Muon Sites and Muon States in Model Fluorides and Magnets



John Wilkinson

Mansfield College

University of Oxford

A thesis submitted for the degree of

Doctor of Philosophy

Hilary 2022

Muon Sites and Muon States in Model Fluorides and Magnets

John Wilkinson

Mansfield College
University of Oxford

A thesis submitted for the degree of Doctor of Philosophy

Hilary 2022

Abstract

The F–μ–F state occurs when a spin polarised muon implanted in a fluoride crystal becomes entangled with its nearest neighbour fluorine nuclei, resulting in a beating pattern observed in the muon decay asymmetry. Ever since these states were discovered in the 1980s, they have never been fully understood, as fitting the data always required a phenomenological relaxation function to account for the observed decay of the oscillations.

This thesis shows how this relaxation can be understood by considering it as a decohering process, achieved by taking into account the effect of all the nuclear spins beyond the nearest-neighbours. Starting with the simple cubic compounds CaF_2 and NaF, techniques are developed which allows one to calculate the way in which the quantum information of the muon gets irreversibly lost into the crystal. This thesis then expands on this to discuss the compounds PbF_2 and YF_3, which have a more complicated crystal structure, and in the former compound it is possible to identify Frenkel defects with μSR for the first time.

This thesis then shows how it is possible to apply these techniques to magnets: starting with KPF_6 and KBF_4, which contain the $[PF_6]^-$ and $[BF_4]^-$ molecular ions which are often found in molecular magnets, it shows how the location of the muon site in the compound considerably changes the observed muon polarisation, determining the muon stopping site by carefully analysing the muon's environment. Finally, the antiferromagnetic material $KAgF_3$ is analysed with these methods, showing how a combination of DFT+μ, dipole field calculations and the techniques developed here can be used to determine the size of the electronic moments, confirm magnetic structures and narrow down the muon site. This final chapter also shows how the nearest-neighbour fluorine nuclear moment can affect the muon polarisation in magnets in a fascinating way.

Acknowledgements

I have been privileged to have worked with many people in completing this thesis, who have helped me hugely throughout my time in Oxford. Firstly, I would like to thank **Steve Blundell**, my brilliant supervisor for being such a great help throughout my project, and for being able to explain everything in such an understandable way. **Francis Pratt** for taking me on as a summer student back in 2017 and introducing me to μSR, and for all of his help during experiments. **Tom Lancaster** for being very helpful and providing me with data to test out my simulations and for useful discussions at conferences. **Franz Lang** for training me up with DFT+μ and providing me with the code to make running the calculations a lot easier. **George Gill** for getting me into *The Office*, wine, and for proofreading my thesis. **Hank Wu** for the weekly memes at the group meetings. At ISIS, I would like to thank the muon group for all their experimental support and beamtime, in particular I would like to thank **Peter Baker**, **Pabi Biswas**, and **Steve Cottrell** for taking some of the data (CaF_2 and KPF_6) for me. **Marina Filip** for all her expertise in DFT which has massively helped me in my calculations. **Dharmalingam Prabhakaran** for his help with the X-ray measurements and for his samples. **Wojciech Grochala** for growing the $KAgF_3$ sample, which led to my favourite chapter in this thesis. **Chennan Wang** at PSI for running our experiments during COVID. **Jonathan Patterson** for all his help in using the Glamdring cluster. My students at **New College** for their deep and thoughtful condensed matter questions, which have made me think twice about all the things I thought I understood. Finally, I would like to thank **EPSRC** for funding my work, and **STFC** for funding ISIS.

I would also like to thank all my friends and housemates I have hung out with while at Oxford for giving me a break from my code, in particular George (whaaaat?), Arkady, Tom, Adam and the Addison Crescent rats (the latter who encouraged me to write faster so I could move out sooner...), Stephen for the antique furniture removal adventures, Lottie for the chaos, Oli, Jon and Elisabeth for the Karaoke nights, Achille for the food and Mads for all the trips to London and listening to my moans and groans.

Finally, I would like to thank my family: Mum, Dad, Charlotte, Katie, Alfie, Holly, Rosie and George[1] for being a constant source of love and support throughout my DPhil and indeed my life. Thank you for everything.

[1]Some of these family members have $n_{\text{legs}} > 2$.

Added post-viva

I would like to additionally thank my D.Phil examiners, **Arzhang Aardvan** and **Jorge Quintanilla**, whose detailed reading and intense questioning of my work here has led to many improvements, and helped me to understand the intricacies of the physics in much greater detail.

Contents

List of Figures **xi**

List of Publications **xix**

1 Introduction **1**

Thesis outline 3

2 Muon Spin Rotation **5**

2.1 Overview of the μSR technique 6

2.1.1 Pulsed muon sources 9

2.1.2 Continuous muon sources 11

2.2 Muon precession 13

2.2.1 A muon in a magnetic field 14

2.2.2 Muon–matter interactions 16

2.2.3 Polycrystalline samples 17

3 The Muon Site Problem, DFT+μ, and Fluorides **19**

3.1 Introduction to the muon site problem 19

3.2 DFT+μ 20

3.2.1 Density functional theory: an overview 20

3.2.2 DFT+μ: using DFT to find muon sites 24

3.3 Fluorides 26

4 Decoherence and the Muon Site Problem: A Study of CaF_2 and NaF **31**

4.1 Introduction 31

4.2 Quantum information in F–μ–F states 34

4.3 CaF_2: a model system 38

4.4 NaF: a model quadrupolar system 44

4.5 Low-energy muons and fluoride states 46

4.6 Conclusion 48

5 Muon Sites in PbF_2 and YF_3: Decohering Environments and Frenkel Defects **49**
5.1 Introduction . . . 49
5.2 Frenkel defects . . . 50
5.2.1 Theory . . . 50
5.2.2 Frenkel defects in fluorides . . . 52
5.3 DFT+$Mu^{\pm}$ . . . 53
5.4 μSR experiments and results . . . 57
5.4.1 PbF_2 results . . . 57
5.4.2 YF_3 results . . . 62
5.4.3 Comparison to previous approaches . . . 64
5.5 Conclusion . . . 64

6 KPF_6 and KBF_4: Identifying Muon Sites "by eye" **67**
6.1 Introduction . . . 67
6.2 Experimental details . . . 69
6.3 KPF_6 . . . 70
6.3.1 Muon site determination . . . 72
6.3.2 Data analysis . . . 76
6.4 KBF_4 . . . 79
6.4.1 Muon site determination . . . 80
6.4.2 Data analysis . . . 86
6.5 Conclusion . . . 88

7 $KAgF_3$: a Magnetic Fluoride **89**
7.1 Introduction . . . 89
7.2 DFT+μ . . . 92
7.3 μSR experiments . . . 93
7.3.1 $T < T_c$: measuring the magnetic order . . . 94
7.3.2 $T > T_c$: measuring the muon-induced perturbations . . . 96
7.4 Analysis . . . 101
7.4.1 Calculating the Ag^{2+} moment . . . 101
7.4.2 F–μ states and magnetic order . . . 102
7.5 Conclusion . . . 106

8 Conclusion **109**
Future work . . . 110

Appendices

A Classical Derivation of Muon Precession in a Magnetic Field 117

B Derivation of the Muon Polarisation of a Linear F–μ–F State 119

C Magnetic Properties of Nuclear Isotopes 125

References 127

List of Figures

2.1 **Muon decay positron emission distribution.** The probability distribution of the direction of the emitted positron (black) with respect to the direction of the decayed muon's spin (red arrow). . . 8

2.2 **Typical μSR instrument schematic.** The muon enters in through the left-hand side of the diagram, implants itself in the material, and the emitted positron is detected in either the backwards set of detectors (B) or the forwards (F). 9

2.3 **CAD drawing of the MuSR detector at ISIS.** The sample sits in a cryostat in the yellow region. Note the large number of positron detectors (the photomultiplier tubes in red) to reduce the dead time effects. Taken from Ref. [39]. 10

2.4 **Plan of the detector arrangement of the GPS instrument at PSI.** The Up detector is not shown, but is above the sample (out of the page). Taken from Ref. [40]. 12

3.1 **The Hohenberg–Kohn theorem.** Starting from the top-left, if one defines the external potential of the electrons due to the nuclei, V_{n}, one can use the Schrödinger equation (S.E.) to calculate the electronic eigenstates $\Psi_i(\{\boldsymbol{r}\})$, and hence their ground states $\Psi_0(\{\boldsymbol{r}\})$. One can then use Born's result of the particle density being the modulus of the wavefunction squared [48], to obtain the ground state electronic density $n_0(\boldsymbol{r})$. The Hohenberg–Kohn theorem (in red) states that it is possible, with *just* the ground state electron density, to obtain V_{n}. Figure adapted from Ref. [47]. 20

3.2 **Muon sites in $\mathbf{UTe_2}$. a** shows the contours of the total potential, calculated with DFT (note that energies lower than 0.4 Ry are not shaded for visual clarity). **b** shows this same potential, across a plane perpendicular to the c axis, with $c = \frac{1}{2}$. Both subfigures have the energies shaded according to the legend in the centre of the figure. . 26

3.3 **Results of J. H. Brewer et al.'s NaF μSR experiment**, showing the fits produced by the F–μ–F function (Equation (3.9), grey line), and that produced by the F–μ–F function multiplied by a stretched exponential function with $\beta = 1.5$ (red line). Data and fit reproduced from Ref. [67]. 28

4.1 **Energy levels in F–μ–F states.** **a** The energy levels in an F–μ coupled state. The eigenstates are labelled by the spins of the muon and the fluorine nucleus. The red arrows link levels between which quantum-mechanical interference can occur and the energies are in units of $\hbar\omega_{\mathrm{D}} = \hbar^2\mu_0\gamma_\mu\gamma_F/(4\pi r^3)$. **b** The energy levels for an F–μ–F state, also showing possible interferences (thicker lines connect energy levels between which there is the largest amplitude of quantum interference). The energy eigenvalues are very slightly different from those shown once the small F–F dipolar coupling is included, as will be done in all subsequent plots. **c** The time-dependence of the muon polarisation $P^\mu(t)$ for isolated F–μ (dotted line), isolated F–μ–F (dashed line) and for F–μ–F also coupled to eight next-nearest-neighbour fluorine nuclear spins appropriate for the fluorite structure (blue line). These simulations are for an experiment in zero applied magnetic field, and assume a polycrystalline average over all possible orientations of the F–μ or F–μ–F species. **d** Energy levels for the F–μ–F state including next-nearest-neighbour fluorine nuclear spins. **e** Interference amplitude for isolated F–μ–F (top panel) and with the next-nearest-neighbour couplings (bottom panel). The amplitude of the quantum interference between energy levels $\hbar\omega_1$ and $\hbar\omega_2$ is represented by the relative areas of the points in the top panel and by a grey scale in the bottom panel. The energy scales of **b** and **d** are lined up with these two panels. 33

4.2 **von Neumann entropy for muon–fluorine states.** The top panel shows the case when the initial muon polarisation is aligned along z (defined as the vector linking the muon with its nearest-neighbour fluorine). The bottom panel shows the case of the initial muon polarisation perpendicular to this vector (x). 35

4.3 **Mutual information in the F–μ system.** **a**, The mutual information in the F–μ, F–μ–F and F–μ–F state with the next-nearest neighbour (nnn) couplings included, where the initial muon polarisation is perpendicular to the F–μ bond. Here, S_μ is the entropy of the muon, and S_F is the entropy of all the N fluorine nuclei included in the calculation. **b**, the same as **a** but with the initial muon polarisation parallel to the F–μ bond. 37

4.4 **Crystal structure of CaF_2 and NaF.** **a** depicts the positions of the calcium (magenta) and fluorine (red) atoms in CaF_2, and **b** depicts the positions of the sodium (blue) and fluorine atoms in NaF. 38

4.5 **The effect of ζ_{nnn} on F–μ–F frequencies.** The Fourier transform of the F–μ–F + nnn muon polarisation is shown for various ζ_{nnn}, demonstrating the effect of adjusting ζ_{nnn} on the muon precession frequencies. The bottom plot shows the positions of the major peaks as a guide to the eye. 41

4.6 **Muon data and fits for CaF_2 and NaF. a** Muon decay asymmetry data $A(t)$ for polycrystalline CaF_2 (at 50 K), together with the simulated muon polarisation without (dotted line) and with (solid line) the effects of environmental decoherence. **b** The muon (green sphere) strongly coupled to two fluorine nuclei (dark blue spheres), and weakly coupled to next-nearest neighbour fluorine nuclei (cyan spheres), embedded inside the fluorite structure of CaF_2. **c** $A(t)$ for NaF (at 100 K), with simulations as in **a**. **d** The muon (green sphere) strongly coupled with the two nearest-neighbour fluorine nuclei (blue spheres, pulled close to the muon) and weakly coupled with the two nearest sodium nuclei (orange spheres, pushed away from the muon), and the next-nearest-neighbour fluorine nuclei (cyan spheres). . . . 43

4.7 **Effect of the quadrupolar interaction on NaF.** The red line shows the evolution of the muon polarisation only considering dipole couplings, and the blue line also includes the small quadrupolar coupling on the Na ions. 45

4.8 **Exploring the surface of CaF_2 with low energy muons. a** shows the stopping profile of the muons with energy 8 keV on a 150 nm N_2 layer. **b** shows the muon polarisation from muons stopped at the very surface, compared with those stopped in the bulk sample . 47

5.1 **Muon sites in PbF_2 and YF_3**, calculated with DFT. The left-hand side shows the muon site calculated with the DFT+μ method, as described in the text. In all cases, the muon (black sphere) sits in between two fluoride ions (red spheres), and the transparent (solid) spheres show the locations of the surrounding ions before (after) the perturbation of the implanted muon. The centre column shows the position of the defect fluorine in the perfect lattice, and the final (initial) relaxed positions of the surrounding ions are displayed as solid (transparent) spheres. Finally, the right-hand column shows the site of the Mu^- (black sphere) in the vacancy created by such a defect, and the effect of this on the surrounding ions. 54

5.2 **Polarisation of the three muon sites in α-PbF_2**, predicted by DFT+μ to have the lowest total energy. The inset shows the muon sites with the three lowest energies as red, blue and green spheres (ignoring muon-induced distortions), and the time dependence of muon polarisation expected from these three sites is shown in the main frame. 55

5.3 **Polarisation of the YF_3 muon sites**, predicted by DFT+μ to have the lowest total energy. The inset shows the muon sites with the lowest energy (green), 35 meV above this (red), and 72 meV above the lowest energy site (blue) (the distortions induced by the muon are not shown). The graph in the main frame corresponds to the expected muon polarisation from these three sites. 56

5.4 **α-PbF_2 results. a** shows the zero-field μSR data obtained for our sample of PbF_2, and the solid (dashed) lines corresponding to fits of the data with (without) taking into account the Mu^- entering into a defect state. **b** shows the data obtained with a longitudinal field applied, plotted with the muon polarisation as described in the text. 58

5.5 **PbF_2 Mu^- state fits.** The main plot shows the fit of the muon asymmetry from the model including a Mu^- state in crystals both with an AFD and without an AFD (the "perfect lattice"), and without including any Mu^- states at all. Inset: the muon polarisation exclusively from the two Mu^- states, i.e. without the μ^+ component. 60

5.6 **YF_3 results.** The results of our μSR experiment, with the fitted muon polarisation using the muon site obtained by DFT. This site is displayed on the YF_3 crystal structure in the inset, with the atom positions unperturbed for simplicity. 62

5.7 **Comparison of fitting techniques for PbF_2 and YF_3**. The graphs show fits to the data for PbF_2 (top graph) and YF_3 (bottom) with an F–μ–F function multiplied by a stretched exponential (grey), and the fits considering all the nuclei in the crystal (red). 65

6.1 **KBF_4 and KPF_6 muon data. a** shows the data obtained at 10 K for KBF_4 with the MUSR spectrometer, and **b** shows the data for KPF_6 taken at 10 K with the EMU spectrometer. **c** shows the data for the latter sample taken with the MUSR spectrometer, with the slits set to 100 mm, but one can see that the deadtime (DT) correction is significant, and even with this correction there is a clear slowly relaxing background which is not present in the EMU data. . 71

6.2 **Crystal structure of the low-temperature 'wet' phase (IV) of KPF_6.** The $[PF_6]^-$ octahedra consist of eight fluorines (grey) which occupy the same Wyckoff position, with a P in the centre (dark pink). These ions are intercalated with K^+ (purple). 72

6.3 **Muon states in KPF_6.** The expected muon polarisation was calculated for the muons in the positions as shown on the diagram in the left side of the figure, with the colour of the muons matching the corresponding muon polarisation on the right hand side. The octahedra shown are the two shown in the conventional unit cell depicted in Figure 6.2, looking in the $-\boldsymbol{b}$ direction. 74

6.4 **Fits of the KPF_6 EMU data**, using Equation (6.1). The fits are in a very good agreement with the data for all the measured temperatures. 78

6.5 **Crystal structure of KBF_4.** The $[BF_4]^-$ tetrahedra consist of two fluorides in the F3 site, and one in F1 and F2. 79

6.6 **Muon states in KBF_4.** The muon polarisation expected from muons in all four potential muon states calculated with DFT+μ are plotted. Inset: The muon asymmetry data from the KBF_4 sample. . 83

6.7 **Muon-induced perturbations in KBF_4**. The muon is represented by the black sphere, fluorine by the red and boron by the green sphere. Distorted (undistorted) positions are shown as solid (translucent) spheres, and the lines connecting the spheres are guides to the eye. The potassium ions are not shown for clarity. 84

6.8 **KBF_4 μSR fits**. The main plot shows the fit of the muon data to Equation (6.7). The inset shows the muon polarisations obtained when the borons in the positions of B_1 and B_2 are either ^{10}B or ^{11}B. 87

7.1 **Crystal structure of $KAgF_3$**. The Ag^{2+} ions are connected in Ag–F–Ag chains in the **b** direction by fluorines of the type F1, and the **a**-**c** planes contain two dimensional AgF_2 sheets, using the fluorine of the type F2. 90

7.2 **Potential $KAgF_3$ muon sites.** The two candidate muon sites as described in Table 7.1 are shown. Neither the muon-induced structural perturbations nor the potassium ions are shown for visual clarity. 93

7.3 **PSI $KAgF_3$ data and fits. a** shows the PSI data with the sample holder background removed, where the oscillations can be clearly observed. The black lines represent the fit to Equation (7.2), as described in the text. **b** shows how the amplitudes of the two oscillating components A_1 and A_2 vary with temperature, **c** shows the frequency of these oscillations (the cyan line shows the fit to the model as described in the text), and **d** the relaxation of these two components. 94

7.4 **$KAgF_3$ μSR data taken with MuSR.** The oscillations observed above 30 K are due to the muon entering into an F–μ–F state, due to the entanglement between the muon and the nearest fluorine nuclei. The inset shows the data in the main graph at short times, where one can see the onset of magnetic order in the sample (which is resolved better in the PSI data plotted in Figure 7.3**a**). 97

7.5 **$KAgF_3$ fits for both DFT sites.** Both sites discussed in Table 7.1 were fitted to the ISIS data at 60 K using Equation (7.4). 99

7.6 **ISIS $KAgF_3$ data and fits. a** shows the fits to the data using the model described in the text. **b** shows the variation of the relaxing asymmetry A_r and background asymmetry A_bg with temperature T, and **c** shows how the μ–F distances r_nn1 and r_nn2 vary. 100

7.7 **Coordinate system used for the calculation of F–μ states in a magnetic field**. The coordinates are aligned such that the field on the muon is in along z, and such that the component of the fluorine's field along y is zero. 102

7.8 **F–μ states in a magnetic field. a** shows how the amplitudes of the components of the muon precession signal vary as the field on the muon and fluorine sites are scaled by a factor of $B/B^0_{\mu,\mathrm{F}}$ (the key shows the precession frequencies as $B\to\infty$). The inset shows how the amplitudes A_1 and A_2 of the two measured components vary with the muon precession frequency, showing how at low fields A_1 and A_2 become closer in value, in support of this model. **b** shows the Fourier transform of the system of the muon coupled to its nearest- and next-nearest neighbour spins, for the field at the muon and fluorine sites scaled by various amounts, as shown in the legend. 105

8.1 **Muon–iodine entanglement in KI.** The muon polarisation for KI is plotted for a muon interacting with its nearest-neighbour iodine nuclei (pink line) and three of its next-nearest-neighbours (red line) (calculating this for all four nnn nuclei results in matrices of size 93312×93312, which is very computationally challenging). The grey lines show the fits to these lines with a Gaussian and Kubo–Toyabe oscillation, showing the effect the muon–iodine entanglement has on the polarisation. 111

8.2 **PERFECTA μSR data.** The data obtained at 4 K with the MuSR spectrometer at ISIS is shown, alongside the chemical structure in the inset (note that the hydrogen atoms are not shown for clarity) . 113

A.1 **Coordinate system used for the derivation of muon precession in a magnetic field.** 117

List of Publications

- J. M. Wilkinson and S. J. Blundell, *Information and decoherence in a muon-fluorine coupled system*, Physical Review Letters **125**, 087201 (2020).
- J. M. Wilkinson, F. L. Pratt, T. Lancaster, P. J. Baker, and S. J. Blundell, *Muon sites in PbF_2 and YF_3: decohering environments and the role of anion frenkel defects*, Physical Review B **104**, L220409 (2021).
- G. J. W. Gill, J. M. Wilkinson, F. Lang, J. N. Blandy, S. J. Clarke, and S. J. Blundell, *Muon-spin rotation study of the layered oxyselenide $Sr_2CoO_2Ag_2Se_2$*, submitted to Physical Review B.
- P. Bonfà, J. Frassineti, J. M. Wilkinson, G. Prando, M. M. Isah, C. Wang, T. Spina, B. Joseph, V. F. Mitrović, R. De Renzi, S. J. Blundell and S. Sanna, *Entanglement between muon and $I > \frac{1}{2}$ nuclear spins as a probe of charge environment*, submitted to Physical Review Letters.

1 Introduction

Magnetism is a phenomenon which has been known to mankind for millennia: lodestone, a magnetised piece of the mineral magnetite (composed of various iron oxides), was one of the first known magnetic materials, and was mentioned in texts from the ancient Chinese and Greek civilisations (the oldest known writings about lodestone is from the Chinese writer Guanzhong, who died in 645 BC) [1]. Writings by Gui Guzi and Han Fei from ancient China in around 280 BC indicate that it was well known that lodestones tend to point towards the Earth's poles, and the idea of magnetic attraction was written about by both Gui Guzi (400 BC) and Hippocrates (460 BC – 377 BC) [1].

Since then, humanity has made a lot of progress in our understanding of magnetism. The work of Michael Faraday [2], Pierre-Simon de Laplace and André-Marie Ampère on electromagnetism, culminating in the discovery of Maxwell's equations [3], shows how electric and magnetic fields are intrinsically linked, and is consistent with Albert Einstein's theory of special relativity [4] (in fact, magnetism is intrinsically a relativistic effect, originating from the movement of charges in the observer's rest frame). The discovery of spin as an intrinsic property of electrons by Wolfgang Pauli in 1925 [5], and later Werner Heisenberg's investigations in 1928 of the interactions between spins in a compound leading to magnetic ordering

resulted in the Heisenberg model which provides an excellent description of many magnetic materials [6].

Despite these successes, a full understanding of *why* some materials magnetically order and others don't is still lacking. Understanding the way in which around 10^{23} atoms interact with each other is very difficult[1] and humanity is not yet at the stage where we know exactly how a given material behaves magnetically before measuring it. This is a big problem, as magnets are incredibly useful: for example in navigation, data storage, electricity generation and in many other applications.

Therefore, the understanding and discovery of magnetic materials is primarily done empirically. There are many well-known techniques for this, including measuring the magnetic susceptibility [7], neutron scattering [8], and nuclear magnetic resonance (NMR) [9], but in this thesis I will focus on muon spin rotation, often abbreviated to μSR[2]. This technique involves implanting spin-polarised muons into materials, and using them to measure the magnetic fields at the microscopic scale. Performing μSR experiments is now a relatively straightforward process as many of the instruments are heavily automated, but like many experimental techniques, understanding the data from these experiments is often very challenging and in many cases requires computational simulations of the way in which the muon interacts with the atoms around it, and sometimes only a qualitative understanding of the data is possible.

Instead of focusing on the complicated materials with lots of constituents interacting with each other in highly nontrivial ways, it can be often be a lot more helpful to measure model systems, chosen so that they exhibit the properties one wishes to measure, but lack those which only serve to complicate the data. In this thesis I will focus on fluorides, where a full analysis method for their μSR data was lacking for many years. I will show how, by focusing on compounds with a very simple structure and with no electronic moments, analysis methods can be

[1] You can see this problem immediately by considering that if each spin has two states, even dealing with twenty would result in over one million configurations (2^{20})!

[2] The 'R' in μSR can also stand for 'relaxation' and 'resonance', but this thesis will not discuss these.

devised and then applied to more complicated materials, including some exciting state-of-the-art materials *with* ordered electronic moments.

Thesis outline

This thesis is laid out as follows:

Chapter 2 gives an introduction to the technique of μSR, introducing the experimental setup and practicalities, and also introduces some simple muon polarisation functions.

Chapter 3 introduces the muon site problem, giving a brief overview of the technique of DFT+μ. It also talks about F–μ–F states, and shows how these have been used in the past to locate muon stopping sites.

Chapter 4 re-frames the F–μ–F problem with a quantum information framework, investigating the decoherence of the muon's quantum information and using this to explain the relaxation observed in these states using the simple cubic compounds CaF_2 and NaF.

Chapter 5 investigates the F–μ–F decoherence of two compounds with more complicated crystal structures than the previous chapter. By investigating the decohering environments in these crystals, I show that it is possible to identify Frenkel defects using μSR for the first time.

Chapter 6 uses the methods developed in the previous two chapters and applies them to the compounds containing the ions $[BF_4]^-$ and $[PF_6]^-$, which are often found in molecular magnets. I show how these methods can be used to determine the muon site in these compounds with high accuracy.

Chapter 7 looks at the recently synthesised fluoroargentate $KAgF_3$, which contains Ag^{2+} moments which magnetically order. This chapter shows that investigating the muon–fluorine coupling can give an excellent indication as to the nature of the magnetic ordering, and argues that even below the ordering transition temperature the nuclear moment of the fluorine still affects the μSR spectrum in a fascinating way.

Chapter 8 contains concluding remarks for this thesis, suggesting future work which could be undertaken to expand on it.

Additionally, this thesis contains three appendices:

Appendix A goes through the derivation of a muon precessing its local magnetic field using classical physics (a very important result for μSR).

Appendix B derives the time evolution of the muon polarisation for an F–μ–F state, showing the origin of the beating pattern observed experimentally.

Appendix C contains the data for the nuclear isotopes of the elements used in this thesis, including gyromagnetic ratios and quadrupolar coupling constants.

2
Muon Spin Rotation

Contents

2.1 Overview of the μSR technique 6
2.1.1 Pulsed muon sources 9
2.1.2 Continuous muon sources 11
2.2 Muon precession 13
2.2.1 A muon in a magnetic field 14
2.2.2 Muon–matter interactions 16
2.2.3 Polycrystalline samples 17

Muon Spin Rotation (μSR) is a technique primarily used to study magnetism in condensed matter systems. Analogous to the techniques of NMR [9] and ESR [10], it relies upon the Larmor precession of the muon due to the particle having a spin of $\frac{1}{2}$, with the key difference being that resonance is *not* necessary – the precession of the muon is instead inferred from the spatial distribution of its decay products [11]. μSR has been used to investigate magnetism in superconductors [12–15], probe magnetic ordering in correlated electron systems [16–20], to examine hydrogen storage materials [21–23], and in many other applications [24]. This chapter introduces the technique, discussing experimental considerations and will derive some key results which will be relied upon in the rest of this thesis. More detailed introductions can be found in various reviews [24–27], and books [28, 29].

	μ^+	e^-	p
Charge	$+\|e\|$	$-\|e\|$	$+\|e\|$
Spin	$\frac{1}{2}$	$\frac{1}{2}$	$\frac{1}{2}$
Magnetic Dipole Moment	$8.890\mu_{\mathrm{N}}$	$-1838\mu_{\mathrm{N}}$	$2.793\mu_{\mathrm{N}}$
Gyromagnetic Ratio (Mrad s^{-1})	851.4	1.761×10^5	267.5
Mass	$0.11m_p$	$0.0054m_p$	m_p

Table 2.1: Physical properties of the muon compared to the free electron and proton. Data are from Ref. [33].

2.1 Overview of the μSR technique

Muons are classed as leptons, with a mean lifetime of 2.2 μs, and a mass of approximately 200 times greater than that of an electron [30]. The muons which are most useful for μSR are antimuons, μ^+, which interact with matter in a similar way to protons, as both types of particle have the same charge of $+|e|$. Some μSR work has also been done on negatively-charged muons [31], which tend to behave more like electrons, often joining an electronic orbital and losing some polarisation in the process[1]. In this thesis, I use "muon" to primarily refer to positively charged antimuons. Some of the key properties of muons are tabulated in Table 2.1, alongside the properties of electrons (e^-) and protons (p) for comparison.

Naturally occurring muons can be found on the surface of the earth due to cosmic rays interacting with the atmosphere [34]. However these are unsuitable for μSR experiments since they lack spin polarisation, and are not produced with the intensity required. μSR experiments instead use muons produced at large-scale particle accelerators[2], where protons are accelerated up to around 80% of the speed of light, and collided with a target (often a block of graphite). When these protons collide with either the protons (p) or neutrons (n) in this target, pions (π^+) are produced due to either the reaction

$$p + p \rightarrow n + p + \pi^+,$$

[1]The property of μ^- joining an electronic orbital has been exploited for elemental analysis, as this process results in X-rays being emitted with a frequency which is dependent on the electronic properties of the atom the muon interacts with [32].

[2]The five μSR facilities worldwide are currently ISIS (UK), PSI (Switzerland), J-PARC and MuSIC (Japan) and TRIUMF (Canada).

if a proton from the beam collides with a proton in the target, or

$$p + n \rightarrow n + n + \pi^+,$$

if a proton from the beam collides with a neutron. These pions subsequently decay into antimuons (μ^+) through the weak interaction,

$$\pi^+ \rightarrow \mu^+ + \nu_\mu.$$

Since the muon neutrino (ν_μ) is a highly relativistic particle, its helicity is aligned with its linear momentum. For pions at rest in the lab frame, both the muon and neutrino must be emitted in exactly opposite directions. Due to the violation of parity exhibited in the weak interaction, only neutrinos with negative helicity exist (i.e. its spin is always aligned antiparallel with its linear momentum), and in order to conserve angular momentum in the decay of π^+, the muon must *also* have negative helicity, as pions are spinless. Therefore, selecting muons with a momentum of 29.97 MeV c^{-1}, corresponding to muons produced by pions at rest in the lab frame, one can ensure that the beam of muons produced is 100% spin-polarised[3] [11, 28, 29].

The beam of spin-polarised muons, after passing through various quadrupole and dipole magnets to focus the beam and to ensure a homogeneous muon momentum, is finally incident upon the sample to be measured. When the muons enter the sample, they lose energy primarily through electron scattering and ionisation reactions [25, 37], which result in the muon eventually stopping somewhere within the sample, at a depth of around a few millimetres [27]. Implanted muons can form a number of different charge states: a diamagnetic "bare" muon (μ^+), a paramagnetic neutral muonium state (Mu=μ^+e^-), or a diamagnetic negatively charged muonium state (Mu$^-$=μ^+2e^-)[4]. The muon then interacts with its environment, causing the

[3]This is for so-called "surface" muons (which result from pion decays at the surface of the target [35]). The RIKEN-RAL facility at ISIS also uses "decay" muons, where the pions decay in-flight. This results in a beam which is not as spin-polarised as surface muons, but allow the experimenter to select the muon momentum (useful for pressure cell experiments) and can produce negative muons [36].

[4]The use of the terms "paramagnetic" and "diamagnetic" here refers to the electronic nature of the state: for the state where there is an unpaired electron (Mu), the paramagnetic term $\mathcal{H} \propto \mathbf{I} \cdot \mathbf{S}$ dominates the Hamiltonian.

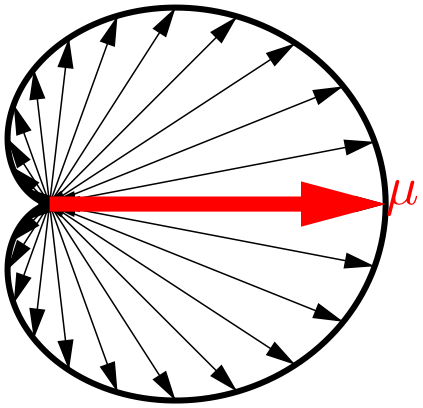


Figure 2.1: Muon decay positron emission distribution. The probability distribution of the direction of the emitted positron (black) with respect to the direction of the decayed muon's spin (red arrow).

polarisation of the muon to vary as a function of time (see next section), before decaying into a positron, again through the weak interaction,

$$\mu^+ \rightarrow e^+ + \nu_e + \bar{\nu}_\mu,$$

which is a three-body decay process. The probability of a positron with energy (as a fraction of the maximum kinetically possible) x, being emitted at an angle θ to the direction of the muon spin, $W(x,\theta)$, is given by

$$W(x,\theta) = \frac{2x^2(3-2x)}{4\pi}\left(1 + \frac{2x-1}{3-2x}\cos\theta\right), \tag{2.1}$$

so the direction of the emitted positron is most likely to be in the direction of the muon spin at the time of its decay[5]. This is plotted for a positron emitted with maximum energy ($x = 1$) in Figure 2.1. This means, by measuring the spatial distribution of emitted positrons, with enough statistics one can infer the most likely direction of the muon's spin before it decayed as a function of time.

A μSR instrument typically consists of two sets of positron detectors, labelled Forwards and Backwards, as shown in Figure 2.2. The number of muons detected by the forwards and backwards detectors, $N_{\mathrm{F}}(t)$ and $N_{\mathrm{B}}(t)$ respectively, varies as

$$N_{\mathrm{B}}(t) + N_{\mathrm{F}}(t) = N_0 e^{-\frac{t}{\tau_\mu}}, \tag{2.2}$$

[5]This distribution is derived using the so-called Michel Parameters [38], but this is beyond the scope of this thesis.

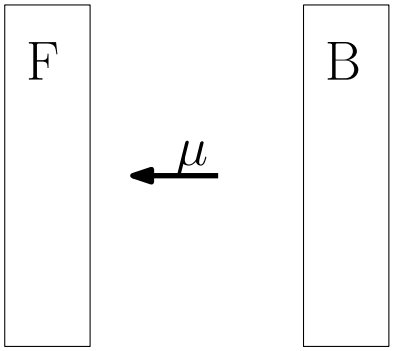


Figure 2.2: Typical μSR instrument schematic. The muon enters in through the left-hand side of the diagram, implants itself in the material, and the emitted positron is detected in either the backwards set of detectors (B) or the forwards (F).

with $\tau_\mu = 2.2$ µs [30]. The time evolution of the muon's polarisation is proportional to the asymmetry, $A(t)$, calculated as

$$A(t) = \frac{N_{\mathrm{F}}(t) - \alpha N_{\mathrm{B}}(t)}{N_{\mathrm{F}}(t) + \alpha N_{\mathrm{B}}(t)}, \tag{2.3}$$

where α is a parameter which quantifies to the difference in detector geometry and efficiency, which is experimentally determined by applying a small transverse field (usually around 20–30 Gauss), and finding the value of α which makes the resulting muon asymmetry sinusoidal.

There are three magnetic field configurations which are used for μSR experiments: Zero-Field (ZF-μSR), where active magnetic field cancellation is used, Longitudinal-Field (LF-μSR), where a magnetic field is applied in the same direction as the muon's initial polarisation, and Transverse-Field (TF-μSR), where a magnetic field is applied in a perpendicular direction to the muon's initial polarisation [28]. In this thesis, I will primarily use ZF-μSR unless explicitly stated.

Muon facilities are generally split into two categories: pulsed muon sources, such as ISIS and J-PARC, and continuous sources, such as PSI and TRIUMF.

2.1.1 Pulsed muon sources

In pulsed sources, a pulse of several hundred muons are implanted into the sample at the same time, and the separation between pulses is set to be much larger than the decay time of the muons. These sources have the advantage that data can be

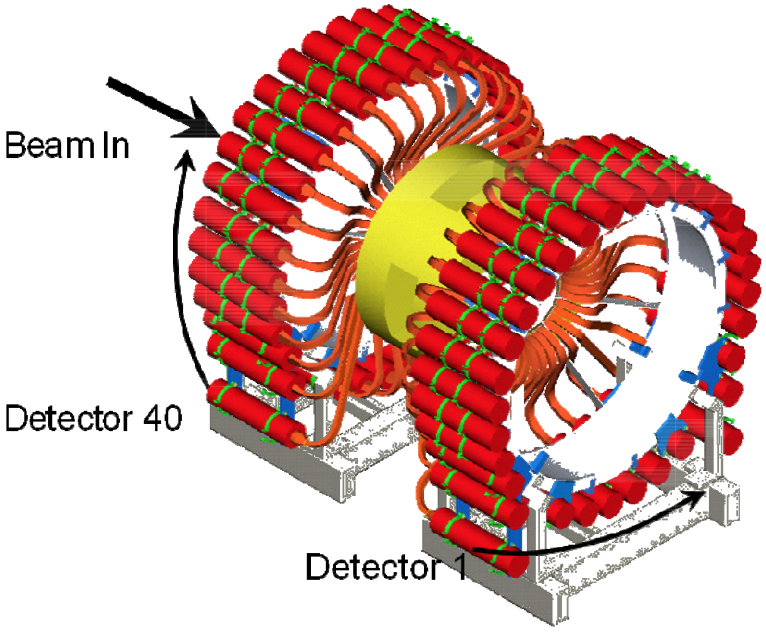


Figure 2.3: CAD drawing of the MuSR detector at ISIS. The sample sits in a cryostat in the yellow region. Note the large number of positron detectors (the photomultiplier tubes in red) to reduce the dead time effects. Taken from Ref. [39].

measured out to several microseconds, despite the number of muons present in the sample decreasing by a factor of e^{-1} every 2.2 μs, as it is possible to get a large amount of decay statistics. The key disadvantage of pulsed muon sources is that the finite width of the pulse of muons means there is an inherent uncertainty in the time taken by each muon to decay (as the muon in question could have arrived at the start *or* the end of the pulse, or somewhere in between), and therefore it is not possible to measure fast muon precession in strong magnetic fields (the pulse width for the MuSR instrument at ISIS is 80 ns, hence limiting the maximum measurable precession frequency to around 6 MHz [39], and even frequencies below this will have a reduced amplitude compared to a continuous source due to the phase difference caused by the pulse width).

A cartoon of a typical instrument at a pulsed muon source (MuSR at ISIS) is shown in Figure 2.3. Before the beam enters the instrument, it is incident on an aperture (often referred to as the "slits"), which serves two purposes: firstly, it restricts the cross section of the beam to reduce the number of muons that miss the sample, and secondly it allows one to restrict the number of muons measured per

beam pulse (often referred to as a "frame"), to minimise dead time effects (defined below). For the first point, optimum slit widths can be chosen by calculating the figure of merit $A_{\mathrm{rel}}^2 R$, where A_{rel} is the relaxing asymmetry (the asymmetry due to muons stopping in the sample), and R is the count rate[6].

Experiments undertaken at pulsed facilities often require data to be acquired over several muon decay lifetimes. However, as this requires a large amount of muon decay statistics, often one wishes to open the slits very wide to get a large number of muons incident on the sample per pulse. However, every time the detectors measure a positron, there is a finite time afterwards before they can measure another one. This time period is called *dead time*, the extent of which is a property of the detectors. The dead time on the MuSR instrument at ISIS tends to be of the order of 10 ns, which is primarily due to the pulse width of the discriminators, which convert the noisy signal from the positron detectors into a clean digital pulse.

One way of correcting dead time is by assuming a non-paralysable model[7], and using a first-order correction of the form

$$N_{\mathrm{F,B}}^{*} = \frac{N_{\mathrm{F,B}}^{\mathrm{M}}}{1 - (\tau_{\mathrm{DT}}/\tau_{\mathrm{bin}}) N_{\mathrm{F,B}}^{\mathrm{M}}}, \tag{2.4}$$

where $N_{\mathrm{F,B}}^{\mathrm{M}}$ is the measured number of counts in either the forward (F) or backward (B) detectors, $N_{\mathrm{F,B}}^{*}$ is the corrected number of counts, τ_{DT} is the dead time, and τ_{bin} is the bin width. Such a correction works well if the dead time is not significant, but it can fail at larger count rates. In order to counteract the dead time, muon instruments are made with a large number of detectors (MuSR has 64, which will be increased to around 600 after the Super-MuSR upgrade).

2.1.2 Continuous muon sources

Continuous sources, in contrast to pulsed, only implant one muon at a time. The instrument waits for the implanted muon to decay (or until the timeout, which

[6] This comes from the fact that increasing the rate decreases the error bars by a factor of $\sqrt{N}$ (where N is the number of counts), so the increase of the muon rate decreases the error bars by $\sqrt{R}$.

[7] A non-paralysable model assumes that any positrons incident on the detector during the dead time are ignored; while a paralysable model assumes that the dead time resets if a positron is incident on the detector in this time.

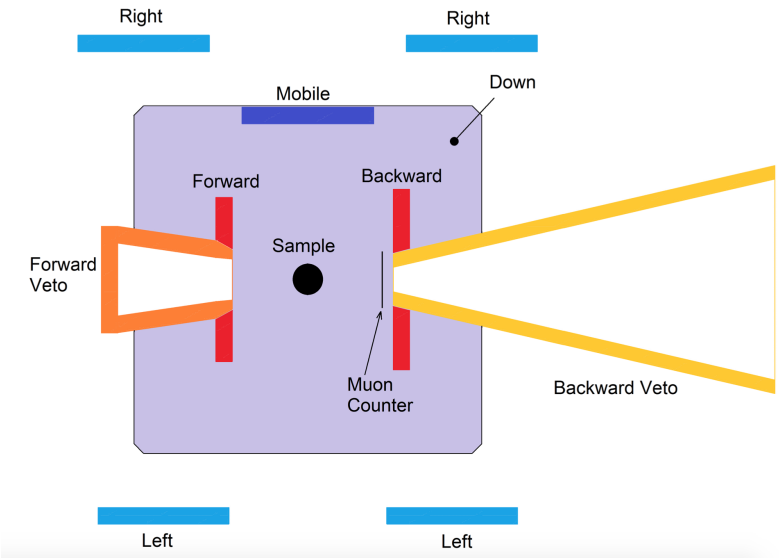


Figure 2.4: Plan of the detector arrangement of the GPS instrument at PSI. The Up detector is not shown, but is above the sample (out of the page). Taken from Ref. [40].

can be set by the user) before proceeding to admit another, which means that the largest measurable muon precession frequency is determined only by the time resolution of the detectors. This tends to be around 400 ps, corresponding to a maximum muon precession frequency of around 600 MHz, which makes these sources particularly useful for experiments to measure the detailed magnetic ordering of samples (for example $KAgF_3$ in Chapter 7).

The detector schematic for a typical μSR spectrometer at a continuous muon facility is depicted in Figure 2.4, which is the GPS instrument at PSI [40]. As only one muon is incident on the sample at a time, dead time is not an issue for the instruments, and therefore it is not necessary to have a large number of positron detectors. Instead, there are the six detectors for measuring the muon decays (labelled Up, Down, Forward, Backward, Left and Right), a Backward Veto detector to collimate the muon beam and to reject muons which are likely to miss the sample, and a Forward Veto to reject muons which miss the sample completely.

Normally, to maximise the number of detectors being utilised, the spin of the muon is rotated by 45° before reaching the sample with a spin rotator. A spin rotator works by applying a magnetic field in a perpendicular direction to the

muon beam momentum, to make the muon's spin precess for a known amount of time (as the beam momentum is well known). As solely applying a magnetic field would also cause the beam to bend due to the Lorentz force, an electric field is also applied in a perpendicular direction to both the beam momentum and the magnetic field of magnitude vB. In this spin-rotated mode, the muon asymmetry is calculated between the Up+Backward and Down+Forward detectors to find the muon polarisation.

Continuous sources have the main disadvantage that measuring the muon asymmetry out to long muon decay times requires significantly more wall time, as only implanting one muon at a time severely inhibits the statistics one can obtain compared to a pulsed source. Another disadvantage of continuous sources is that the data often has a large background, which is due to some muons surviving beyond the timeout and still being present in the sample when the new muon is admitted. Accordingly, some background correction needs to be applied to the individual detectors before the data can be analysed.

2.2 Muon precession

This section will set up the mathematical basis of muon precession, deriving some important results which will be heavily utilised in the remainder of this thesis. To calculate muon polarisation functions, it is simplest to use a density matrix, ρ, to describe the system. This is defined as

$$\rho = \sum_i p_i \left|i\right\rangle \left\langle i\right| \tag{2.5}$$

for a system in state $|i\rangle$ with probability p_i, and the sum is over all possible states the system can be in.

When a muon in a pure state with spin $S_\mu = \frac{1}{2}$ and initial polarisation $\boldsymbol{P}_\mu$ is implanted in a sample, the density matrix of the muon, ρ_μ, is initially [41]

$$\rho_\mu(t=0) = \frac{1}{2}(\mathbb{1} + \boldsymbol{\sigma}_\mu \cdot \boldsymbol{P}_\mu), \tag{2.6}$$

where $\boldsymbol{\sigma}_\mu = (\sigma_\mu^x, \sigma_\mu^y, \sigma_\mu^z)$ is a vector of the Pauli spin matrices for the muon. The time evolution of this is

$$\rho_\mu(t) = e^{-i\mathcal{H}t}\rho_\mu(0)e^{i\mathcal{H}t}, \tag{2.7}$$

for a time-independent Hamiltonian $\mathcal{H}$. The aim of a muon spin rotation experiment is to measure the muon polarisation as a function of time[8], which can be calculated as

$$P_\mu^\sigma(t) = \mathrm{Tr}[\rho_\mu(t)\sigma_\mu^\sigma(0)] \tag{2.8}$$

in the Schrödinger picture, where the superscript σ denotes the direction of the muon's initial polarisation[9], conventionally chosen to be along z. To demonstrate how this is used, the following section details the calculation of the muon polarisation for a magnetic field applied longitudinally and transverse to the initial muon spin polarisation.

2.2.1 A muon in a magnetic field

For the case where an isolated muon is subjected to a homogeneous longitudinal field, the Hamiltonian is that of the Zeeman interaction [42, 43],

$$\mathcal{H} = -\gamma_\mu S_\mu^z B, \tag{2.9}$$

where $\gamma_\mu = 851.4$ Mrad s^{-1} is the muon's gyromagnetic ratio (as given in Table 2.1). Substituting this into Eq. (2.7), with $\boldsymbol{P}^\mu = \hat{\boldsymbol{z}}$, we get

$$\rho_\mu(t) = \begin{bmatrix} e^{-i\frac{1}{2}\gamma_\mu Bt} & 0 \\ 0 & e^{i\frac{1}{2}\gamma_\mu Bt} \end{bmatrix} \begin{bmatrix} 1 & 0 \\ 0 & 0 \end{bmatrix} \begin{bmatrix} e^{i\frac{1}{2}\gamma_\mu Bt} & 0 \\ 0 & e^{-i\frac{1}{2}\gamma_\mu Bt} \end{bmatrix} = \begin{bmatrix} 1 & 0 \\ 0 & 0 \end{bmatrix}, \tag{2.10}$$

and, using Eq. (2.8), we get $P_\mu^z(t) = 1$, i.e. the muon polarisation is constant. This is no surprise, as the Zeeman Hamiltonian splits the $\pm\frac{1}{2}$ spin states of the muon, but as the muon is initially in an eigenstate of the Hamiltonian, the time evolution of

[8] More specifically, the *expectation value* of the muon polarisation, but for notational simplicity I leave out the angle brackets.

[9] In this thesis, the symbol σ has three different meanings: if it is in normal print (e.g. σ^x), it denotes Pauli spin matrices. If it is used as a superscript, it represents the direction the Pauli matrix corresponds to (and can correspond to any unit vector), and if it is in bold, it corresponds to a vector of Pauli spin matrices ($\boldsymbol{\sigma} = (\sigma^x, \sigma^y, \sigma^z)$).

the phases of the sum of the eigenstates that make up the state of the muon remain constant[10]. Longitudinal fields applied in this way are often used to decouple the muon from its environment, by investigating how large an applied field is required to make the Zeeman interaction the dominant term in the muon's Hamiltonian.

For the somewhat more interesting case of a muon in a transverse magnetic field, the Hamiltonian is now (keeping the muon's initial polarisation along z)

$$\mathcal{H} = -\gamma_\mu S_\mu^x B. \tag{2.11}$$

By substituting this Hamiltonian into Equation (2.7) and diagonalising, using the introducing rotation matrices to rotate the basis of the vector space to be along x, we obtain

$$\rho_\mu(t) = \frac{1}{4}\begin{bmatrix}1 & 1\\ 1 & -1\end{bmatrix}\begin{bmatrix}e^{-i\frac{1}{2}\gamma_\mu Bt} & 0\\ 0 & e^{i\frac{1}{2}\gamma_\mu Bt}\end{bmatrix}\begin{bmatrix}1 & 1\\ 1 & -1\end{bmatrix}\begin{bmatrix}1 & 0\\ 0 & 0\end{bmatrix}\cdot \begin{bmatrix}1 & 1\\ 1 & -1\end{bmatrix}\begin{bmatrix}e^{i\frac{1}{2}\gamma_\mu Bt} & 0\\ 0 & e^{-i\frac{1}{2}\gamma_\mu Bt}\end{bmatrix}\begin{bmatrix}1 & 1\\ 1 & -1\end{bmatrix}, \tag{2.12}$$

so

$$\rho_\mu(t) = \frac{1}{4}\begin{bmatrix}2\cos\frac{1}{2}\gamma_\mu Bt & -2i\sin\frac{1}{2}\gamma_\mu Bt\\ -2i\sin\frac{1}{2}\gamma_\mu Bt & 2\cos\frac{1}{2}\gamma_\mu Bt\end{bmatrix}\begin{bmatrix}1 & 0\\ 0 & 0\end{bmatrix}\cdot \begin{bmatrix}2\cos\frac{1}{2}\gamma_\mu Bt & 2i\sin\frac{1}{2}\gamma_\mu Bt\\ 2i\sin\frac{1}{2}\gamma_\mu Bt & 2\cos\frac{1}{2}\gamma_\mu Bt\end{bmatrix}, \tag{2.13}$$

which results in

$$\rho_\mu(t) = \begin{bmatrix}\cos^2\frac{1}{2}\gamma_\mu Bt & i\cos\frac{1}{2}\gamma_\mu Bt\sin\frac{1}{2}\gamma_\mu Bt\\ -i\sin\frac{1}{2}\gamma_\mu Bt\cos\frac{1}{2}\gamma_\mu Bt & \sin^2\frac{1}{2}\gamma_\mu Bt\end{bmatrix}, \tag{2.14}$$

and then the muon polarisation, again calculated from Eq. (2.8), is

$$P_\mu^z(t) = \mathrm{Tr}\left[\begin{bmatrix}\cos^2\frac{1}{2}\gamma_\mu Bt & i\cos\frac{1}{2}\gamma_\mu Bt\sin\frac{1}{2}\gamma_\mu Bt\\ -i\sin\frac{1}{2}\gamma_\mu Bt\cos\frac{1}{2}\gamma_\mu Bt & \sin^2\frac{1}{2}\gamma_\mu Bt\end{bmatrix}\begin{bmatrix}1 & 0\\ 0 & -1\end{bmatrix}\right] \tag{2.15}$$

$$= \cos\gamma_\mu Bt, \tag{2.16}$$

[10] In other words, if the muon is initially polarised e.g. along x, the initial state of the muon would be the sum of the up and down z states. Time evolving this would result in a factor of $e^{-i\omega_\mu t}$ on one of these states and $e^{i\omega_\mu t}$ on the other, leading to an oscillation in time if one measures the z polarisation.

so the polarisation of the muon oscillates in a coherent fashion. This oscillation is due to the muon initially not being in an eigenstate of the Hamiltonian, but in a sum of both the $\pm x$ eigenstates. The phase between these then varies as a function of time, which leads to an oscillation.

The derivation of muons precessing in a magnetic field can also be done classically, which is given in Appendix A. Note that the classical method only works when none of the eigenstates of the Hamiltonian are entangled, which heavily restricts the utility of such an approach for the measurement of real systems.

2.2.2 Muon–matter interactions

Often, instead of the muon simply precessing in a magnetic field, the muon's polarisation affects that of the spins around it [44]. This effect is most significant when muons interact with nuclei, in which case the density matrix of the entire system (muon and surrounding nuclei) evolves in time, rather than just the muon's. This means the density matrix at time $t = 0$ becomes

$$\rho(0) = \frac{1}{2}(\mathbb{1} + \boldsymbol{\sigma} \cdot \boldsymbol{P}^{\mu}) \otimes \left[\bigotimes_i \frac{1}{2I_i + 1} \mathbb{1}_{2I_i+1} \right], \tag{2.17}$$

where I_i is the spin of nucleus i, and we are working on the assumption that the other spins in i are initially unpolarised[11]. The muon spin operator is now also the Kronecker product of that of the isolated muon and the identity matrix,

$$\sigma_{\mu}^{\sigma}(0) = \sigma^{\sigma} \otimes \left[\bigotimes_i \mathbb{1}_{2I_i+1} \right]. \tag{2.18}$$

For these cases, it is simplest to time-evolve this spin operator σ_{μ}^{σ} rather than the density matrix (i.e. switching to the Heisenberg picture), so

$$\sigma_{\mu}^{\sigma}(t) = e^{i\mathcal{H}t} \sigma_{\mu}^{\sigma}(0) e^{-i\mathcal{H}t}, \tag{2.19}$$

and the time evolution of the muon polarisation is now

$$P_{\mu}^{\sigma}(t) = \mathrm{Tr}[\rho(0)\sigma_{\mu}^{\sigma}(t)] = \frac{1}{2\prod_i (2I_i + 1)} \mathrm{Tr}[\sigma_{\mu}^{\sigma}(0)\sigma_{\mu}^{\sigma}(t)], \tag{2.20}$$

[11] This is the infinite-temperature limit of the thermal density matrix, an approximation that holds well for nuclei as they are often completely unpolarised as $\mu_{\mathrm{N}} B \ll k_{\mathrm{B}} T$ for any reasonable temperature and magnetic field one would measure in a muon experiment.

where the density matrix is substituted with Eq. (2.17), noting that all Pauli spin matrices are traceless which removes the identity term. Conventionally, for single crystal samples the muon is initially polarised and measured in the z direction, hence the superscript $\sigma = z$.

2.2.3 Polycrystalline samples

Often in μSR polycrystalline magnetic samples are measured, where the angle between the magnetic field and the muon polarisation is equally likely to be in any direction on the unit sphere. To calculate the expected muon polarisation $P_\mu^{\text{avg}}(t)$ in this case, it is easiest to set up the coordinates such that the Hamiltonian is constant, and instead allowing the density matrix and the spin measurement operator to rotate[12]. The simplest way to calculate this is by continuing in the Heisenberg picture of time evolution, and hence we can calculate the angular average of the muon polarisation as

$$P_\mu^{\text{avg}}(t) = \frac{1}{4\pi}\int_{\theta=0}^{\pi}\int_{\phi=0}^{2\pi} \text{Tr}[\rho_\mu^{\theta,\phi}(0)\sigma_\mu^{\theta,\phi}(t)]\sin\theta \text{d}\theta\text{d}\phi. \tag{2.21}$$

By noting, due to Pauli spin matrices being traceless,

$$\begin{aligned}\text{Tr}[\rho_\mu^{\theta,\phi}(0)\sigma_\mu^{\theta,\phi}(t)] &= \text{Tr}\Big[\frac{1}{2}(\mathbb{1} + \sigma_\mu^{\theta,\phi}(0))\sigma_\mu^{\theta,\phi}(t)\Big] &(2.22)\\ &= \frac{1}{2}\text{Tr}[(\sigma_\mu^x(0)\sin\theta\cos\phi + \sigma_\mu^y(0)\sin\theta\sin\phi + \sigma_\mu^z(0)\cos\theta) \\ &\qquad \cdot (\sigma_\mu^x(t)\sin\theta\cos\phi + \sigma_\mu^y(t)\sin\theta\sin\phi + \sigma_\mu^z(t)\cos\theta)], &(2.23)\end{aligned}$$

and that the only terms which are non-zero in the integral have only even powers of either $\cos\phi$ or $\sin\phi$ (which discounts all the products of Pauli spin matrices in different directions), this reduces to

$$\begin{aligned}P_\mu^{\text{avg}}(t) = \frac{1}{4\pi}\int_{\theta=0}^{\pi}\int_{\phi=0}^{2\pi} \frac{1}{2}\text{Tr}[&\sigma_\mu^x(0)\sigma_\mu^x(t)\sin^2\theta\cos^2\phi \\ &+ \sigma_\mu^y(0)\sigma_\mu^y(t)\sin^2\theta\sin^2\phi \\ &+ \sigma_\mu^z(0)\sigma_\mu^z(t)\cos^2\theta]\sin\theta\text{d}\theta\text{d}\phi.\end{aligned} \tag{2.24}$$

[12]You can imagine this as keeping the sample fixed while the instrument rotates around it, which is equivalent to the sample rotating with the instrument fixed in place.

Calculating the integrals,

$$P_\mu^{\text{avg}}(t) = \frac{1}{3}\Big(\frac{1}{2}\text{Tr}[\sigma_\mu^x(0)\sigma_\mu^x(t)] + \frac{1}{2}\text{Tr}[\sigma_\mu^y(0)\sigma_\mu^y(t)] + \frac{1}{2}\text{Tr}[\sigma_\mu^z(0)\sigma_\mu^z(t)]\Big). \tag{2.25}$$

Defining $P_\mu^\sigma(t) = \text{Tr}[\rho_\mu(0)\sigma_\mu^\sigma(t)] = \text{Tr}[\rho_\mu(t)\sigma_\mu^\sigma(0)]$ in the spirit of Equation (2.8), we obtain

$$P_\mu^{\text{avg}}(t) = \frac{1}{3}\Big(P_\mu^x(t) + P_\mu^y(t) + P_\mu^z(t)\Big). \tag{2.26}$$

This means that to calculate the muon polarisation for a muon in a polycrystalline sample, one just needs to take the average of the polarisation from any three perpendicular directions. This property works for any Hamiltonian, as long as the initial muon polarisation is independent of the Hamiltonian (which is not the case for LF- or TF-μSR).

3

The Muon Site Problem, DFT+μ, and Fluorides

Contents

3.1 Introduction to the muon site problem 19
3.2 DFT+μ 20
3.2.1 Density functional theory: an overview 20
3.2.2 DFT+μ: using DFT to find muon sites 24
3.3 Fluorides 26

3.1 Introduction to the muon site problem

In Chapter 2 and in Appendix A, I showed how a muon in a magnetic field precesses at a frequency proportional to the magnitude of its local magnetic field (Larmor precession). Although the model considered in the previous chapter provides an explanation for the muon precession one observes in experiments, in real samples the magnetic field is a function of the muon stopping site, and often varies dramatically on this. Therefore, in order to quantitatively analyse muon data, knowledge of the muon stopping site is essential. There are several methods of calculating muon sites: one can use Bayesian methods if the probability of the muon stopping in various sites can be quantified [45], density functional theory (DFT+μ), or by taking

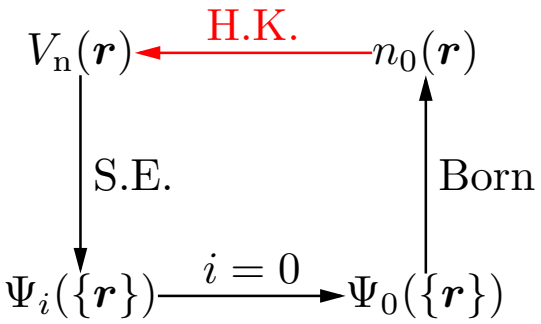


Figure 3.1: The Hohenberg–Kohn theorem. Starting from the top-left, if one defines the external potential of the electrons due to the nuclei, V_{n}, one can use the Schrödinger equation (S.E.) to calculate the electronic eigenstates $\Psi_i(\{\boldsymbol{r}\})$, and hence their ground states $\Psi_0(\{\boldsymbol{r}\})$. One can then use Born's result of the particle density being the modulus of the wavefunction squared [48], to obtain the ground state electronic density $n_0(\boldsymbol{r})$. The Hohenberg–Kohn theorem (in red) states that it is possible, with *just* the ground state electron density, to obtain V_{n}. Figure adapted from Ref. [47].

advantage of samples which affect the muon polarisation in such a way that the muon site can be determined by a careful analysis of the data. This chapter will only focus on the latter two methods, which tend to be the most widely used in practice.

3.2 DFT+μ

3.2.1 Density functional theory: an overview

Density functional theory (DFT) is a technique which is based upon the Hohenberg–Kohn theorem [46]. This theorem states the following (adapted from Ref. [47]):

- The ground state particle density, $n_0(\boldsymbol{r})$ determines *uniquely* the external potential of the particles (which, in this case, is the potential due to the nuclei $V_{\mathrm{n}}(\boldsymbol{r})$).

- The energy can be calculated by a universal functional in terms of the density, i.e $E = F[n]$ for any external potential $V_{\mathrm{n}}(\boldsymbol{r})$. The ground state energy is the global minimum of this functional, and the ground state density $n_0(\boldsymbol{r})$ is the corresponding particle density that produces this minimum.

Another way of understanding this theorem is by looking at Figure 3.1, adapted from Ref. [47]. Usually in quantum mechanics, if one has a potential, using the

Schrödinger equation it is possible (in principle) to calculate all the eigenstates of the system[1]. From this, the ground state can be determined, and hence the ground state electron density. The Hohenberg–Kohn theorem states that, if one starts from the ground state electron density, it is possible to calculate the potential, completing the loop.

The total energy functional of a solid state system is

$$E = F[n] = \int d\boldsymbol{r} n(\boldsymbol{r}) V_{\mathrm{n}}(\boldsymbol{r}) - \sum_i \int d\boldsymbol{r} \phi_i^*(\boldsymbol{r}) \frac{\nabla^2}{2} \phi_i(\boldsymbol{r}) + \frac{1}{2} \int \int d\boldsymbol{r} d\boldsymbol{r'} \frac{n(\boldsymbol{r}) n(\boldsymbol{r'})}{|\boldsymbol{r} - \boldsymbol{r'}|} + E_{\mathrm{xc}}[n], \tag{3.1}$$

in Hartree units[2] where the first term is due to the electron–nuclear Coulomb interaction, the second term the kinetic energy of the electrons, the third term is the Hartree energy (the average coulomb repulsion between the electrons) and the final term is the exchange and correlation energy functional. $\phi_i(\boldsymbol{r})$ are the single-electron Kohn–Sham wavefunctions, which are generated by solving the single particle equation

$$\Big[-\frac{1}{2}\nabla^2 + V_{\mathrm{n}}(\boldsymbol{r}) + V_{\mathrm{H}}(\boldsymbol{r}) + V_{\mathrm{xc}}[n](\boldsymbol{r}) \Big] \phi_i(\boldsymbol{r}) = E_i \phi_i(\boldsymbol{r}), \tag{3.2}$$

where $V_{\mathrm{xc}}[n](\boldsymbol{r})$ is generated by calculating the functional derivative of $E_{\mathrm{xc}}[n]$, i.e.

$$V_{\mathrm{xc}}[n](\boldsymbol{r}) = \left. \frac{\delta E_{\mathrm{xc}}[n]}{\delta n} \right|_{n(\boldsymbol{r})}. \tag{3.3}$$

Note that the key point of Kohn-Sham's theory is that each of the electrons can be treated independently, with the other electrons being taken into account by means of effective potentials. If all the effective potentials were known exactly, then DFT would be an exact method of calculating the properties of materials.

The exchange and correlation energy functional $E_{\mathrm{xc}}[n]$ in Equation 3.1 is not known exactly; instead approximations have to be utilised [49]. The simplest approximation used is the Local Density Approximation (LDA) (and the similar,

[1] Although it is possible in principle, it is rarely practical to do so!

[2] When discussing DFT, I will use Hartree units for convenience. This means lengths are in units of Bohr (1 Bohr $\approx$ 0.5292 Å), masses are in a.u. (1 a.u. $\approx 9.109 \times 10^{-31}$ kg), and energies are in Ha (1 Ha $\approx$ 27.21 eV).

but more general Local Spin Density (LSD) approximation[3]), which uses ideas from the theory of a uniform electron gas. Specifically, the exchange energy is

$$E_{\mathrm{x}}[n] = -\frac{3}{4}\left(\frac{3}{\pi}\right)^{\frac{1}{3}} n^{\frac{4}{3}} V, \tag{3.4}$$

and the exchange potential obtained from this using Eq. (3.3) depends only on the electron density at the position in space $\boldsymbol{r}$ in question. In this scheme, the correlation energy is calculated with a parameterised approach due to Perdew and Zunger [50]. This approximation works well for systems where the electron density varies over a longer length scale than the Fermi wavelength, which for many systems is not the case. Nevertheless, it can predict bond lengths to an accuracy of around 2-3% [49] (tending to underestimate them in many cases [51, 52]), despite it being relatively simple functional. An improved functional for the exchange and correlation energy is given by the Generalised Gradient Approximation (GGA), where the functional is of *both* the electron density and its gradient [53]. The functional due to Perdew, Burke and Ernzerhof (PBE) is one of the most widely used GGA functionals, and provides a significant improvement over LDA and LSD for the calculation of many physical properties [54, 55]. In all of the DFT calculations in this thesis, I use the PBE functional unless stated otherwise.

In practice, most DFT codes use the self-consistency method, which makes use of the following Kohn–Sham equations,

$$\nabla^2 V_{\mathrm{H}}(\boldsymbol{r}) = -4\pi n(\boldsymbol{r}), \tag{3.5a}$$

$$V_{\mathrm{n}}(\boldsymbol{r}) = -\sum_I \frac{Z_I}{|\boldsymbol{r} - \boldsymbol{R}_I|}, \tag{3.5b}$$

$$V_{\mathrm{xc}}[n](\boldsymbol{r}) = \left.\frac{\delta E_{\mathrm{xc}}[n]}{\delta n}\right|_{n(\boldsymbol{r})}, \tag{3.5c}$$

$$\left[-\frac{1}{2}\nabla^2 + V_{\mathrm{n}}(\boldsymbol{r}) + V_{\mathrm{H}}(\boldsymbol{r}) + V_{\mathrm{xc}}[n](\boldsymbol{r})\right]\phi_i(\boldsymbol{r}) = E_i\phi_i(\boldsymbol{r}), \tag{3.5d}$$

$$n(\boldsymbol{r}) = \sum_i |\phi_i(\boldsymbol{r})|^2, \tag{3.5e}$$

and calculates the electron density with the following steps:

[3]The difference between LDA and LSD is that LSD treats the spin up and spin down electron densities separately; whereas LDA makes no distinction between the two states.

1. Guess the electron density (using the atomic electron wavefunctions), $n(\boldsymbol{r})$
2. Calculate $V_{\mathrm{H}}(\boldsymbol{r})$, by solving (3.5a)
3. Calculate $V_{\mathrm{xc}}[n](\boldsymbol{r})$, by calculating the functional derivative of the exchange and correlation energy using the electron density, Eq. (3.5c)
4. Calculate the nuclear potential (3.5b), and use this with the new exchange and correlation potential $V_{\mathrm{xc}}[n](\boldsymbol{r})$ to solve the Schrödinger equation (Eq. (3.5d)) to find the Kohn–Sham wavefunctions $\phi_i(\boldsymbol{r})$
5. Use the Kohn–Sham wavefunctions to re-calculate the electron density $n'(\boldsymbol{r})$, using Eq. (3.5e)
6. If $n(\boldsymbol{r}) \approx n'(\boldsymbol{r})$ within a tolerance, quit. Otherwise, go to step 2, using the new density $n(\boldsymbol{r}) = n'(\boldsymbol{r})$

Using the above method, with a suitable approximation for the exchange and correlation potential $V_{\mathrm{xc}}[n](\boldsymbol{r})$, one can calculate the total energy and hence many other properties of materials from first principles, to an impressive accuracy.

For all but the smallest atoms, calculating the wavefunction of all the electrons is unnecessary and computationally expensive, so often pseudopotentials are used. These allow one to approximate the core electrons by assuming their wavefunctions are the same as they are in the isolated atoms [56], and hence only the valence electrons (which dominate the physics) need to be described by the Kohn–Sham wavefunctions.

DFT can also be used to calculate the forces on the atoms, as the force on each atom at position $\boldsymbol{R}_I$ is $\boldsymbol{F}_I = \frac{\partial E(\{\boldsymbol{R}_I\})}{\partial \boldsymbol{R}_I}$. Calculating this derivative for N atoms would require $3N+1$ calculations of the energy (and hence the electron density n) with DFT, which would take a prohibitively large amount of time. Instead, one can make use of the Hellmann–Feynman theorem [57, 58], which states that for any parameter λ,

$$\frac{\partial E}{\partial \lambda} = \left\langle \psi \middle| \frac{\partial \mathcal{H}}{\partial \lambda} \middle| \psi \right\rangle, \tag{3.6}$$

and hence the forces on the nuclei can be found by differentiating Equation (3.1) (with an additional term to account for Coulomb interactions between the nuclei) with respect to nuclear position $\boldsymbol{R}_I$,

$$\boldsymbol{F}_I = \int \mathrm{d}\boldsymbol{r} n(\boldsymbol{r}) \frac{Z_I(\boldsymbol{r} - \boldsymbol{R}_I)}{|\boldsymbol{r} - \boldsymbol{R}_I|^3} + \sum_{i \neq I} \frac{Z_I Z_i (\boldsymbol{R}_I - \boldsymbol{R}_i)}{|\boldsymbol{R}_I - \boldsymbol{R}_i|^3}. \tag{3.7}$$

This means that in order to calculate the forces on all the nuclei, the electron density $n(\boldsymbol{r})$ only needs to be calculated once, which considerably speeds up the calculation when compared to the the simple numerical derivative method. Hence, to calculate the equilibrium structure of the material in question one can calculate the force on each of the nuclei, move them in the direction of their forces by a small amount, and re-calculate the electron density until the forces on all the atoms are below a desired threshold.

This method relies on the Born-Oppenheimer approximation, which assumes that the total wavefunction of the system can be written as a product of the electronic and nuclear wavefunctions, leading to separate Schrödinger equations for both [59]. The electrons are taken into account in the nuclear Schrödinger equation with an effective potential term, which in effect assumes that the nuclei move so slowly the electrons are always in the ground state, regardless of the nuclear positions. This approximation works since the electron mass is much smaller than the mass of a nucleon, meaning that the nuclei have a much more localised wavefunction which means that the effects of zero-point motion is negligible.

3.2.2 DFT+μ: using DFT to find muon sites

The technique of DFT+μ was pioneered by the Oxford muon group in 2013 [60], and the Parma group independently at the same time [61], where both groups successfully used DFT to calculate the muon stopping site in fluoride insulators. To this extent, the method used was to generate supercells of the structure to be analysed, and a muon was placed in lots of random positions in separate supercells. The muon in this case was modelled as a light hydrogen ion, by using a hydrogen pseudopotential and setting a charge of $+|e|$ on the supercell. All the atoms and

the muon were then relaxed[4] until the equilibrium positions were found. Then, the total energy of each of the final muon positions within the supercell were compared, and the one with the lowest energy was taken as the most likely muon site.

This method has been used very successfully to calculate the muon site in a range of fluorides [60, 61], and magnetic materials [64], and has allowed for a more quantitative analysis of μSR data. However, although predictions of the muon-induced distortion of the atoms obtained by DFT have been used to provide additional insights into their effects in μSR experiments [65], the extent of the distortions are predicted to an accuracy of about 5%, which can be significant when utilising DFT for the analysis of some compounds, as I will show later. Another disadvantage of DFT+μ is that the calculations often require significant computational resources, especially for state-of-the-art materials which tend to have atomic species with a large number of electrons, many of which cannot be treated as core electrons in the pseudopotentials[5].

In some circumstances, especially for atoms with f electrons (where many of the electrons need to be treated as valence), a full DFT+μ approach is not possible, as the computational resources required are too large, especially if one implants a muon in a supercell. In these cases, a rough estimate of the likely muon position can be obtained by calculating the total potential of the crystal as a function of position in the unit cell. An example of this is in Figure 3.2, for the compound UTe_2 (note that in this figure, the sign of the potential is for electrons – so a positively charged muon would need to go to the *maximum* of this potential to minimise its energy). UTe_2, due to uranium being a 5f ion, is too computationally challenging to perform DFT+μ on, but the figure shows that the position of the muon is likely to be $(0.44, 0, 0.5)$ in fractional coordinates. There can be some discrepancy between the muon site calculated by considering just the potential

[4]Treating a muon as a light hydrogen ion in DFT assumes that its zero-point motion is negligible, an approximation that works as the mass of a muon is around 200 times greater than an electron. The effect of muonic zero-point motion in μSR has been dealt with in detail in Refs. [62, 63].

[5]A DFT+μ calculation, on average, takes about 3 days on around 50 nodes on a modern cluster.

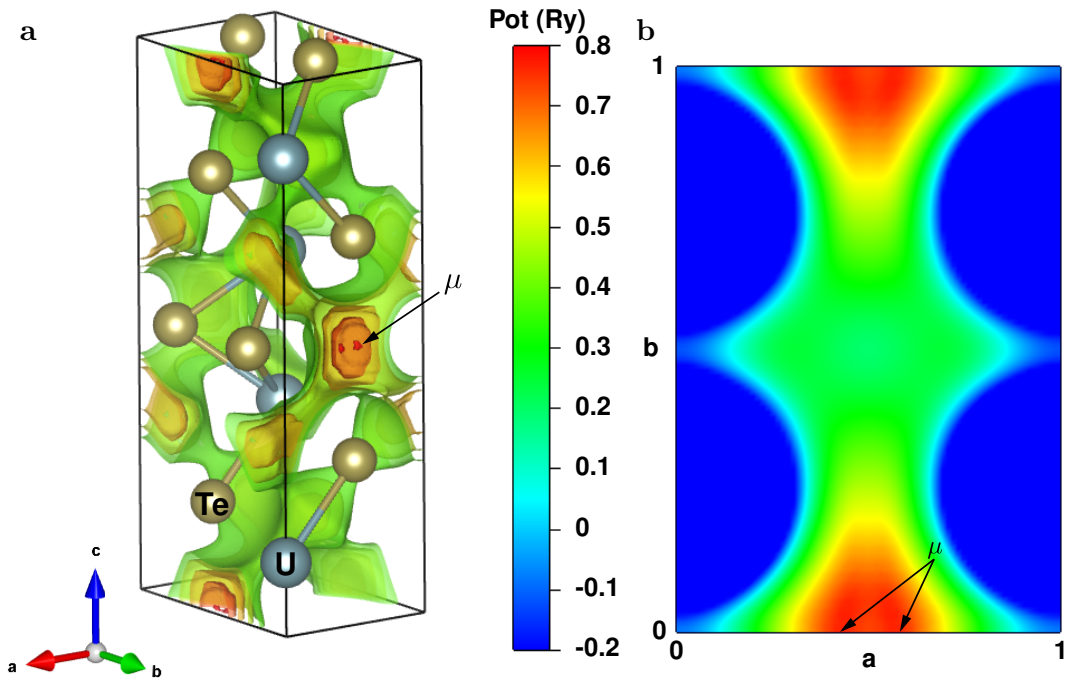


Figure 3.2: Muon sites in UTe_2. **a** shows the contours of the total potential, calculated with DFT (note that energies lower than 0.4 Ry are not shaded for visual clarity). **b** shows this same potential, across a plane perpendicular to the c axis, with $c = \frac{1}{2}$. Both subfigures have the energies shaded according to the legend in the centre of the figure.

and those calculated with a 'full' DFT+μ approach, as it fails to take into account the perturbations of the muon on the surrounding atoms, but it nevertheless can give a rough guide as to the likely stopping location [66].

3.3 Fluorides

Using DFT+μ to calculate muon sites can be resource-intensive and the technique sometimes fails to calculate the muon site to a high degree of accuracy. Sometimes, however, the muon site can be derived through the analysis of the data itself (rather than the other way around; that is using the muon site to analyse the data). One particular class of materials where this is very apparent is fluorides: J. H. Brewer et al. discovered in 1986 [67] that a muon in an ionic fluoride insulator is strongly attracted to the negatively-charged fluoride ions, owing to the positive charge of the muon and the strong electronegativity of the fluorides, and an F–μ–F "molecule" is formed. The muon then interacts with its environment through the magnetic

dipole-dipole interaction, with the Hamiltonian (in S.I. units)

$$\mathcal{H} = \sum_{i<j} \frac{\mu_0 \gamma_i \gamma_j}{4\pi |\boldsymbol{r_{ij}}|^3} (\boldsymbol{s}_i \cdot \boldsymbol{s}_j - 3(\boldsymbol{s}_i \cdot \hat{\boldsymbol{r}}_i)(\boldsymbol{s}_j \cdot \hat{\boldsymbol{r}}_j)), \tag{3.8}$$

where the sum indices i and j represent the nuclei and the muon, γ_i is the gyromagnetic ratio for nucleus (or muon) i, and $\boldsymbol{r}_{ij}$ is the displacement vector between spins i and j. Because this Hamiltonian is strongly dependant on the inter-spin displacement vector $\boldsymbol{r}_{ij}$, the muon polarisation (calculated by substituting Equation (3.8) into (2.7) and (2.26)) changes significantly with the inter-spin distances which therefore can be easily derived by fitting these to the muon asymmetry data. The muon polarisation derived by Brewer et al. [67] to fit a range of ionic fluorides took Equation (3.8) and restricted the sum to only nearest-neighbour interactions, assuming a linear F–μ–F "molecule", giving

$$P_\mu(t) = \frac{1}{6}\Bigg\{3 + \cos\Big(\sqrt{3}\omega_\mathrm{D} t\Big) + \left(1 - \frac{1}{\sqrt{3}}\right)\cos\left[\left(\frac{3-\sqrt{3}}{2}\right)\omega_\mathrm{D} t\right] + \left(1 + \frac{1}{\sqrt{3}}\right)\cos\left[\left(\frac{3+\sqrt{3}}{2}\right)\omega_\mathrm{D} t\right]\Bigg\}, \tag{3.9}$$

with $\omega_\mathrm{D} = \hbar\mu_0\gamma_\mu\gamma_\mathrm{F}/(4\pi r_{\mathrm{F}\mu}^3)$. The derivation of this function is in Appendix B. This function, however, does not by itself provide an adequate fit to the data, which can be seen in Figure 3.3 for the case of NaF: adequate fits require multiplying Equation (3.9) by a phenomenological "stretched exponential" function, that is $\exp\Big(-(\lambda t)^\beta\Big)$, with β chosen to be 1.5. This results in a fit which is visually better – but the lack of a physical basis for this relaxation function means it provides no insight as to the physical cause of this relaxation.

J. H. Brewer et al., in another publication in the same year [68], performed calculations of the muon polarisation in NaF, on an improved model that took into account the nearest-neighbour Na cations in addition to the nearest fluorines. Although such a method worked well for the dataset they measured (which had significant errors at about 8 μs), to understand the relaxation fully one needs data of higher statistics, and a method of including *all* the nuclei in the system.

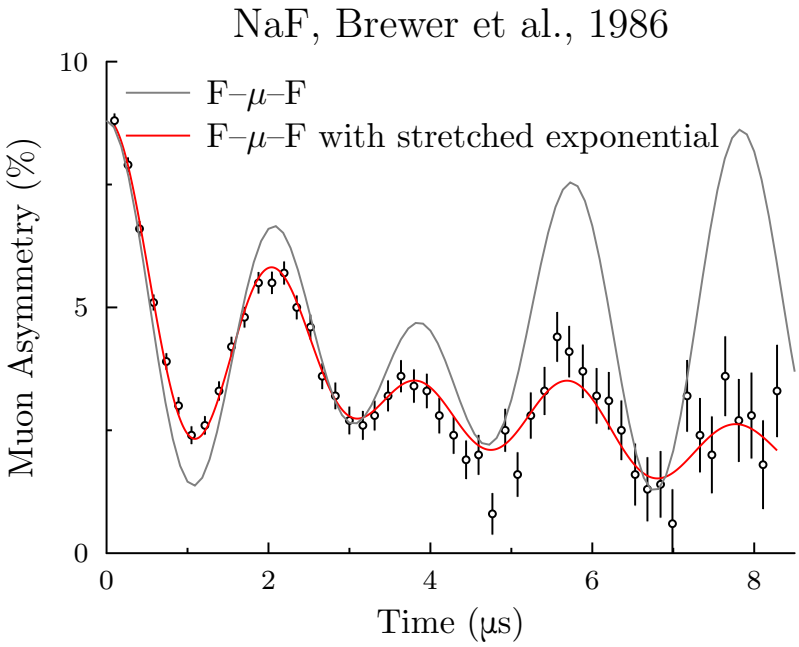


Figure 3.3: Results of J. H. Brewer et al.'s NaF μSR experiment, showing the fits produced by the F–μ–F function (Equation (3.9), grey line), and that produced by the F–μ–F function multiplied by a stretched exponential function with $\beta = 1.5$ (red line). Data and fit reproduced from Ref. [67].

F–μ–F states have since been investigated in a range of other ionic fluorides by Noakes et al. [69], which, despite producing pleasing fits, also introduces a range of phenomenological relaxation functions to match the data, severely limiting the insight that can be obtained from the analysis. This paper was also the first to report an additional relaxation in the baseline asymmetry, the origin of which was unclear.

F–μ–F states were later measured on a range of polyfluorocarbons in 2003, by K. Nishiyama et al. [70]. Their analysis tried to describe the relaxation of the oscillating component by fitting to a dynamical model, where the muon undergoes diffusion between different sites, described by the strong collision model[6] [72, 73]. However, such a treatment gave unusually large values for the hopping rate (0.1 μs^{-1}) at a temperature of 5 K), and still required a phenomenological relaxation function to describe the data fully. At the same time, F. L. Pratt et al. [74] undertook a

[6]The strong collision model assumes that muon hopping is a Markovian process, with a fixed probability per unit time and the environment of the muon after the hop event is completely independent of the environment of the muon before [71].

study of the polymer PTFE, also describing the relaxation using a dynamical model. Utilising dynamics in such a way when the static polarisation is not fully understood means the muonic hopping rate is likely to be incorrect (and, in these cases, possibly overestimated as the static polarisation underestimates the extent of the relaxation).

In 2007, T. Lancaster et al. from the Oxford muon group extended the analysis of F–μ–F states further, by utilising the dependence of the spectrum on the F–μ–F bond angle to determine muon sites in a range of molecular magnets [75]. These sites were determined to a high accuracy without needing to carry out electronic structure calculations, despite the Hamiltonian for each of the cases only including the muon and two nearest-neighbours. It was also possible to identify a muon state of the form F–μ–H, where a nearby hydrogen nucleus affected the muon polarisation to a significant degree.

In the same year, the Oxford group also measured the compound Cs_2AgF_4 using μSR [76], where they found evidence of magnetic order below $T_c \approx 14$ K, and F–μ–F oscillations at temperatures above. Two muon sites were predicted due to the two magnetic frequencies observed below the critical temperature, the locations of which were estimated by considering the shape of the F–μ–F complex. A similar study was undertaken on a range of multiferroic fluorides in 2010 by A. Potočik et al. [77], where again the shape of the F–μ–F bond was utilised to predict the muon stopping site, where it was found that the site was linear and symmetric about the muon. In both cases, it was assumed that below T_c, the magnetic field due to the ordered electronic moments was the sole cause of the muon precession, and therefore the fluorine nuclear moments only affect the μSR spectrum at temperatures above the magnetic transition.

Muon states which evolve due to the magnetic dipole-dipole Hamiltonian (Eq. (3.8)) have been discovered in a range of other systems [78, 79]. However, it is most commonly observed in fluorides, as fluorine is the most electronegative element and the bonds it forms in compounds are often of a highly ionic character.

All the cases discussed above required a phenomenological stretched exponential decay function to be multiplied by the coherent F–μ–F oscillations, of a similar form

to that used by Brewer et al. Such an approach however never *quite* matches the data as closely as perhaps one would like, and the parameters obtained from the stretched exponential relaxation can neither be derived from the physics of the material nor can they be used to measure its physical properties. Therefore, we require a deeper theory of the relaxation of these states that can describe the data fully.

This chapter is based on Phys. Rev. Lett. **125** *087201 (2020) (Ref. [80])*

4

Decoherence and the Muon Site Problem: A Study of CaF_2 and NaF

Contents

4.1 Introduction **31**
4.2 Quantum information in F–μ–F states **34**
4.3 CaF_2: a model system **38**
4.4 NaF: a model quadrupolar system **44**
4.5 Low-energy muons and fluoride states **46**
4.6 Conclusion **48**

4.1 Introduction

An important issue in the study of quantum mechanics is the interaction between a *system*, $\mathcal{S}$, considered as a few coupled quantum objects evolving in a manner described by some well-defined Hamiltonian, and its *environment*, $\mathcal{E}$, considered as a large bath consisting of many quantum objects. The role of the environment is to act as a source of decoherence [81] whereby quantum information, stored in the system and in principle readable from it, is degraded and leaks out into the environment where it can no longer be discovered. If the system and environment could be considered together as a single system, $\mathcal{S} \otimes \mathcal{E}$, this larger system would undergo

unitary evolution and its von Neumann entropy, $S = -\mathrm{Tr}\rho \log_2 \rho$, where ρ is the density matrix of the $\mathcal{S} \otimes \mathcal{E}$ composite object, would be constant. However, one is rarely permitted this holistic view and is restricted to monitoring the reduced density matrix of the system, $\rho_{\mathcal{S}} = \mathrm{Tr}_{\mathcal{E}}\rho$, obtained by tracing out the degrees of freedom of the environment [82], and the entropy of $\mathcal{S}$ will tend to increase with time [83].

One scenario where this is very apparent is the F–μ–F state introduced in Section 3.3, where the time evolution of the muon's polarisation is governed by the dipolar Hamiltonian in Equation (3.8). This dipolar interaction between a single fluorine nuclear spin and a muon would result in the energy level spectrum shown in Figure 4.1**a**, while for two fluorine nuclear spins (the F–μ–F state), the spectrum is shown in Figure 4.1**b** (the case used by J. H. Brewer in Ref. [67], Eq. (3.9)). In both cases, the distinctive beating pattern of oscillations in the time-dependence of the muon polarisation $P_\mu^z(t)$ occurs because of quantum interference between these energy eigenstates, an effect which can be interpreted as a coherent exchange of spin polarisation between the initially polarised muon and the initially unpolarised fluorine nuclei. These oscillations are shown in Figure 4.1**c**, which are of the same origin as Equation (3.9) (but include the small F–F interaction). However, as discussed in Section 3.3, previously good fits to the experimental data require multiplying the calculated coherent precession signals by a phenomenological relaxation function, often a stretched exponential, the parameters of which have no theoretical basis. A master equation approach could be used to model the non-unitary evolution of the reduced density matrix of the system [84], but this would still involve an arbitrary parameter quantifying the system–environment coupling. This chapter will show how an exact treatment is possible which includes the known couplings between the muon and more distant fluorine nuclei, thereby accurately modelling the *environment* of the F–μ–F *system*. These couplings result in a relaxation of the precession signal [solid line in Figure 4.1**c**] that completely accounts for the data and confirms electronic structure calculations of the muon site [60, 61].

The effects of interactions with more distant fluorine nuclei can be understood by examining the energy eigenvalues shown in Figure 4.1**d** where the eight next-

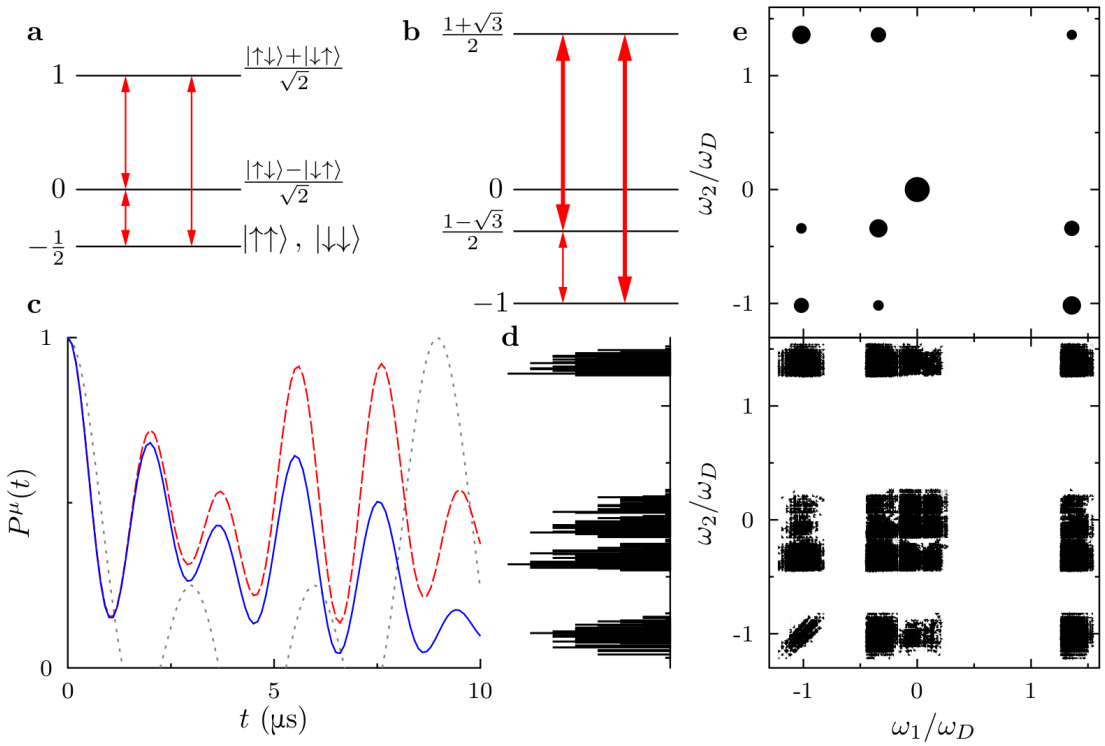


Figure 4.1: Energy levels in F–μ–F states. a The energy levels in an F–μ coupled state. The eigenstates are labelled by the spins of the muon and the fluorine nucleus. The red arrows link levels between which quantum-mechanical interference can occur and the energies are in units of $\hbar\omega_D = \hbar^2\mu_0\gamma_\mu\gamma_F/(4\pi r^3)$. **b** The energy levels for an F–μ–F state, also showing possible interferences (thicker lines connect energy levels between which there is the largest amplitude of quantum interference). The energy eigenvalues are very slightly different from those shown once the small F–F dipolar coupling is included, as will be done in all subsequent plots. **c** The time-dependence of the muon polarisation $P^\mu(t)$ for isolated F–μ (dotted line), isolated F–μ–F (dashed line) and for F–μ–F also coupled to eight next-nearest-neighbour fluorine nuclear spins appropriate for the fluorite structure (blue line). These simulations are for an experiment in zero applied magnetic field, and assume a polycrystalline average over all possible orientations of the F–μ or F–μ–F species. **d** Energy levels for the F–μ–F state including next-nearest-neighbour fluorine nuclear spins. **e** Interference amplitude for isolated F–μ–F (top panel) and with the next-nearest-neighbour couplings (bottom panel). The amplitude of the quantum interference between energy levels $\hbar\omega_1$ and $\hbar\omega_2$ is represented by the relative areas of the points in the top panel and by a grey scale in the bottom panel. The energy scales of **b** and **d** are lined up with these two panels.

nearest-neighbour (nnn) couplings that occur in the fluorite structure[1] have also been included (analogous effects will occur in other fluoride crystal structures, which I will show in subsequent chapters). The four energy levels in isolated F–μ–F are

[1] A fluorite structure can be understood as a simple cubic arrangement of fluoride ions, with cations in the centre of alternate cubes of anions.

broadened by the nnn couplings into four bands of energy levels. The coherences between these energy levels are shown in the two-dimensional plots in Figure 4.1**e**, where the size of the point indicates the amplitude of the interference term between energy levels $\hbar\omega_1$ to $\hbar\omega_2$. These diagrams are reminiscent of two-dimensional NMR plots [85], but here there are no radiofrequency pulses and the interference between levels happen automatically in the unitary evolution of the quantum state. Thus, the overall structure for isolated F–μ–F in the upper panel is largely retained in the lower panel when including the more distant couplings, but a richer frequency spectrum results and this mixture of frequencies is responsible for the dephasing of the precession signal observed in experiments.

4.2 Quantum information in F–μ–F states

In order to understand the broadening of the energy bands in Figure 4.1**e**, I now calculate the time-dependence of the von Neumann entropy. I consider the three cases again: (i) the F–μ state; (ii) the F–μ–F state; and (iii) the F–μ–F state with eight nnn fluorine nuclei, appropriate for the fluorite structure [86]. The von Neumann entropy for these states remains constant at $S = N_{\mathrm{F}}$ as the states evolve unitarily, where N_{F} is the number of fluorine nuclei in the cluster ($N_{\mathrm{F}} = 1,\ 2$ and 10 for the three cases respectively). This is because the implanted muon is initially spin-polarised and hence in a pure state, but the fluorine nuclei are initially unpolarised. By tracing out the fluorine or muon degrees of freedom, it is possible to calculate the muon and fluorine reduced entropies, S_μ and S_{F} as a function of time, see Figure 4.2. This figure shows the time-dependence of the muon polarisation $P_\mu^z(t)$, the muon entropy S_μ (obtained by tracing out all the other spins), and the entropy of the entire fluorine system, S_{F} (note that $S_{\mathrm{F}}(t = 0) = N_{\mathrm{F}}$, and, following convention, von Neumann entropies use $\log_2$, so that information is measured in bits). These are plotted for the three cases of isolated F–μ, isolated F–μ–F and environmentally decohering F–μ–F. The coupling between the muon and its fluoride environment results in the muon oscillating between being in a completely pure ($S_\mu = 0$) and mixed ($S_\mu > 0$) state, with the fluorine subsystem oscillating in

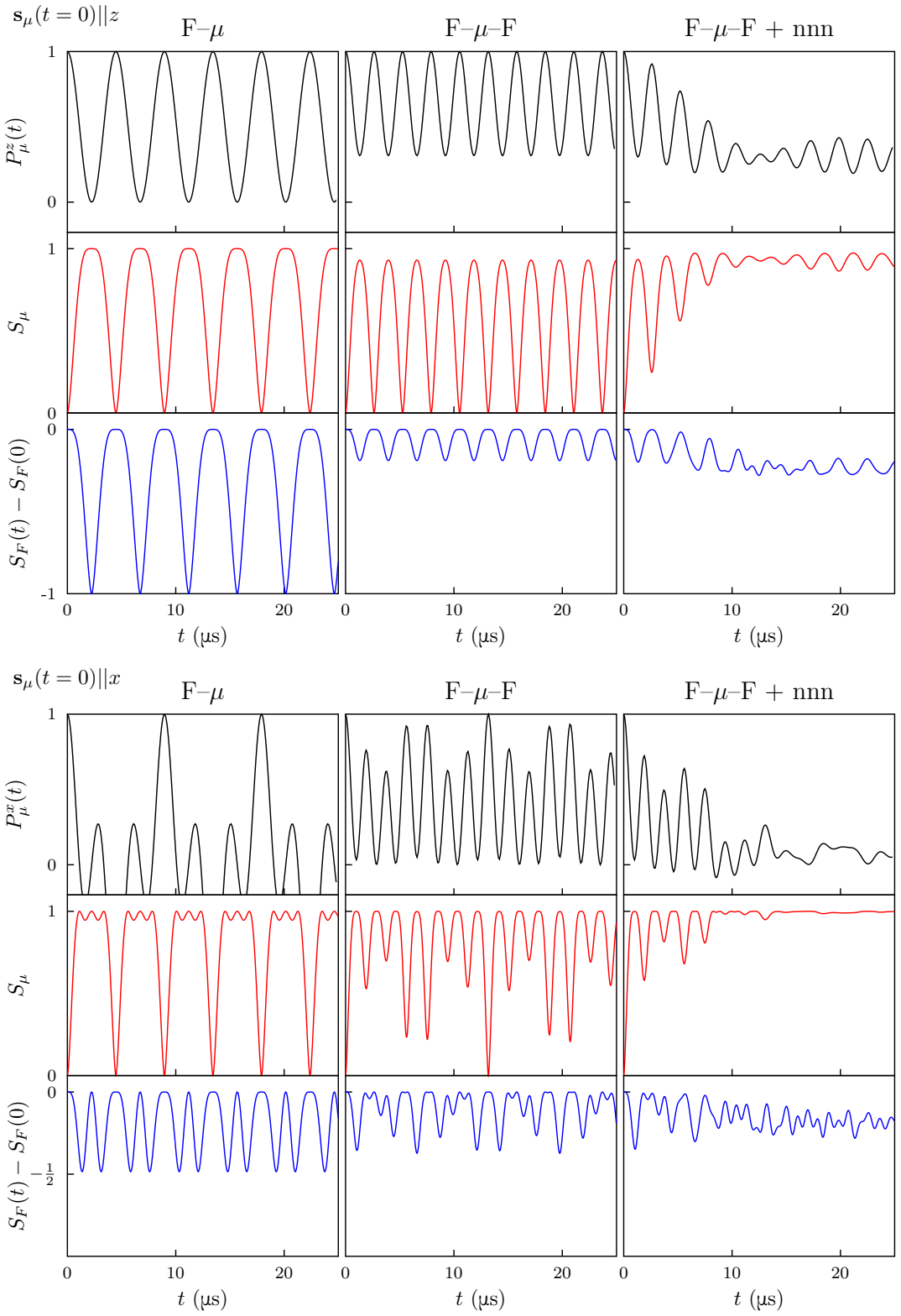


Figure 4.2: von Neumann entropy for muon–fluorine states. The top panel shows the case when the initial muon polarisation is aligned along z (defined as the vector linking the muon with its nearest-neighbour fluorine). The bottom panel shows the case of the initial muon polarisation perpendicular to this vector (x).

antiphase. This can be interpreted in terms of quantum information exchanging back and forth between the muon and the fluorine subsystem; $P_\mu^z(t)$ and $P_\mu^x(t)$ reach a maximum whenever information is stored on the muon, and a minimum whenever it is residing in the fluoride subsystem. For F–μ, there are times when the muon is in a completely mixed state and the fluorine nucleus is in a completely pure state, but for F–μ–F the fluoride subsystem never evolves into a pure state. However, for both F–μ and F–μ–F the muon periodically returns to a completely pure state ($S_\mu = 0$) and the quantum information is therefore never completely lost.

However, when the effect of the eight additional nnn fluorines is included, the muon never recovers to a pure state within the timescale of a typical muon experiment (25 μs). Thus the eight nnn fluorines act as a source of decoherence, so that information transferred from the muon remains in this subsystem and never completely returns to the muon[2]. This results in the oscillations of $P_\mu^z(t)$ exhibiting relaxation.

Further insight is provided by investigating the mutual information between the fluorine system and the muon, $I(\mu : \mathrm{F}) = S_\mu + S_\mathrm{F} - S_{\mu\otimes\mathrm{F}}$, a quantity which quantifies the entanglement between both systems[3] [87]. This is plotted in Figure 4.3, again for the muon polarisation initially along the F–μ–F bond (z) and perpendicular to it (x). From this, one can see that initially for all cases $I(\mu : F) = 0$, corresponding to the fact that measuring the muon polarisation provides no information as to the state of the fluorine system as no polarisation exchange has happened yet. However, as time increases, the mutual information increases from 0, and, if the nnns are included, never returns. This is because some polarisation has been transferred from the muon to the surrounding nuclei, so making a measurement of the muon polarisation results in one gaining information as to the state of the fluoride environment.

An interesting feature of this system is that in general the total polarisation of the system is *n*ot conserved, which can be inferred from Noether's theorem [88]:

[2]This can be seen for the F–μ–F case, where there is an irrational ratio of frequencies ($\sqrt{3} : \frac{3-\sqrt{3}}{2} : \frac{3+\sqrt{3}}{2}$).

[3]Mutual information answers the question "How much do we learn about the F system by measuring μ?" This quantity is maximal when S_μ and S_F is maximal, as more information is gained by making the measurement of the muon polarisation.

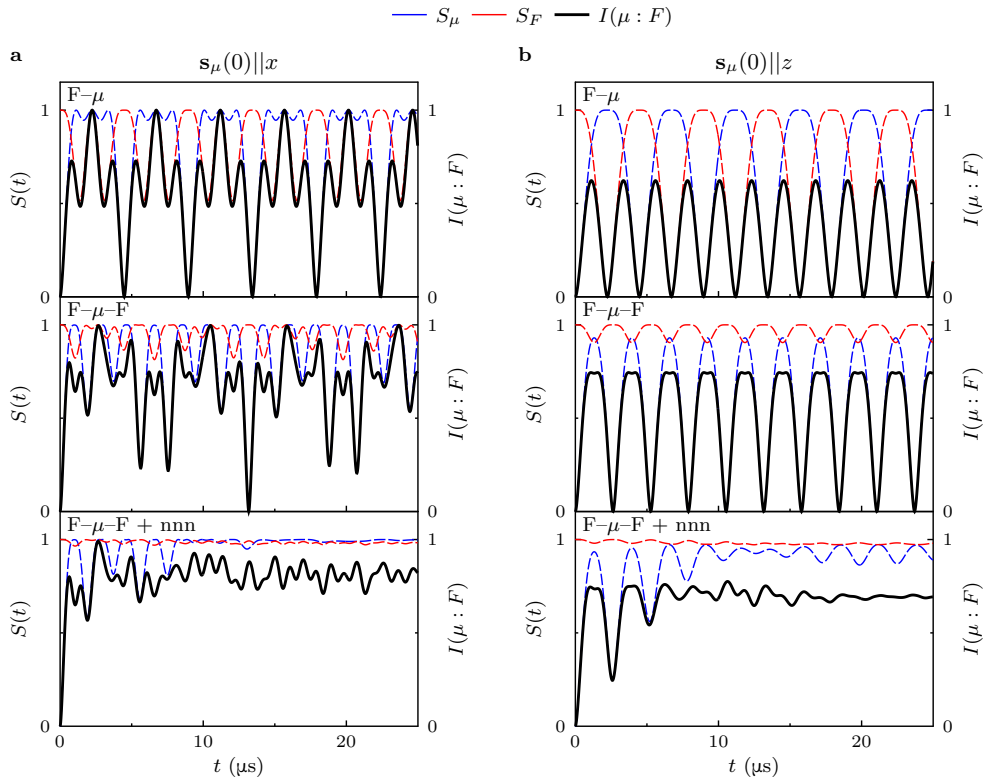


Figure 4.3: Mutual information in the F–μ system. **a**, The mutual information in the F–μ, F–μ–F and F–μ–F state with the next-nearest neighbour (nnn) couplings included, where the initial muon polarisation is perpendicular to the F–μ bond. Here, S_μ is the entropy of the muon, and S_F is the entropy of all the N fluorine nuclei included in the calculation. **b**, the same as **a** but with the initial muon polarisation parallel to the F–μ bond.

for the case of the muon initially polarised along the F–μ–F bond (z), the system has cylindrical symmetry along the bond and hence the total angular momentum along z will be conserved. However, if the muon is initially polarised perpendicular to this, there is no longer cylindrical symmetry (as the symmetry is broken by the muon polarisation creating a unique direction) and hence the total angular momentum will no longer be conserved[4] (in both cases, adding nnns breaks this conservation law as these remove the cylindrical symmetry).

It is important to note that even including nnn interactions only results in a

[4]This can be seen by rotating the operators in Equation (3.8) in the x–y plane for $\hat{\boldsymbol{r}} = \hat{\boldsymbol{z}}$ and $\hat{\boldsymbol{r}} = \hat{\boldsymbol{x}}$, and it turns out only the former case results in the Hamiltonian being invariant. Alternatively, one can also show this more simply (but perhaps less insightfully) by defining $s^z_{\mathrm{T}} = \sum_i s^z_i$, and using Heisenberg's equation of motion $\frac{\mathrm{d}s^z_{\mathrm{T}}}{\mathrm{d}t} = \frac{1}{i\hbar}[s^z_{\mathrm{T}}, \mathcal{H}]$ to show that only one of these cases is zero.

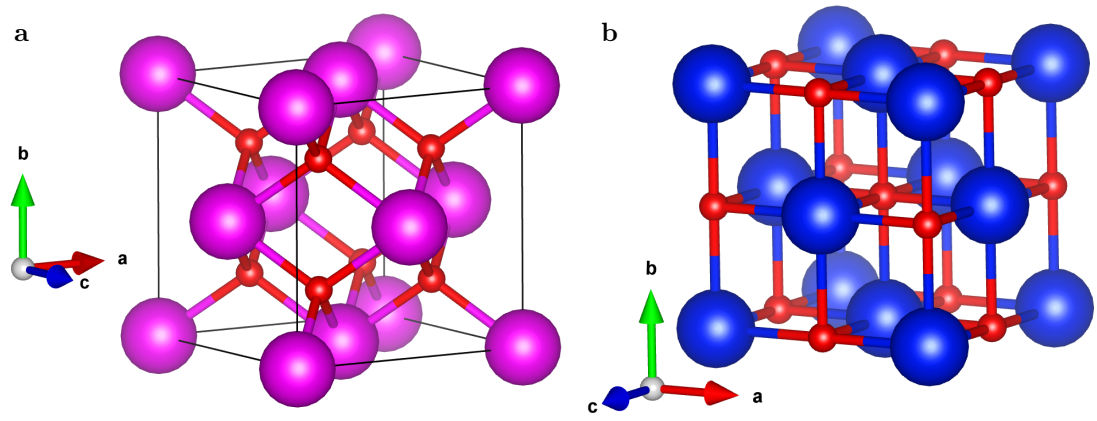


Figure 4.4: Crystal structure of CaF_2 and NaF. a depicts the positions of the calcium (magenta) and fluorine (red) atoms in CaF_2, and **b** depicts the positions of the sodium (blue) and fluorine atoms in NaF.

larger interacting cluster and does not yet account for the decoherence due to the entire crystal, which I will discuss in the next section.

4.3 CaF_2: a model system

To demonstrate how to account for system-environment interactions, CaF_2 was identified as a model system since the Ca nuclear spin can be neglected (the most abundant Ca isotopes have $I = 0$ and make up 99.86% of the nuclei, see Appendix C); thus only the fluorine nuclei contribute to the μSR spectrum. CaF_2 adopts the cubic fluorite structure (lattice parameter $a = 5.451$ Å) as depicted in Figure 4.4**a**, and the muon site was identified by density functional theory calculations (DFT+μ [60] using Quantum Espresso [89], a software package which allows one to perform density-functional theory calculations, using a plane wave basis to represent the electron wavefunctions). The muon site lies between two fluoride ions, each of which is pulled in towards the muon, resulting in a 14% reduction in the F–F separation distance. These calculations show that the effect of the muon on the positions of the more distant nuclei is negligible. An exact diagonalisation method was used to evaluate the time evolution of the density matrix and simulate $P_\mu^z(t)$ [90, 91], which was undertaken by calculating Equation (B.5) in Appendix B, but with more fluorine nuclei. An exact treatment has the virtue of accounting for all

interactions precisely, but can only be carried out with a small number of nearest neighbours (a Trotter-like method as discovered by Celio is also possible [91], but for the system considered here the improvement is marginal, as including all the inter-fluorine interactions in the Hamiltonian requires a large number of SWAP gates in the calculation of the time evolution operator [92, 93]). The dimension of the Hilbert space is $2\prod_{i=1}^{M}(2I_i+1)$, where the product is over the M nuclei included in the calculation (and the initial factor of two is due to the muon spin), and this dimension grows exponentially with M, making this method prohibitively computationally expensive when too many nuclei are included. Earlier attempts to include coupling beyond the nearest-neighbour fluorines using the method in Ref. [91] were carried out, but were limited by the computing power available at the time, see Refs. [68] and [94]. Hence, we restrict our diagonalisation method to include only nearest-neighbour and nnn fluorine nuclei, but scale the nnn interactions to account for all couplings in the infinite lattice. This can be done in a quantitative way by considering the second moment of the nuclear dipole field distribution, a quantity well known from the theory of broadening of NMR lines [95, 96]. The second moment σ_M^2 of this distribution at the muon site is given by

$$\sigma_M^2 = \frac{2}{3}(\frac{\mu_0}{4\pi})^2\hbar^2\gamma_\mu^2\sum_{j=1}^{M}\frac{\gamma_j^2 I_j(I_j+1)}{r_j^6}, \tag{4.1}$$

where r_j is the distance from the muon to the j^{th} nucleus with spin I_j and gyromagnetic ratio γ_j, $\gamma_\mu(=2\pi\times 135.5$ MHz $\text{T}^{-1})$ is the muon gyromagnetic ratio, and the sum converges as $M\to\infty$. ζ_{nnn} is then calculated such that

$$\sigma_\infty^2 = \sigma_{\text{nn}}^2 + \frac{2}{3}\left(\frac{\mu_0}{4\pi}\right)^2\hbar^2\gamma_\mu^2\sum_{j\in\text{nnn}}\frac{\gamma_j^2 I_j(I_j+1)}{(\zeta_{\text{nnn}}r_j)^6}, \tag{4.2}$$

where σ_{nn}^2 is due to nearest-neighbour couplings only and the sum is restricted to nnn. As the sum converges quickly, practically σ_∞^2 can be calculated by choosing M to be the nuclei closer to the muon than a cutoff radius r_{cutoff} (around 50 Å was sufficient), then considering the further contributions from the infinite lattice by turning the sum into an integral. This adds up the further contributions, using the average second moment from the unit cell (u.c.), and noting that the number

of nuclei at a distance between r and $r + \mathrm{d}r$ from the muon is $4\pi r^2 n \mathrm{d}r$, where n is the number density of nuclei. Hence

$$\sigma_\infty^2 = \frac{2}{3}\left(\frac{\mu_0}{4\pi}\right)^2 \hbar^2 \gamma_\mu^2 \left[\sum_{r_j < r_{\mathrm{cutoff}}} \frac{\gamma_j^2 I_j(I_j+1)}{r_j^6} + \int_{r_{\mathrm{cutoff}}}^{\infty} \frac{4\pi r^2}{r^6} n \sum_{j \in \mathrm{u.c.}} \frac{\gamma_j^2 I_j(I_j+1)}{N_{\mathrm{u.c.}}} \mathrm{d}r \right], \tag{4.3}$$

thus we adjusted the coupling to the nnn nuclei using the parameter ζ_{nnn} to mimic the effect of all more distant couplings. Because contributions to the second moment scale as $1/r_j^6$, ζ_{nnn} should be to be close to unity (but $\zeta_{\mathrm{nnn}} < 1$ because the more distant couplings make a positive contribution to σ_∞^2). The effect of ζ_{nnn} can be seen most clearly by looking at Figure 4.5, which shows that for around $0.8 < \zeta_{\mathrm{nnn}} < 1$, much of the features of the $\zeta_{\mathrm{nnn}} = 1$ case remain and the main effects on the peaks is an additional broadening, causing the observed relaxation of the muon polarisation. However, when ζ_{nnn} is too small, e.g. $\zeta_{\mathrm{nnn}} = 0.7$, spurious extra peaks are observed in the spectrum which are due to the muon becoming too strongly entangled with the nnns, leading to the assumption of the further nuclei behaving as classical magnetic moments being no longer valid.

For CaF_2, a direct calculation of Equation (4.2) results in $\zeta_{\mathrm{nnn}} = 0.943$, thus slightly enhancing the coupling with the nnn fluorine nuclei so that they are able to act as a proxy for all the coupling beyond the nnn fluorines to the rest of the lattice. The Hamiltonian can then be easily evaluated for this system of eleven particles (one muon, two nearest-neighbour fluorine nuclei and eight next-nearest-neighbour fluorine nuclei), and has dimension 2048×2048, whereas including the next shell of fluoride neighbours would become unfeasible for exact diagonalisation. Our DFT+μ calculations on CaF_2 show that the nnn fluoride ions do move towards the muon by a very small distance (approx 0.03 Å), and including this in our calculation of ζ_{nnn} leads to $\zeta_{\mathrm{nnn}} = 0.937$.

P. Biswas performed a μSR measurement on CaF_2 and these measured asymmetry data were fitted to the function $A(t) = A_{\mathrm{r}} P_\mu(r_{\mathrm{nn}}, \zeta_{\mathrm{nnn}}; t) + A_{\mathrm{bg}}$, where A_{r} accounts for muons which form diamagnetic (μ^+) states (see Section 2.1), A_{bg} accounts for muons stopping outside the sample, and $P_\mu(r_{\mathrm{nn}}, \zeta_{\mathrm{nnn}}; t)$ is the polarisation signal on

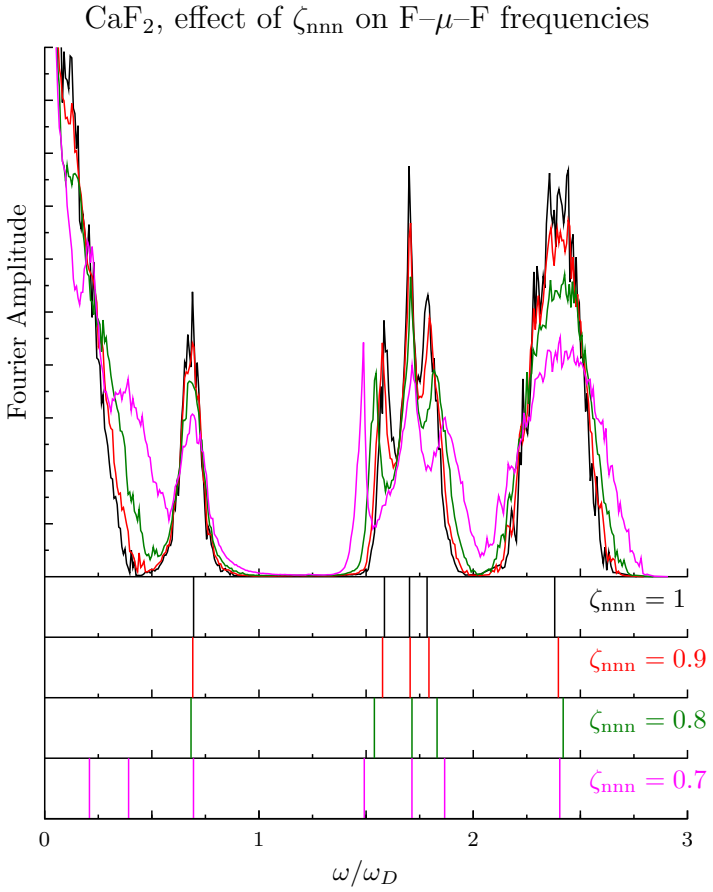


Figure 4.5: The effect of ζ_{nnn} on F–μ–F frequencies. The Fourier transform of the F–μ–F + nnn muon polarisation is shown for various ζ_{nnn}, demonstrating the effect of adjusting ζ_{nnn} on the muon precession frequencies. The bottom plot shows the positions of the major peaks as a guide to the eye.

which we are focusing (here, r_{nn} corresponds to the nearest-neighbour F–μ distance, and ζ_{nnn} is the relative adjustment of the nnn coupling, defined in Eq. (4.2)). The value of A_{r} is consistent with approximately 35% of muons implanting in diamagnetic states, suggesting the remainder are in paramagnetic muonium (Mu^0) states, in agreement with previous work [97]. The agreement of these simulations with the experimentally observed $A(t)$ can be seen in Figure 4.6**a**. If only the nearest-neighbour fluorine nuclei are considered (isolated F–μ–F; dashed line in Figure 4.6**a**) the fit is very poor, but the inclusion of nnn couplings results in an impressive agreement between theory and experiment (solid line in Figure 4.6**a**). Note that this fit does not need to include any phenomenological relaxation function of the sort used in previous studies [67, 69, 70, 74–76, 98]. Instead, the observed

relaxation of the oscillations results *entirely* from the nnn couplings. The fit uses only two fitting parameters, one of which is the distance between the muon and the two nearest-neighbour fluorine nuclei, which is found to be 1.172(1) Å (very close to the DFT prediction of 1.134 Å, and dramatically shorter than the $\frac{a}{4} = 1.362$ Å expected if there was no muon-induced distortion). The second fitting parameter is $\zeta_{\mathrm{nnn}} = 0.920(3)$, within 2% of the predicted value. These results demonstrate that, with suitable scaling, the eight nnn fluoride ions, which constitute a spin-subspace of dimensionality $2^8 = 256$, can provide an adequate representation of the full environment due to the entire crystal (Figure 4.6**b**), allowing a quantitative description of the decoherence for this problem.

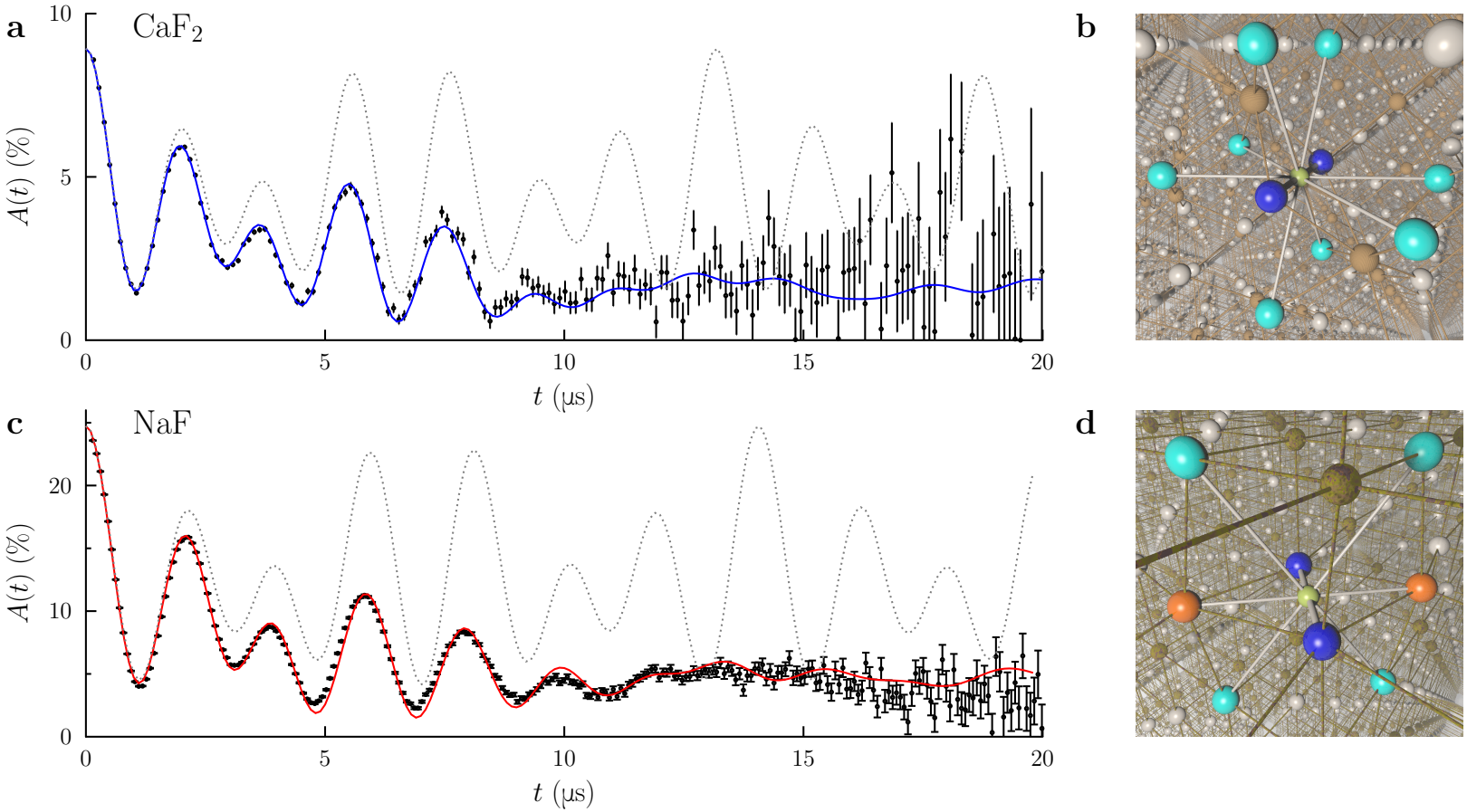


Figure 4.6: Muon data and fits for CaF_2 and NaF. a Muon decay asymmetry data $A(t)$ for polycrystalline CaF_2 (at 50 K), together with the simulated muon polarisation without (dotted line) and with (solid line) the effects of environmental decoherence. **b** The muon (green sphere) strongly coupled to two fluorine nuclei (dark blue spheres), and weakly coupled to next-nearest neighbour fluorine nuclei (cyan spheres), embedded inside the fluorite structure of CaF_2. **c** $A(t)$ for NaF (at 100 K), with simulations as in **a**. **d** The muon (green sphere) strongly coupled with the two nearest-neighbour fluorine nuclei (blue spheres, pulled close to the muon) and weakly coupled with the two nearest sodium nuclei (orange spheres, pushed away from the muon), and the next-nearest-neighbour fluorine nuclei (cyan spheres).

4.4 NaF: a model quadrupolar system

These methods for fitting μSR fluoride data can be extended to the more general case, in which the cation nuclear spin is non-negligible. NaF adopts the rocksalt structure[5] as depicted in Figure 4.4 and contains sodium nuclei which have spin $I = \frac{3}{2}$ (see Appendix C). In this case, the muon forms an F–μ–F state with the muon sitting at the centre of a square containing two fluorine ions and two sodium ions on its corners. The muon couples most strongly to its two nearest neighbour fluorine nuclei, then the next largest couplings arise from the two sodium nuclei; then the next largest couplings are due to four nnn fluorine nuclei. We used the four nnn fluorine nuclei (subspace dimension 16) as a proxy for all of the more distant fluorine and sodium couplings, and evaluated the muon polarisation function only for these nine spins (one muon, the two closest fluorines and sodiums, and four nnn fluorines, as shown in Figure 4.6**d**, giving a Hamiltonian with dimensionality 2048), and we also included the quadrupolar interaction of the Na nuclei in the electric field gradient of the muon, which is an additional term in the Hamiltonian of the form

$$\hat{\mathcal{H}}_{\mathrm{Q}} = \sum_{i \in \mathrm{Na}} \frac{eQ(1+\gamma)}{\hbar 2I(2I-1)} \sum_{\alpha\beta} V^i_{\alpha\beta} \hat{I}^i_\alpha \hat{I}^i_\beta, \tag{4.4}$$

where

$$\begin{aligned} V^i_{\alpha\beta} &= \frac{\partial^2 V(\boldsymbol{x}^i)}{\partial x_\alpha \partial x_\beta} \\ &= \sum_{j \neq i} \frac{q_j}{4\pi\epsilon_0} \left(\frac{3(x^i_\alpha - x^j_\alpha)(x^i_\beta - x^j_\beta) - \delta_{\alpha\beta}|\boldsymbol{x}^i - \boldsymbol{x}^j|^2}{|\boldsymbol{x}^i - \boldsymbol{x}^j|^5} \right), \end{aligned} \tag{4.5}$$

is the external electric field gradient (EFG) at the site of the ith quadrupolar (Na) nucleus (with spin operator $\boldsymbol{I}^i$), due to charges q_j, and the sum is performed over all atoms in the lattice. The tensor is traceless and so $V^i_{xx} + V^i_{yy} + V^i_{zz} = 0$. For Na, the quadrupole coupling factor $Q = 0.10 \times 10^{-28}$ m^2, and the anti-shielding factor γ is 4 [96] (this anti-shielding factor arises due to the electron orbitals around the Na interacting with the EFG, which amplifies the quadrupolar interaction [99–102]).

[5]The rocksalt structure is a cubic structure with alternating anions and cations. It is called this because it is the structure of table salt, NaCl.

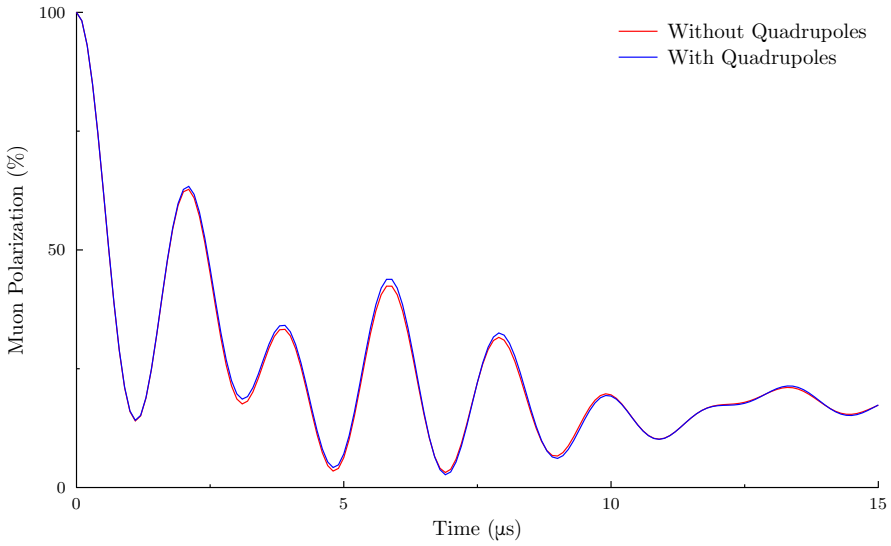


Figure 4.7: Effect of the quadrupolar interaction on NaF. The red line shows the evolution of the muon polarisation only considering dipole couplings, and the blue line also includes the small quadrupolar coupling on the Na ions.

In pure NaF there is no EFG at the Na site since all the contributions from the other ions cancel by symmetry, but the presence of the muon leads to three effects which result in a non-zero EFG at the two Na sites closest to the muon:

1. The presence of the muon itself leads to an EFG at each Na site resulting from the muon's charge of $+|e|$.

2. The displacement of each Na from its equilibrium position due to the implanted muon means that the EFG contributions from the other ions in the crystal no longer cancel.

3. A third, smaller effect, is due to the other muon-induced local distortions of the ions (principally the two fluorine anions adjacent to the muon and the other sodium cations).

The effect of including the quadrupolar interaction on the muon polarisation is small, as shown in Figure 4.7, however the effect gets more pronounced at longer times and can be essential when very high muon decay statistics are measured.

Therefore we[6] collected 720 million muon decay events for NaF so that we could carefully study the details of the precession signals. The fitting function used was $A(t) = A_{\mathrm{r}} P_{\mu}(r_{\mathrm{nn}}^{\mathrm{F}}, r_{\mathrm{nn}}^{\mathrm{Na}}, \zeta_{\mathrm{nnn}}; t) + A_{\mathrm{bg}}$, and the analysis again demonstrated that the nearest-neighbour fluorine anions are pulled towards the muon and the sodium cations are pushed out (so that $r_{\mathrm{nn}}^{\mathrm{F}} = 1.1980(3)$ Å and $r_{\mathrm{nn}}^{\mathrm{Na}} = 2.31(3)$ Å, rather than both being 1.637 Å without the muon-induced distortion, values which are in good agreement with DFT+μ calculations). The value of $r_{\mathrm{nn}}^{\mathrm{Na}}$ was used in evaluating the quadrupole interaction via the calculated electric field gradient from the muon. The scaling parameter was fitted to be $\zeta_{\mathrm{nnn}} = 0.86(1)$, very close to the calculated value $\zeta_{\mathrm{nnn}} = 0.88$ using Equation (4.2). The fit was again in excellent agreement with data (Figure 4.6**c**), and no phenomenological relaxation functions were required; all the parameters used in the fit are derived directly from the physics of the system.

4.5 Low-energy muons and fluoride states

Equation (4.2) shows that the nuclei beyond the nnn contribute to the relaxation of the muon asymmetry in a quantifiable way. A natural question one could therefore ask is to what extent can you manipulate such an effect by reducing the number of surrounding nuclei? One possible approach to this is to use low energy muons, for example using the LEM spectrometer at PSI [103]. This spectrometer allows one to select the energy of the muons incident upon the sample, by accelerating them with a potential set by the user, and then the stopping depth of the muons in the sample can be chosen by adding a solid N_2 layer to act as a buffer for the muons.

Figure 4.8 shows the results of simulations of such an experiment. The stopping profile was calculated for various thicknesses of the N_2 layer and various muon implantation energies, which results in a stopping profile which extends around 250 nm into the CaF_2 sample. Such a profile, however, will not produce a noticeable difference in the μSR asymmetry: Figure 4.8**b** shows the expected muon polarisation from muons stopped at the very surface, and in the bulk. The difference is very

[6]The experimental team consisted of myself, F. Pratt and S. Blundell. The data are available at doi:10.5286/ISIS.E.RB1920547.

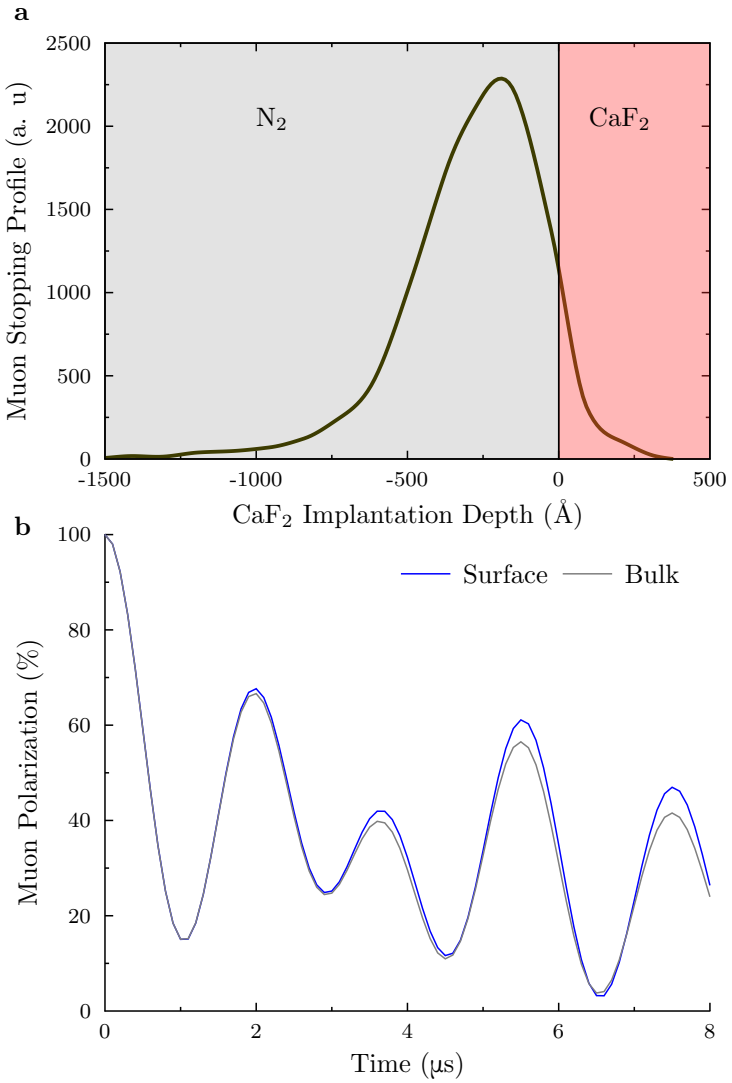


Figure 4.8: Exploring the surface of CaF_2 with low energy muons. **a** shows the stopping profile of the muons with energy 8 keV on a 150 nm N_2 layer. **b** shows the muon polarisation from muons stopped at the very surface, compared with those stopped in the bulk sample

slight (the surface value of ζ_{nnn} is within 1% of the bulk value at an implantation depth of only 2 lattice parameters (10.9 Å)), and the relatively large width of the stopping profile makes the effect experimentally very difficult to measure, especially with the low statistics available at PSI.

4.6 Conclusion

This chapter has shown how recasting the F–μ–F problem discussed in Section 3.3 in a quantum information framework can provide a wealth of additional insight into its physics. In particular, it is possible to have a much deeper understanding of the way in which the muon's quantum information dissipates into the other spins of the system, which is the cause of the relaxation observed in the data. In addition, this chapter has outlined a method of incorporating all the spins in an infinite lattice into the calculation of the muon polarisation in a quantitative way, which is in excellent agreement with the data. These findings will form the basis of the work in the proceeding chapters, which will demonstrate how these methods can be extended to a wide range of other systems.

This chapter is based on Phys. Rev. B **104** *L220409 (2021) (Ref. [104])*

5 Muon Sites in PbF_2 and YF_3: Decohering Environments and Frenkel Defects

Contents

5.1 Introduction 49
5.2 Frenkel defects 50
5.2.1 Theory 50
5.2.2 Frenkel defects in fluorides 52
5.3 DFT+$Mu^{\pm}$ 53
5.4 μSR experiments and results 57
5.4.1 PbF_2 results 57
5.4.2 YF_3 results 62
5.4.3 Comparison to previous approaches 64
5.5 Conclusion 64

5.1 Introduction

In the previous chapter I showed how by extending the Hilbert space of the F–μ–F problem to include the next-nearest neighbours, μSR data for simple cubic fluorides can be explained with an unprecedented level of detail, allowing one to infer the nature of the muon sites in a way which closely matches electronic structure calculations. A prevailing question, however, is what happens in fluorides with

a more complicated crystal structure? Can F–μ–F states be used to distinguish between multiple possible sites found with DFT+μ?

In this chapter, I extend the method used for CaF_2 and NaF previously and apply it to two other ionic fluorides: YF_3[1] and α-PbF_2. These were chosen as they have structural phases with a more complicated structure than the simple cubic phases considered previously, and thereby show that the method can be utilised in conjunction with DFT+μ to provide an insight into structural phase transitions and defect states, allowing one to gain a fuller understanding of the nature of the perturbation of the muon on the surrounding nuclei.

PbF_2 comes in both the α and β structural phases: the compound adopts the fluorite β phase at high temperature (the same structure as CaF_2), and at low temperature the α phase with space group *Pnma*. The structural phase transition occurs at around 600 K, but the β phase is reported to be more stable at room temperature [106]. YF_3 also adopts a structure with space group *Pnma*, and in both compounds the cation moments are negligible so only the fluorine nuclei contribute significantly to the μSR data (see Appendix C for the isotopes with non-zero nuclear moments).

5.2 Frenkel defects

5.2.1 Theory

Often theoretical models of materials assume a crystal structure which consists of a lattice and a motif; where simply replicating the motif across all space produces the structure of the crystal [107, 108]. However in reality the structure of a crystal is rarely – if ever – perfect, and is often instead filled with vacancies, interstitials, and the unintentional introduction of additional elements from the crystal growth process.

Anion Frenkel defects (AFDs) are defects which occur when anions in an ionic solid become displaced from their positions in the perfect crystal, leaving behind a

[1] Although YF_3 has been measured and analysed before [61], the crystal structure used for the analysis was incorrect (as discussed in Ref. [105]), and it was therefore not possible in that study to fit the data without including a phenomenological relaxation function.

vacancy and implanting themselves in a metastable site elsewhere[2]. The fraction of vacancies due to AFDs forming can be estimated through simple thermodynamical arguments. The Gibbs[3] free energy of a defective crystal, assuming that the free energy of a perfect crystal is G_0 and the creation of a vacancy/defect pair costs energy g_F (and including an additional term $-TS_\mathrm{config}$ due to the configurational entropy), is

$$G = G_0 + ng_\mathrm{F} - TS_\mathrm{config}, \tag{5.1}$$

where n is the number of Frenkel vacancy/defect pairs. At equilibrium,

$$\frac{\partial G}{\partial n} = 0, \tag{5.2}$$

so

$$g_\mathrm{F} - T\frac{\partial S_\mathrm{config}}{\partial n} = 0. \tag{5.3}$$

If there are N anions in the perfect lattice, N' possible defect locations and n defect/vacancy pairs, the configurational entropy S_config is

$$S_\mathrm{config} = k_\mathrm{B} \log\left(\frac{N!}{(N-n)!n!}\frac{N'!}{(N'-n)!n!}\right), \tag{5.4}$$

(this comes about because there are ${}^{N}\mathrm{C}_n$ ways of choosing n of the anions to become defective, and ${}^{N'}\mathrm{C}_n$ ways of choosing where these defective ions end up).

Using Stirling's law ($\log N! \approx N\log N - N$), assuming N, N' and n are all large, we get

$$\frac{\partial S_\mathrm{config}}{\partial n} = k_\mathrm{B} \log\left(\frac{N-n}{n}\frac{N'-n}{n}\right), \tag{5.5}$$

so Equation (5.3) becomes

$$g_\mathrm{F} - k_\mathrm{B}T \log\left(\frac{N-n}{n}\frac{N'-n}{n}\right) = 0. \tag{5.6}$$

Rearranging, defining the fraction of vacant anion sites as $f = n/N$, we get

$$g_\mathrm{F} - k_\mathrm{B}T \log\left(\frac{N}{N'f^2}\right) = 0, \tag{5.7}$$

[2]Some books explain this in terms of them occurring when the ionic radii of the anion and cation are vastly different, but as ionic radii are difficult to define and vary wildly depending on the surrounding ions, it is not a very helpful explanation.

[3]We are using the Gibbs free energy as both T and P are kept constant.

for small f. Hence,

$$f = \left(\frac{N}{N'}\right)^{\frac{1}{2}} \exp\left(-\frac{g_{\mathrm{F}}}{2k_{\mathrm{B}}T}\right), \tag{5.8}$$

so the defect formation energy g_{F} quantifies the number of vacancies that are present in the crystal.

5.2.2 Frenkel defects in fluorides

In many fluorides, an additional relaxation component is also present in the μSR asymmetry, which was first reported by Noakes et al. [69] and discussed in Section 3.3. The origin of this component has up until now been unidentified, but in PbF_2 there is evidence this is due to diamagnetic Mu^- states located in anion vacancies, the origin of which are due to anion Frenkel defects (AFDs). There have been a number of examples in the past of muons becoming trapped in vacancies in metallic systems, where the signature of the trapped muon is a change in the relaxation rate of the muon asymmetry. Fe [109] and quenched Al are classic examples of this effect, where for the latter case, the extra relaxation remains down to temperatures as low as 10 K [110]. These cases however relate to μ^+, and requires significant muon diffusion in order for it to reach the vacancies [111]. On the other hand, in ionic fluorides, although μ^+ diffusion tends to require fairly high temperatures of about 200 K [68] due to the strength of the F–μ–F bonds, this is not necessarily the case for Mu^-.

As discussed in the previous section, the likelihood of AFDs forming is quantified by the defect formation energy, g_{F}, which is usually of the order of a few eV, meaning that a large abundance of these defects often occur in equilibrium at temperatures of the order of hundreds of kelvin, but some can be "frozen in" to the material and therefore still be present at low temperatures. I utilised DFT to estimate the anion Frenkel defect formation energy, with an approach similar to that undertaken before in pyrochlores [112]: a supercell composed of $2 \times 2 \times 2$ conventional unit cells was created, and multiple calculations were run, trialling multiple different fluorine vacancy and defect positions, and the cell was relaxed until the forces on all the ions fell below a convergence threshold of 51 meV Å^{-1}. The initial defect

Compound	g_F (eV) (calculated)	g_F (eV) (experimental)
YF_3	3.70	-
CaF_2	2.17	2.2–3.1 [113, 114]
α-PbF_2	1.55	1.12 [115]
β-PbF_2	1.05	0.9–1.1 [113, 115]

Table 5.1: Anion Frenkel defect energies g_F calculated by DFT (also showing the experimental values where available), using the method described in the text.

positions were chosen to be in sites of high symmetry (Wyckoff sites 4a and 4b for the *Pnma* structures, and 4b for the fluorite), and the final relaxed positions were found to be very close to the initial sites. The location of the defects which had the lowest energy are shown in Figure 5.1. I found that if the anion is placed in an interstitial site sufficiently far away from the the vacancy, the atoms would not relax to their original positions. The final relaxed energies of the supercells containing the defect were compared to those without defects to obtain an estimate for g_F, and these energies are tabulated in Table 5.1, alongside the experimental values where available, which agree well with these calculations. From this, one can conclude that both structural phases of PbF_2 are much more likely to contain Frenkel defects than YF_3 and CaF_2, a result which is supported by the absence of evidence of such defect states in those compounds in the μSR experiments.

5.3 DFT+$Mu^{\pm}$

The stopping sites of the muon were calculated using DFT+μ for YF_3, and both the α and β phases of PbF_2, following the methods in Section 3.2.2. To this extent, ultrasoft pseudopotentials were used to model the electronic structure of the ions, and the muon was modelled with a hydrogen pseudopotential. The cell was given a total charge of $+|e|$ to model the positive charge of the bare muon. For α-PbF_2, the DFT analysis predicts three possible low-energy sites. The two with the lowest energies are between crystallographically inequivalent fluoride anions (one site is only 16 meV higher in energy than the other) and the site with the third lowest energy (185 meV above the lowest energy site) places the muon between two fluoride

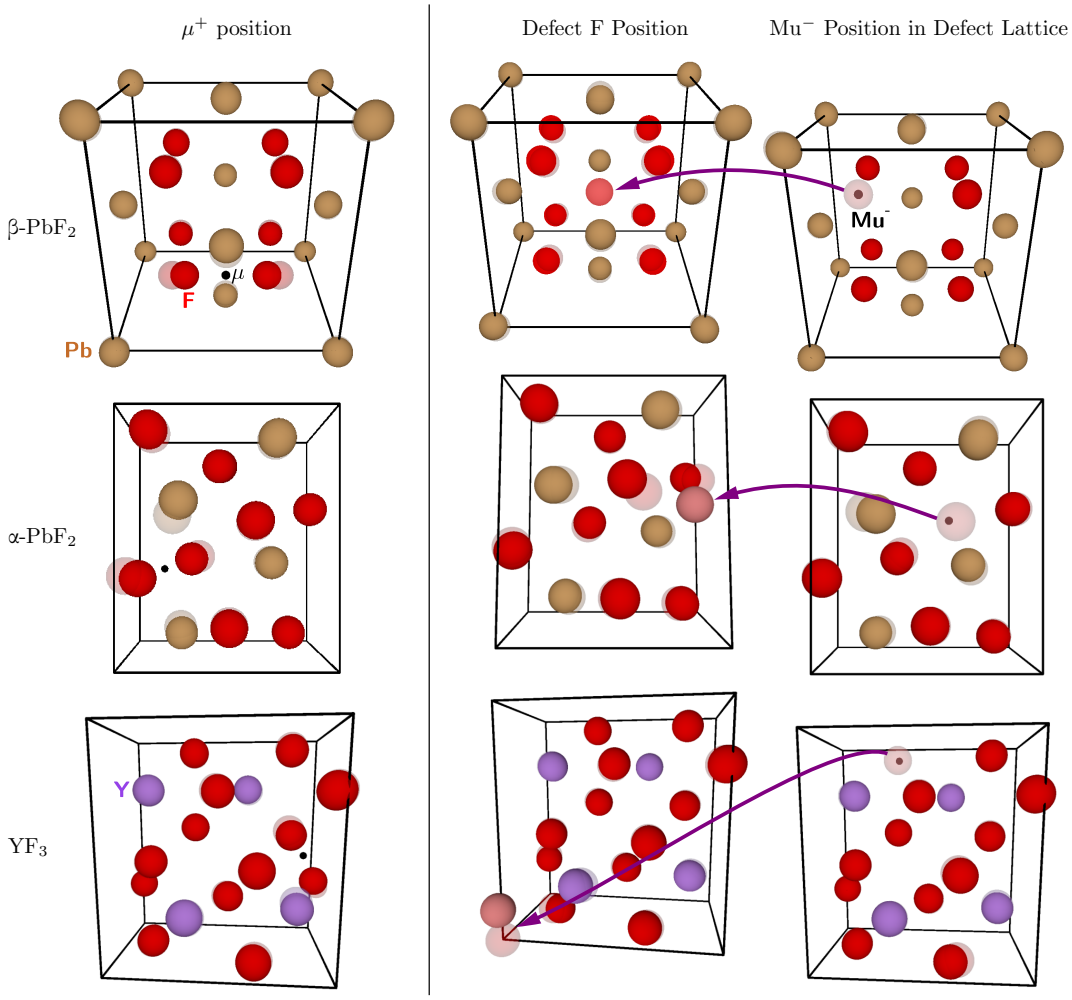


Figure 5.1: Muon sites in PbF_2 and YF_3, calculated with DFT. The left-hand side shows the muon site calculated with the DFT+μ method, as described in the text. In all cases, the muon (black sphere) sits in between two fluoride ions (red spheres), and the transparent (solid) spheres show the locations of the surrounding ions before (after) the perturbation of the implanted muon. The centre column shows the position of the defect fluorine in the perfect lattice, and the final (initial) relaxed positions of the surrounding ions are displayed as solid (transparent) spheres. Finally, the right-hand column shows the site of the Mu^- (black sphere) in the vacancy created by such a defect, and the effect of this on the surrounding ions.

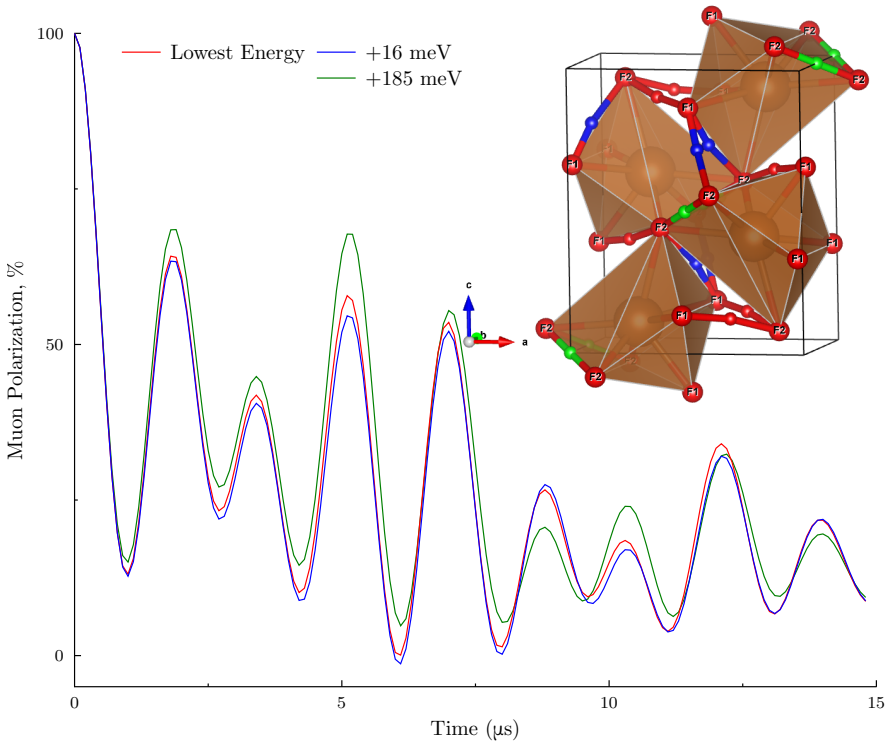


Figure 5.2: Polarisation of the three muon sites in α-PbF_2, predicted by DFT+μ to have the lowest total energy. The inset shows the muon sites with the three lowest energies as red, blue and green spheres (ignoring muon-induced distortions), and the time dependence of muon polarisation expected from these three sites is shown in the main frame.

ions which occupy the same Wyckoff position[4]. The predicted muon polarisation from all these sites is plotted in Figure 5.2, where it can be seen that there is only a small difference between the two sites with the lowest energy, but the site with energy above this shows a substantially different time-dependent polarisation, and can therefore be ruled out (note that the polarisation plotted in this figure is before any small adjustment of the μ–F distances which occur when these polarisations are fitted to the data). For β-PbF_2, the muon site was found to be identical to the site found in CaF_2, and has been calculated in previous work [60].

For YF_3, the DFT+μ calculation resulted in three sites which had the lowest energy: two between crystallographically inequivalent fluorines, and one between two fluorines in equivalent sites, as shown in the inset in Figure 5.3. The muon

[4]All the other sites had energy much greater than this, so were discounted from further analysis.

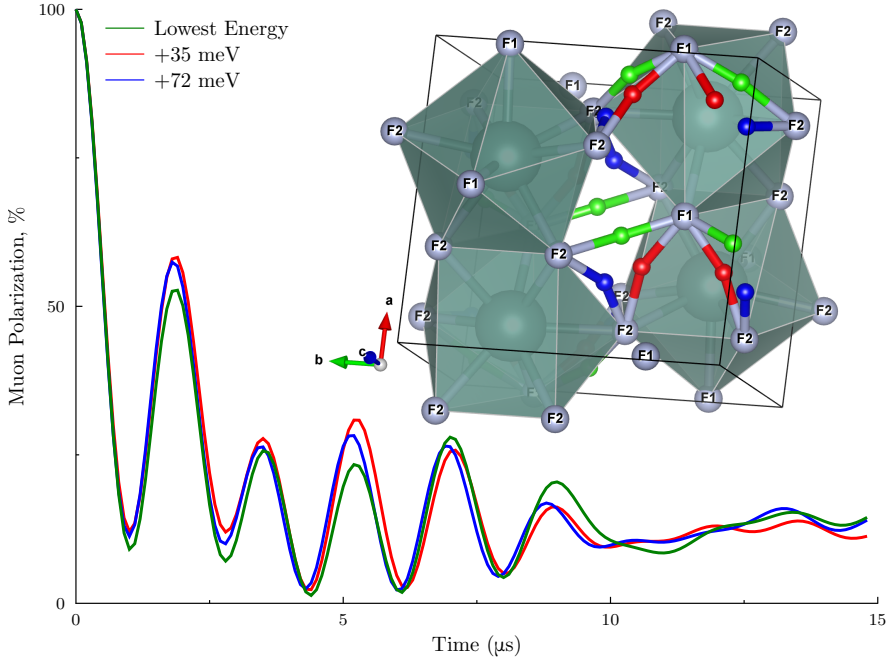


Figure 5.3: Polarisation of the YF_3 muon sites, predicted by DFT+μ to have the lowest total energy. The inset shows the muon sites with the lowest energy (green), 35 meV above this (red), and 72 meV above the lowest energy site (blue) (the distortions induced by the muon are not shown). The graph in the main frame corresponds to the expected muon polarisation from these three sites.

polarisation for these three states are also plotted, and the site which was determined to best fit the data was the site with the lowest overall energy.

The stopping sites of the Mu^- ions in the vacancies caused by the AFDs were also calculated and are shown in Figure 5.1. These were calculated in a similar way to DFT+μ, but instead a charge of $-|e|$ was added to the supercell to represent the two electrons bound to the muon. As the fluorine vacancy has a very strong positive charge, this was the location chosen to be the starting point for the Mu^-. After relaxing the atomic positions, the muon sites were found to be very close to the positions of the anion vacancies, as expected.

In order to test the hypothesis of Mu^- stopping in AFDs, I also used DFT to calculate the effect of another possible Mu^- state which is in the pristine (defect-free) PbF_2 lattice. In this case, the Mu^- finds a 4c site, with position $(0.25, 0.75, 0.274)$, and a nearest-neighbour Mu^-–F distance of 2.29 Å, compared to the AFD state

having a nearest-neighbour Mu^-–F distance of 2.78 Å. This difference nearly doubles the leading order term of the Hamiltonian as the muon precession frequencies vary as $r_{\mu F}^{-3}$, meaning the correct state should be clear from the data.

5.4 μSR experiments and results

Samples of α-PbF_2 and YF_3 were wrapped in 25 µm Ag foil and placed into the MuSR spectrometer at ISIS. The PbF_2 experiment was done at 10 K, in the year 2005 by the Oxford muon group (Prof. S. Blundell, Prof. T. Lancaster, Dr F. Pratt and Dr P. Baker). The YF_3 experiment was also undertaken by the Oxford group, in 2020 by myself, Prof S. Blundell and Dr. F. Pratt. Prior to the μSR experiments, both samples were placed into an X-Ray diffractometer by Dr. D. Prabhakaran to confirm both samples did not contain significant levels of impurities, and that the samples were not hydrated (as ^{1}H has a nuclear moment of $2.793\mu_N$, this would affect the μSR spectrum considerably).

5.4.1 PbF_2 results

The PbF_2 data were fitted with the function

$$\begin{aligned} A(t) = A_r[&(1-c_{AFD})P_\mu(r_{nn1}, r_{nn2}, r_{nnn1}, r_{nnn2}, \zeta_4; t) \\ &+ c_{AFD}P_{Mu^-}(t)] \\ &+ A_{bg}e^{-(\lambda t)^2} \end{aligned} \tag{5.9}$$

assuming the α phase and also, to test the robustness of the procedure, assuming the β phase. The first term $P_\mu(..)$ describes the muon polarisation calculated from the dipolar Hamiltonian (Equation (3.8)), using the muon site calculated with DFT+μ, where r_{nn1} and r_{nn2} represent the distance from the muon to the two nearest neighbour fluorines, and r_{nnn1} and r_{nnn2} is the distance to the next-nearest neighbour fluorines. The second term $P_{Mu^-}(t)$ is the polarisation of the negatively charged Muonium ion in an AFD site, and the final term $e^{-(\lambda t)^2}$ represents a slow relaxation of the muon polarisation due to the weak nuclear moments in the Ag sample holder. As Pb has a very weak nuclear moment, only the nearest ten

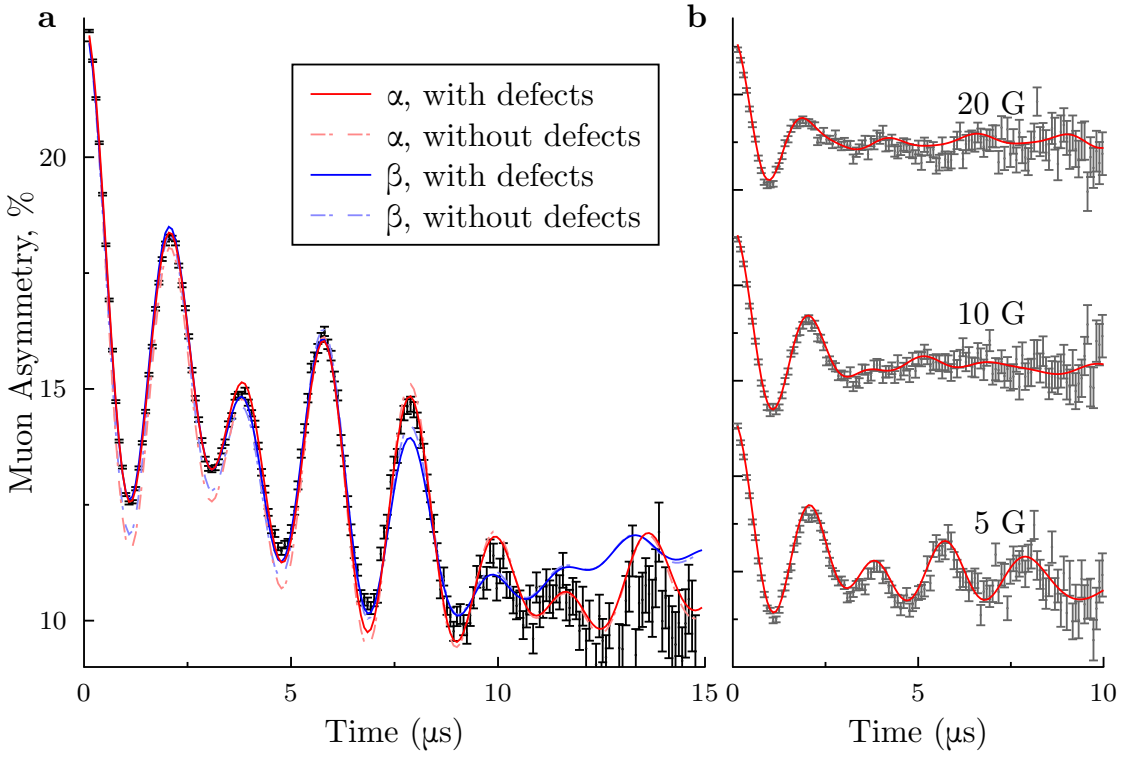


Figure 5.4: α-PbF_2 results. **a** shows the zero-field μSR data obtained for our sample of PbF_2, and the solid (dashed) lines corresponding to fits of the data with (without) taking into account the Mu^- entering into a defect state. **b** shows the data obtained with a longitudinal field applied, plotted with the muon polarisation as described in the text.

fluorine nuclei were included in the calculation of the muon polarisation and so the Hamiltonian was described by a matrix of size 2048 × 2048. The initial fractional positions of the nuclei included in the calculation are listed in Table 5.2.

The results of the fits to both the α and β phases are shown in Fig. 5.4**a**, along with simulations for which c_{AFD} was fixed to zero (i.e. ignoring AFDs). From this, one can see that the best fit is obtained by including the presence of AFDs and with PbF_2 adopting the α phase. The superiority of the α-phase fit is especially apparent for the data at longer times (> 8 μs), where the polarisation function strongly deviates from the data for the β phase. Further evidence supporting the validity of the model applying to the α phase of the compound is obtained by considering the second moment rescaling factor ζ, as introduced in Chapter 4. As the muon is in a site where the adjacent ions do not form neat shells of nearest- and next-nearest neighbours, ζ_k is used instead of ζ_{nnn}, which now defines the

α-PbF_2				β-PbF_2			
Spin	Fractional Position			Spin	Frac. Pos.		
μ	0.1879	$\frac{1}{2}$	0.3906	μ	$\frac{1}{2}$	$\frac{1}{4}$	$\frac{3}{4}$
F_{nn1}	0.0172	$\frac{3}{4}$	0.3520	F_{nn1}	$\frac{1}{4}$	$\frac{1}{4}$	$\frac{3}{4}$
F_{nn2}	0.3586	$\frac{1}{4}$	0.4291	F_{nn2}	$\frac{3}{4}$	$\frac{1}{4}$	$\frac{3}{4}$
F_{nnn1}	-0.0172	$\frac{1}{4}$	0.6480	F_{nnn1}	$\frac{1}{4}$	$\frac{3}{4}$	$\frac{3}{4}$
F_{nnn2}	0.5172	$\frac{3}{4}$	0.1470	F_{nnn2}	$\frac{3}{4}$	$\frac{3}{4}$	$\frac{3}{4}$
F_5	0.0172	$\frac{1}{4}$	0.3520	F_{nnn3}	$\frac{1}{4}$	$\frac{1}{4}$	$\frac{5}{4}$
F_6	0.3585	$\frac{5}{4}$	0.4291	F_{nnn4}	$\frac{3}{4}$	$\frac{1}{4}$	$\frac{5}{4}$
F_7	0.6415	$\frac{3}{4}$	0.5709	F_{nnn5}	$\frac{1}{4}$	$-\frac{1}{4}$	$\frac{3}{4}$
F_8	-0.1415	$\frac{1}{4}$	0.0709	F_{nnn6}	$\frac{3}{4}$	$-\frac{1}{4}$	$\frac{3}{4}$
F_9	0.1415	$\frac{3}{4}$	-0.0709	F_{nnn7}	$\frac{1}{4}$	$\frac{1}{4}$	$\frac{1}{4}$
F_{10}	-0.0172	$\frac{5}{4}$	0.6480	F_{nnn8}	$\frac{3}{4}$	$\frac{1}{4}$	$\frac{1}{4}$

Table 5.2: The original positions of the nuclei in both phases of PbF_2, before muon implantation.

rescaling of the k^{th} furthest atoms from the muon included in the calculation of the Hamiltonian (i.e. ζ_4 in this case rescales F_7 to F_{10} in Table 5.4). The fit for the α phase obtained a value of $\zeta_4 = 0.834(5)$, very close to the calculated value of 0.838. However, for the β phase, the fitted value of $\zeta_{\text{nnn}} = 0.804(4)$, strongly deviating from the calculated value of 0.896. The structural distortions obtained from this fit, and the comparison to the values obtained with DFT+μ, are in Table 5.3. The table also shows the parameters for a fit assuming the muon site calculated by DFT which had an energy of 16 meV above the lowest energy site, which produces a very similar muon polarisation (as can be seen in Figure 5.2). Although inconclusive, the fit assuming the lowest energy site gives the parameters most consistent with DFT, so this is the assumed site[5]. The fit was also attempted considering a Mu^- state in a pristine lattice (instead of the AFD state), also using the DFT results mentioned previously, which can be seen in Figure 5.5. The slower relaxation found for the Mu^- state in the AFD matches well with the slow background relaxation observed in the data, providing strong evidence for the presence of AFDs in this sample.

[5]In practice, more muon statistics are required to accurately determine the next-nearest neighbour perturbations and beyond, which are essential to conclusively determine the site of the muon.

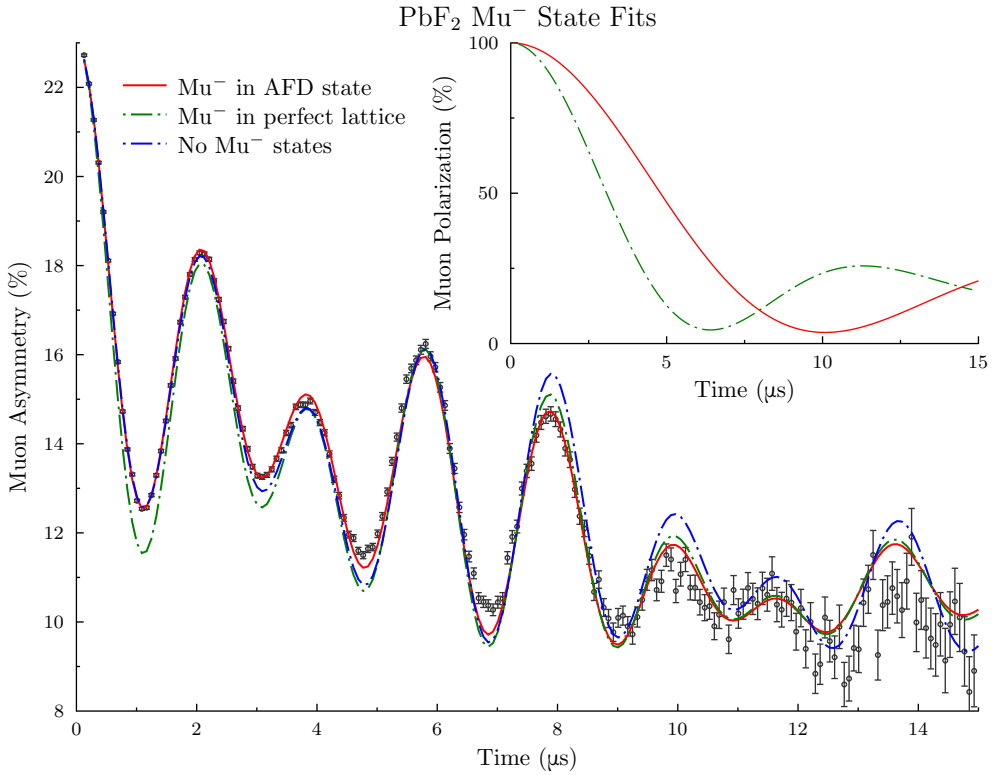


Figure 5.5: PbF_2 Mu^- state fits. The main plot shows the fit of the muon asymmetry from the model including a Mu^- state in crystals both with an AFD and without an AFD (the "perfect lattice"), and without including any Mu^- states at all. Inset: the muon polarisation exclusively from the two Mu^- states, i.e. without the μ^+ component.

Our results demonstrate that the details of the oscillatory signal are able to correctly distinguish between the two related crystallographic phases of PbF_2 and also determine the origin of the diamagnetic muonium signal. Note that the sensitivity of μSR data to these local differences is only revealed clearly in the late-time data (obtained well after $\approx 5\tau_\mu$ where, because of the muon decay, the data rate is more than two orders of magnitude lower than that obtained immediately after implantation). This result highlights the necessity for obtaining high-statistics μSR data so that these small late-time features in the data can be carefully resolved.

The best fit to the zero-field data was obtained assuming that 9.2(2)% of the diamagnetic fraction of the signal in α-PbF_2 was due to AFD states. In order to further quantify the effect of these weak diamagnetic states, a series of small longitudinal fields were applied to the sample. Applying such fields adds an

	Parameter	Experimental	DFT+μ	Difference
Lowest Energy	r_{nn1} (Å)	1.1419(4)	1.0967	+0.0452
	r_{nn2} (Å)	1.2601(7)	1.2057	+0.0544
	r_{nnn1} (Å)	2.68(3)	2.89	−0.21
	r_{nnn2} (Å)	3.01(7)	3.27	−0.26
	ζ_4	0.834(5)	0.838	−0.004
+16 meV	r_{nn1} (Å)	1.1410(5)	1.0965	+0.0445
	r_{nn2} (Å)	1.2580(9)	1.2090	+0.0490
	r_{nnn1} (Å)	2.54(3)	2.71	−0.17
	r_{nnn2} (Å)	3.54(1)	2.94	+0.6
	ζ_4	0.851(7)	0.835	+0.016

Table 5.3: Muon-induced structural distortions in PbF_2, comparing the values obtained with the fit to experimental data with the values obtained using DFT+μ.

additional Zeeman term to the Hamiltonian,

$$\mathcal{H} = \mathcal{H}_{\mathrm{dip}} + \sum_i \boldsymbol{\mu}_i \cdot \boldsymbol{B}, \tag{5.10}$$

where $\mathcal{H}_{\mathrm{dip}}$ is the magnetic dipole-dipole Hamiltonian[6] in Equation (3.8) which, for AFD Mu^- states, tends to be much larger than the dipole interactions, and hence $P_{\mathrm{Mu^-}}(t) \approx 1$. These results, along with plots of the polarisation function for α-PbF_2, using parameters obtained from the aforementioned fit and including the longitudinal field, are shown in Figure 5.4**b**. One can see that the model continues to describe our data very well, and the field indeed removes much of the effect of the defect states on the polarisation (which would not happen to the same extent for Mu^- in a pristine crystal, as the dipole interactions are stronger). Distinguishing between Mu^- and μ^+ states, however, is notoriously difficult, as there is no intrinsic spectroscopic difference between the two [116]. Previous studies [117, 118] have found Mu^- states forming at temperatures of around 200 K and above; however, there is some experimental evidence of a Mu^- state forming in H-doped perovskites in temperatures as low as 15 K [119]. This state was discovered by observing the

[6] As $\boldsymbol{B}$ is applied by the instrument, one cannot calculate the angular average of the muon polarisation by considering three perpendicular directions à la Equation (2.26), as $\mathcal{H} \mapsto \mathcal{H}(\theta, \phi)$. Instead, one needs to numerically evaluate the integral for multiple orientations of $\boldsymbol{B}$ in Equation (2.21).

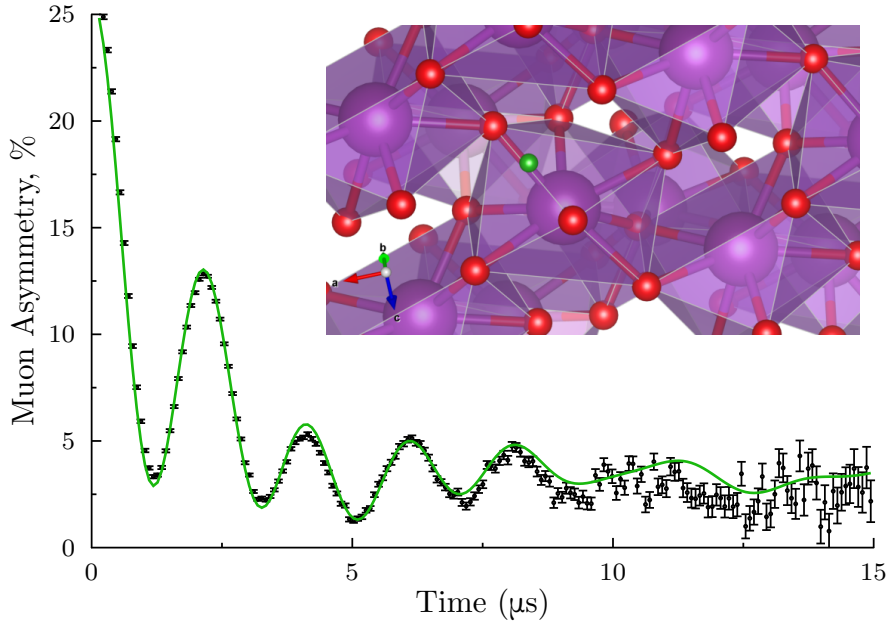


Figure 5.6: YF_3 results. The results of our μSR experiment, with the fitted muon polarisation using the muon site obtained by DFT. This site is displayed on the YF_3 crystal structure in the inset, with the atom positions unperturbed for simplicity.

Mu^-–H dipole entanglement, extracting the muon–H bond length and finding it to be too large to be due to a μ–H state [119], a somewhat analogous situation to the case of α-PbF_2 considered here.

5.4.2 YF_3 results

As our data for YF_3 did not show any slow relaxing background, and the DFT results show that AFDs are less likely to form than in PbF_2, it was not necessary to include the effect of AFDs in our fits of the data. Therefore the YF_3 data was fit to a simpler function, given by

$$A(t) = A_r P_\mu(r_{nn1}, r_{nn2}, r_{nnn1}, r_{nnn2}, \zeta_6; t) + A_{bg}, \tag{5.11}$$

where all symbols have the same meaning as before. As with PbF_2, the ten nearest fluorine nuclei were included in the calculation (Y has only one natural isotope, ^{89}Y, with a negligible moment of $0.137\mu_N$), leading again to matrices of size 2048×2048. The fractional positions of the nuclei involved in the calculation ignoring muon perturbations are listed in Table 5.4, using the muon site which was predicted by

Spin	Fractional Position		
μ	0.5635	0.9233	0.3378
F_{nn1}	0.4733	0.7500	0.4090
F_{nn2}	0.6652	1.0643	0.1245
F_{nnn1}	0.8348	0.9357	0.6245
F_{nnn2}	0.3348	0.9357	-0.1245
F_5	0.5227	1.2500	0.5910
F_6	0.1652	1.0643	0.3755
F_7	0.3348	0.9357	-0.1245
F_8	0.9773	0.7500	0.0910
F_9	0.8348	0.9357	-0.3755
F_{10}	0.6652	0.4357	0.1245

Table 5.4: Original positions of the nuclei in YF_3, ignoring muon perturbations.

Parameter	Experimental	DFT+μ	Difference
r_{nn1} (Å)	1.173(1)	1.10	+0.073
r_{nn2} (Å)	1.278(2)	1.22	+0.058
r_{nnn1} (Å)	2.24(3)	2.15	+0.09
r_{nnn2} (Å)	2.40(1)	2.49	−0.09
ζ_6	0.849(5)	0.907	−0.058

Table 5.5: Muon-induced structural distortions in YF_3, comparing the values obtained with the fit to experimental data with the values obtained using DFT+μ.

DFT to have the lowest energy (using both the LDA and PBE functionals). The fit using this model is depicted by the green line in Figure 5.6. The values obtained from the fit, and their DFT counterparts, are tabulated in Table 5.5, where it can be seen that the nearest- and next-nearest- neighbour perturbations of the fluorines due to the muon are in excellent agreement.

Note that, for the measured muon-induced distortions of YF_3 (and to a lesser extent, PbF_2), the discrepancy between the DFT values and the fitted values increases with the muon-fluorine distance, and that DFT slightly underestimates the bond lengths for nuclei close to the muon, and slightly overestimates these for those nuclei further away. While the PBE functionals tend to slightly underestimate bond lengths, the effect further from the muon may be due to the size of the supercell.

5.4.3 Comparison to previous approaches

As mentioned in Chapter 3.3, the previous approach to fitting F–μ–F states is to multiply the linear F–μ–F function by a stretched exponential decay. Applying such a method to this data results in the fits in Figure 5.7. This clearly shows the very significant improvement applying these methods have on the fits. Although χ^2 per degree of freedom (d.o.f.) is not a particularly useful metric for high rate μSR data[7], this method gives values which are significantly better: for PbF_2, the fit using all nuclei gives a χ^2 per d.o.f. of 3.99, but the stretched exponential fit gives 25.58. For YF_3, the all nuclei fit gives 16.84, but the stretched exponential fit gives 48.23.

5.5 Conclusion

This chapter has shown how the analysis techniques described in the previous chapter can be extended to materials with a much more complicated structure than simple cubic, and applying such techniques to μSR data on these complex fluorides allows one to obtain a wealth of useful information about the muon stopping site and the environment of the muon. This information was previously completely unobtainable when phenomenological relaxation functions were used to analyse the data. I have also shown how the data at long times are particularly useful for understanding the nature of the muon site. Additionally, this chapter has shown that it is possible to measure anion Frenkel defects using μSR in a model system, an important result which can be extended to the analysis of magnetic systems, where the effects of defects on the electronic structure could be important.

[7]This is primarily because the χ^2 cost function divides the square of the deviations of the data from the model by the error, which is estimated only by considering the decay statistics. In reality, the data at small times have an additional uncertainty due to deadtime, which is difficult to model for high rate data.

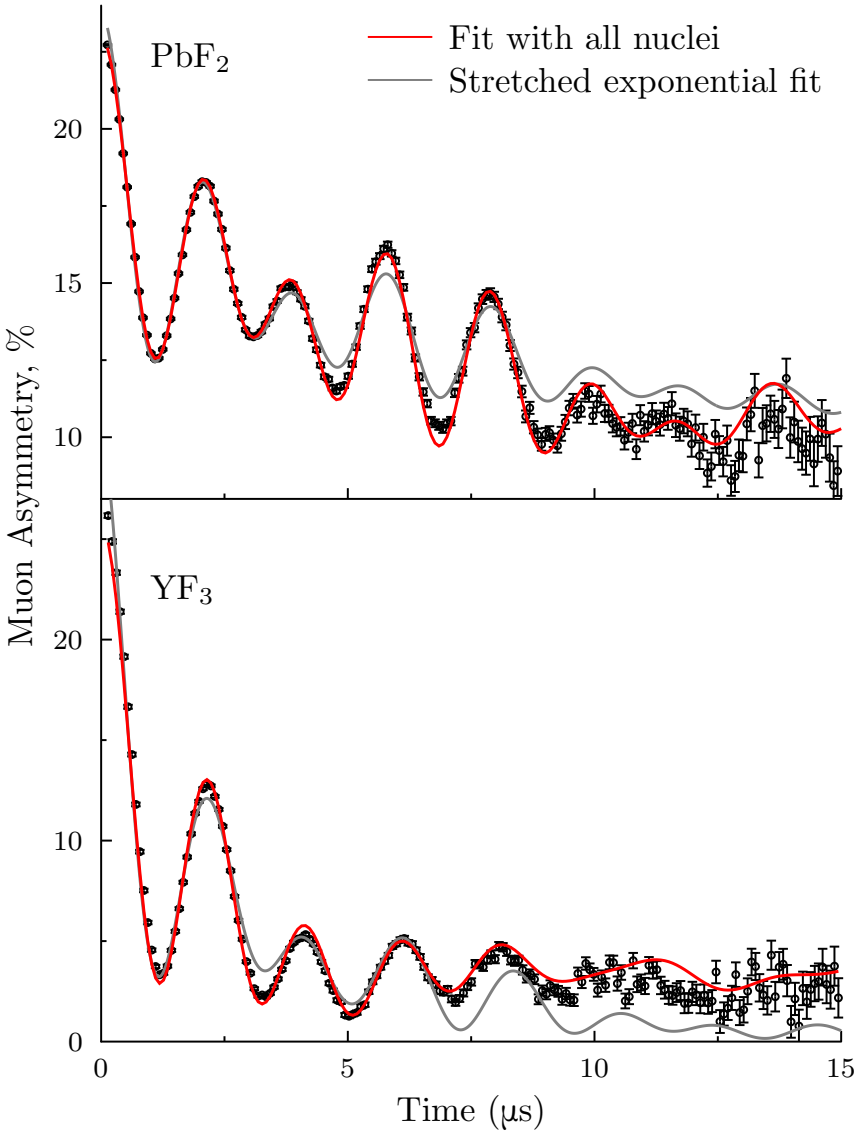


Figure 5.7: Comparison of fitting techniques for PbF_2 and YF_3. The graphs show fits to the data for PbF_2 (top graph) and YF_3 (bottom) with an F–μ–F function multiplied by a stretched exponential (grey), and the fits considering all the nuclei in the crystal (red).

6

KPF_6 and KBF_4: Identifying Muon Sites "by eye"

Contents

6.1 Introduction 67
6.2 Experimental details 69
6.3 KPF_6 70
6.3.1 Muon site determination 72
6.3.2 Data analysis 76
6.4 KBF_4 79
6.4.1 Muon site determination 80
6.4.2 Data analysis 86
6.5 Conclusion 88

6.1 Introduction

One of the principal uses of μSR is to measure magnetic materials, however, as mentioned in Chapter 3, the magnetic field the muon observes depends strongly on the muon stopping site, and the challenges of calculating this can prohibit a full quantitative analysis of the data. Although DFT+μ has been very successful in locating muon stopping sites in many cases, the fact that much of the rich physics of the most exciting quantum materials arises due to their d and f electrons

means that performing such calculations can take a very long time and is therefore unfeasible, even with the pseudoisation of the core electrons[1]. Therefore, it is helpful to see whether, in some materials, the muon stopping site can be determined by observing key features of the data, and using these to narrow down the muon stopping site, sometimes without having to use DFT+μ at all – or in other words, identifying the stopping site "by eye".

From the preceding two chapters and indeed the literature mentioned in Section 3.3, it can be seen that there is a pattern emerging for muons in fluorides: a muon has an overwhelming tendency to form an F–μ–F state, by implanting itself between two fluorides and pulling them closer in to itself. In Chapter 5, I showed that in compounds where there are many fluorines occupying a range of Wyckoff sites, there often appears to be one particular site which dominates the μSR spectrum. The muon seems to be excellent at locating the site with the lowest energy and is much less likely to settle in a site with energy greater than this. This insight will be useful for studying these more complicated compounds, as it is possible that they too have one muon stopping site which dominates the data.

This chapter will detail the analysis of two compounds: KPF_6 and KBF_4. These compounds contain the hexafluorophosphate ion ($[PF_6]^-$) and the tetrafluoroborate ion ($[BF_4]^-$), both of which are often found in molecular magnets [120–124]. By studying them in these compounds where the cation has a very limited effect on the μSR spectrum (the isotopes of K are listed in Appendix C, where it can be seen that all have a very small nuclear moment), one should be able to use the information gained from the analysis of these F–μ–F states to gain insight into the muon site in the somewhat more exciting compounds.

[1]By "pseudoisation", I mean using pseudopotential generation methods to create an effective potential for the outermost electrons which takes into account the nucleus and the innermost electrons closest to the core, meaning the core electrons do not need to be explicitly accounted for in the DFT calculations [59].

6.2 Experimental details

We[2] obtained polycrystalline samples of KPF_6 and KBF_4, and wrapped them in 25 µm Ag foil. A relatively large amount of sample was used (3.023 g and 1.828 g for KPF_6 and KBF_4 respectively), as the principal aim of the experiment was to maximise the long-time statistics so that details of the muon site and environment could be determined.

We placed the KBF_4 sample into the MuSR spectrometer at ISIS [39], and collected around 800 million muon decay statistics at a temperature of 10 K. These data are plotted in Figure 6.1**a**, where it can be seen that they give a very distinctive μSR spectrum, in particular due to the unusual peak at around $t = 10$ µs, which, as 10 µs is approximately $5\tau_\mu$, would only be visible when a very large number of decay statistics are measured.

KPF_6 data were also initially taken with the MuSR spectrometer, with the slits set to 100 mm (which resulted in approximately 2300 muon decay events measured per synchrotron pulse). However, this led to a significant deadtime effect, strongly distorting the low-time data as shown in Figure 6.1**c**. Even trying to correct for the deadtime using Equation (2.4) still resulted in unacceptable distortions to the data. Therefore, additional data were taken with the EMU spectrometer at ISIS[3] [125], which are shown in Figure 6.1**b**, and is the dataset used for this analysis. This dataset contained 1.45 billion events at a temperature of 10 K, again significantly higher decay statistics than what is usually measured in a typical μSR experiment. Data were also taken at higher temperatures and with a small 5 G longitudinal field, but at lower statistics.

The samples were later analysed with X-ray diffraction by D. Prabhakaran to check their purity. Both samples were found to have various impurities (over 10%), but it was not possible to determine the exact composition of the impurities[4].

[2]The experimental team consisted of myself, Franz Lang, Peter Baker, Francis Pratt and Stephen Blundell

[3]This EMU data were taken by Peter Baker and Stephen Cottrell.

[4]The X-ray diffractometer has been out of order for many months, and therefore it was not possible to get better data to analyse the impurities of the compounds in more detail. This however does not significantly affect the rest of this analysis.

Preliminary analysis suggests the KBF_4 sample contains a significant amount of KN_3 and KNO_3, but this does not take into account all of the scattered peaks measured so this remains uncertain. As KBF_4 is soluble in water, it is likely that there is also some hydration in the KBF_4 sample, which will affect the μSR spectrum as H has a large nuclear moment (see Appendix C). Preliminary analysis of the KPF_6 X-ray diffraction data suggests this sample was much purer than KBF_4, but also contained unidentified peaks likely due to impurities. Despite these impurities, the X-ray diffraction data show that the majority component of the both samples was the compound of interest, and as the samples showed very clear F–μ–F oscillations in the muon data it is still possible to use this data to determine the muon sites.

6.3 KPF_6

KPF_6 consists of octahedral $[PF_6]^-$ ions intercalated with K^+ ions. The crystal structure of KPF_6 has four phases [126, 127]:

- At higher temperatures (around room temperature and above), the compound adopts a face-centred cubic (fcc) structure with space group $Fm\bar{3}m$ (often referred to as phase I).
- For wet[5] KPF_6, the compound adopts a trigonal structure with space group $R\bar{3}$. This is also the high pressure phase [128] (often referred to as phase IV).
- For dry KPF_6, when cooled below room temperature, phase I transforms into a monoclinic phase with space group $A2/n$ (phase II), and then upon further cooling transforms into another monoclinic phase, with space group $C2/n$ (phase III).

For this study, the compound was assumed to be in the trigonal phase IV, which is depicted in Figure 6.2. This has K in position $(0.5, 0.5, 0.5)$, P at $(0, 0, 0)$ and F at $(0.7559, 0.7753, 0.0781)$ [127]. The positively charged muon, then, can be assumed to be in between two fluorines which are initially relatively close together (so that

[5]By 'wet', I mean KPF_6 which has not been thermally cycled to dry it out, as used for our experiments.

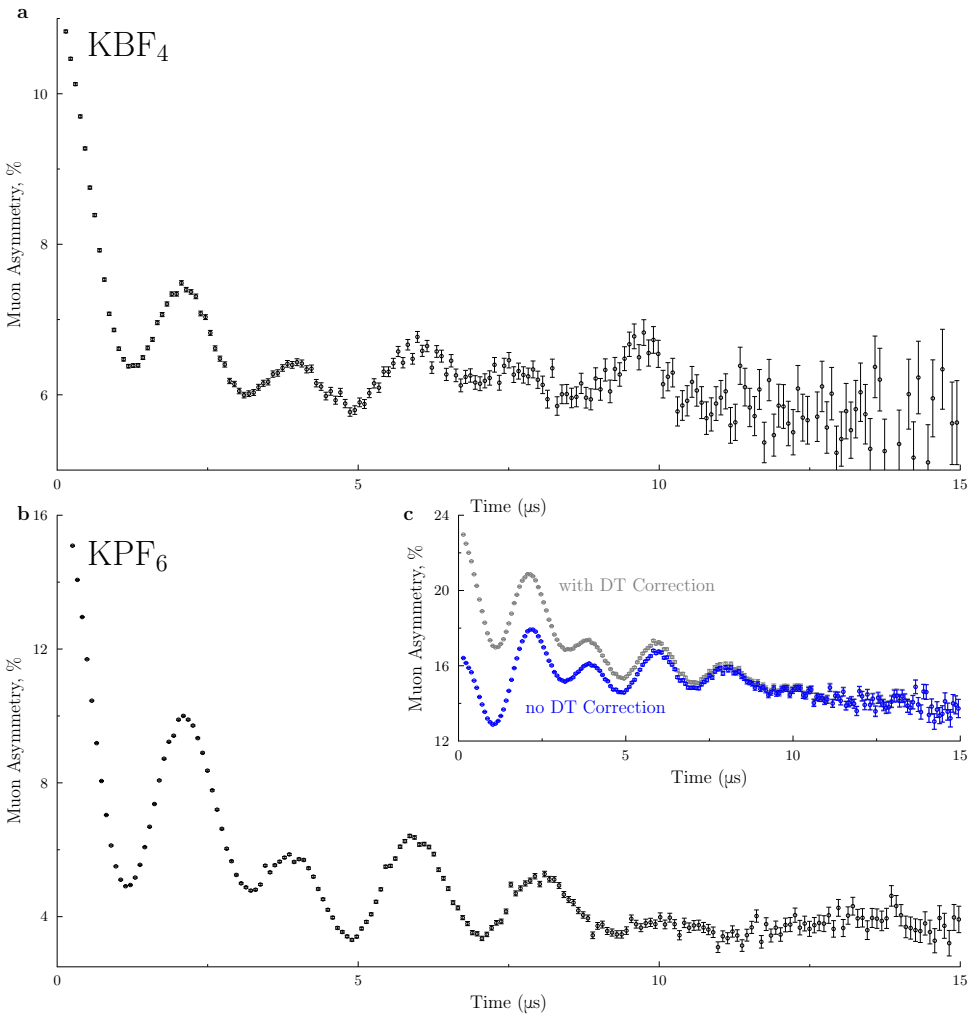


Figure 6.1: KBF_4 and KPF_6 muon data. **a** shows the data obtained at 10 K for KBF_4 with the MUSR spectrometer, and **b** shows the data for KPF_6 taken at 10 K with the EMU spectrometer. **c** shows the data for the latter sample taken with the MUSR spectrometer, with the slits set to 100 mm, but one can see that the deadtime (DT) correction is significant, and even with this correction there is a clear slowly relaxing background which is not present in the EMU data.

the Coulomb forces of the muon at the fluoride ions in their original positions are strong enough to sufficiently displace them) to form an F–μ–F state. There are therefore two categories of states the muon can form in this compound: "intra-octahedra" states, where the F–μ–F bond is formed between two fluorines in the same $[PF_6]^-$ octahedron, and "inter-octahedra" states, where the muon bonds to two fluorines on different $[PF_6]^-$ octahedra.

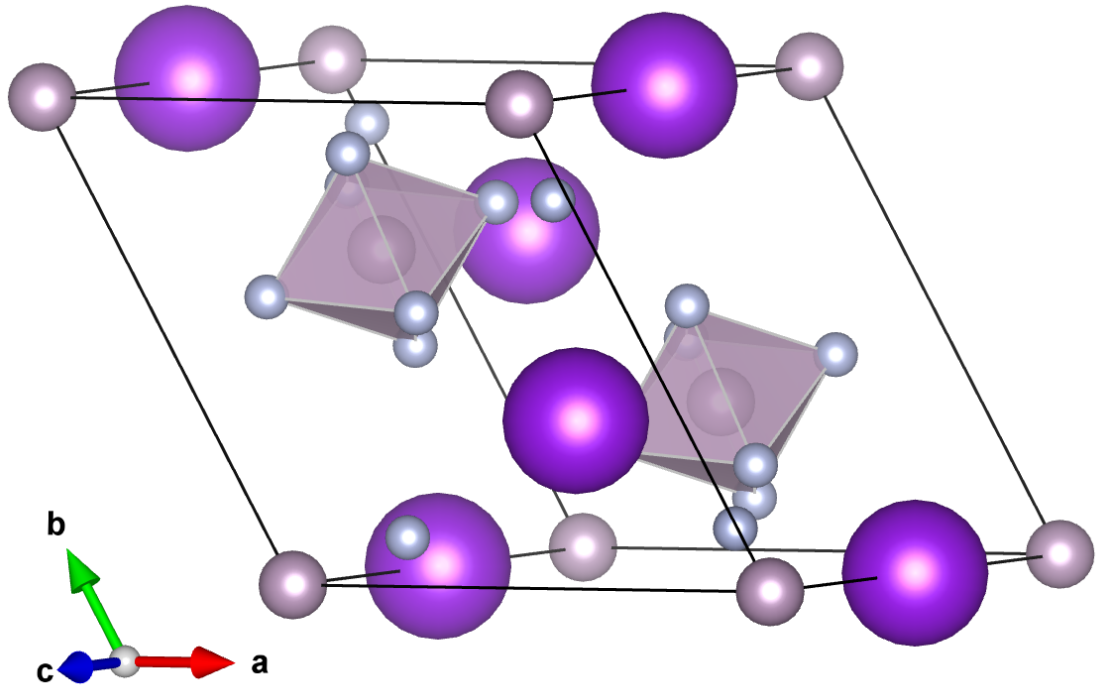


Figure 6.2: Crystal structure of the low-temperature 'wet' phase (IV) of KPF_6. The $[PF_6]^-$ octahedra consist of eight fluorines (grey) which occupy the same Wyckoff position, with a P in the centre (dark pink). These ions are intercalated with K^+ (purple).

6.3.1 Muon site determination

I calculated the muon polarisation for muons in various sites using the dipole-dipole Hamiltonian (Equation (3.8)), cutting off the Hilbert space when the matrices were of size 2048×2048. I chose the nuclei to be included in the calculation by calculating the size of the interaction between the muon and each of the nuclei surrounding the muon, $\frac{\mu}{r^3}$ [where μ is the nuclear moment and r is the distance between the muon and the nucleus], selecting the nuclei with the ten largest values of this figure of merit[6]. Figure 6.3 shows the muon polarisation one would expect from muons in various states. In this figure, the muon-induced distortions are assumed to only be felt by the nearest-neighbour fluorines, and are assumed to be

[6]This figure of merit is deduced directly from the dipole-dipole Hamiltonian; it is no longer sufficient to select the nuclei to be included by thinking in terms of nearest-neighbours as both P and F nuclei should be considered, which have different nuclear moments.

in a radial direction[7]. The nearest-neighbour F–μ distance was set to be 1.20 Å for every muon site, which is a rough estimate of the expected distance based on the F–μ–F states previously measured.

[7]These assumptions also mean that the F–μ–F bond angle is different for all the sites, but by comparing the two sites closest to the centre of the quadrilateral one can see that the that the overall environment of the muon has the greatest effect, as these two have a very similar muon polarisation but different F–μ–F bond angles.

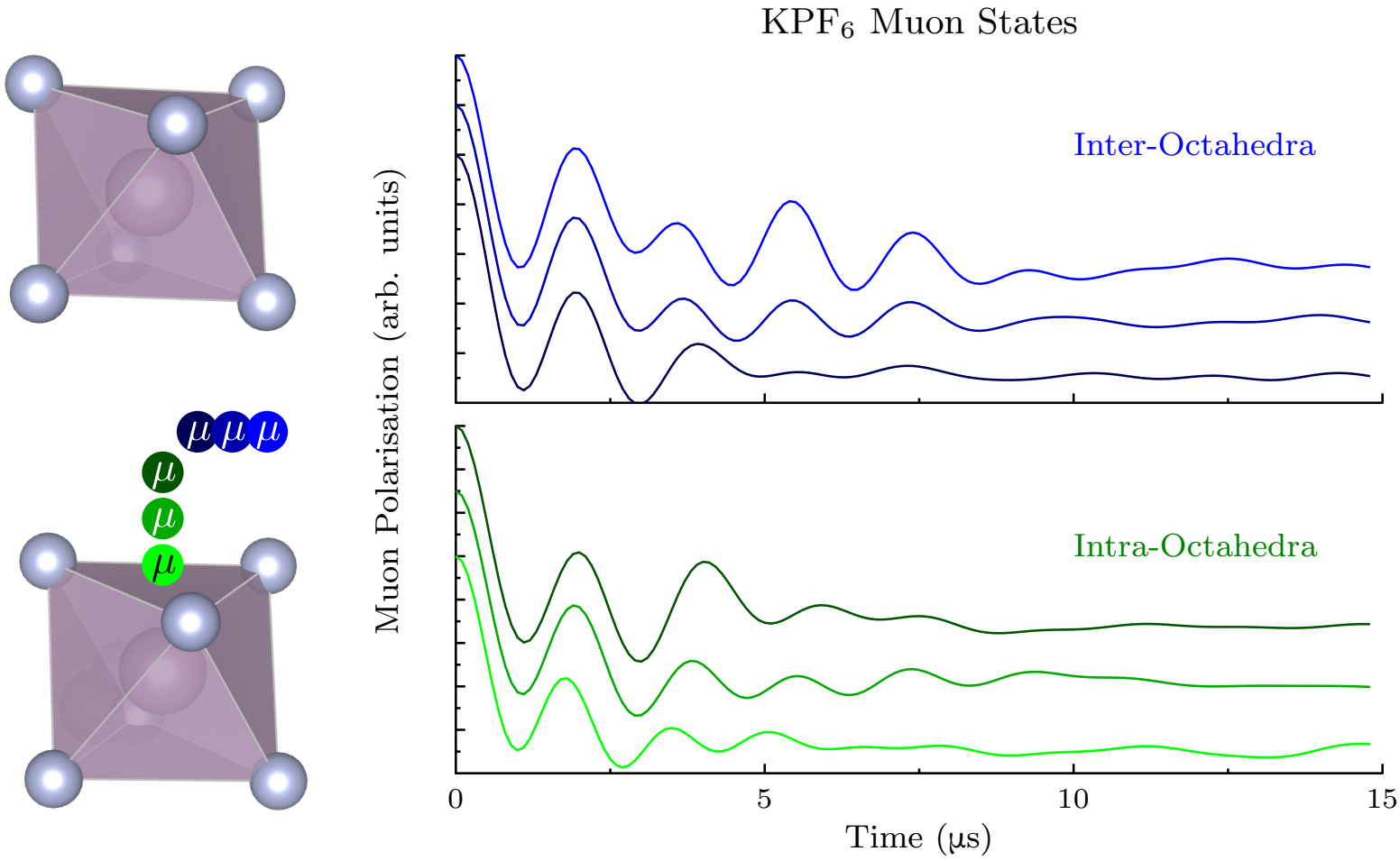


Figure 6.3: Muon states in KPF_6. The expected muon polarisation was calculated for the muons in the positions as shown on the diagram in the left side of the figure, with the colour of the muons matching the corresponding muon polarisation on the right hand side. The octahedra shown are the two shown in the conventional unit cell depicted in Figure 6.2, looking in the $-\boldsymbol{b}$ direction.

From this figure, it is clear that a change in muon site has a significant effect on the μSR data: each of the states produces a muon polarisation which is visually distinct, even though they are *all* F–μ–F states. These different muon sites would certainly not be distinguishable to any significant extent if the approach of modelling the relaxation by a stretched exponential function was used, as the main difference between these sites is the nature of the muon's decohering environment of surrounding nuclear spins. By comparing the data in Figure 6.1**b** to the states in Figure 6.3, it is clear that the muon state which most closely matches the data is the light blue inter-octahedra state[8]. This is likely because the P atom in the centre of the $[PF_6]^-$ ion has a slight positive charge, which repels the muon and ensures only inter-octahedra muon sites are realised.

In order to confirm this site, and to predict the lattice distortions, I also performed DFT+μ calculations[9] on KPF_6. As the rough location of the muon stopping site was determined previously, only one DFT relaxation calculation was required, as it was not necessary to place the muon in lots of random locations in the crystal structure. A supercell was constructed from $2 \times 2 \times 2$ conventional unit cells, and the muon was placed in an inter-octahedral position similar to that determined from the muon polarisation, and, as usual, the cell was given a charge of $+|e|$ to represent the charge state of the muon. The DFT+μ calculation predicts that the muon strongly distorts its nearest-neighbour fluorines, but the distortions of the further ions are to a lesser (but not negligible) extent. The DFT+μ result also predicted a slightly off-centre site: the distance between the muon and the two nearest fluorine atoms (r_{nn1} and r_{nn2}) was 1.07 Å and 1.25 Å respectively.

[8] You can qualitatively see the distinctive features of the predicted polarisation are similar to the data: the first two minima of the polarisation are at roughly the same height, and then all the subsequent minima are lower but also at similar heights to each other

[9] Trying to just fit the muon site starting from the lightest blue site in Figure 6.3 (as determined qualitatively) would not be a particularly good approach, as there is likely to be many possible local minima for the χ^2, and the impurities in the sample may cause a playoff between the fitting parameters.

6.3.2 Data analysis

With the DFT+μ results in mind, I initially fitted the μSR data to the function

$$A(t) = A_{\mathrm{rel}} P_\mu(r_{\mathrm{nn1}}, r_{\mathrm{nn2}}, r_{\mathrm{disp}}; t) + A_{\mathrm{imp}} e^{-\lambda t} + A_{\mathrm{bg}}, \tag{6.1}$$

where the first term represents the muons in the F–μ–F state in KPF_6, and r_{nn1} and r_{nn2} are the distances between the muon and the two nearest neighbour fluorines, r_{disp} is the displacement of the muon from the site determined by DFT+μ in the direction perpendicular to the line joining the two nearest-neighbours (i.e. increasing this moves the muon from the light blue state in Figure 6.3 to the darker blue), a parameter which in effect also adjusts the F–μ–F bond angle. Owing to the particularly high statistics of the dataset, particularly at 10 K, I used a larger Hilbert space to fit the data, with the matrices being of dimension 4096×4096, and the eight furthest nuclei from the muon were rescaled by a factor ζ_8, calculated from the DFT+μ results using Equation (4.2) and was *not* used as a fitting parameter[10]. The second term in the fitting function ($A_{\mathrm{imp}} e^{-\lambda t}$) models muons stopping in the various impurities in the sample, with the small nuclear moments causing a slow relaxation. The final term (A_{bg}) was included to model the small Ag nuclear moments in the sample holder, a term which is small because the KPF_6 sample covered the vast majority of the beam spot size. The value of these amplitudes are $A_{\mathrm{rel}} = 11.76(3)\%$, $A_{\mathrm{imp}} = 1.223(4)\%$ and $A_{\mathrm{bg}} = 1.87(1)\%$, and were fixed in every fit[11]. While fitting the data, I found that the parameters r_{nn1} and r_{nn2} were always the same, despite the DFT results suggesting otherwise[12]. Hence for all subsequent fits both parameters were set to the same value, r_{nn}. The fits are shown in Figure 6.4, which depicts the impressive agreement between the data and the model, and the results of the fitting parameters r_{nn} and r_{disp} for the temperatures

[10] The value of this varies with the parameter r_{disp}, as a change of muon site results in a change of ζ_8.

[11] From this, it is *not* possible to determine the relative amount of impurities in the sample, as the probability of the muon stopping in each of the compounds affects these quantities in a non-trivial way.

[12] This is not unexpected, as a muon sitting exactly in between two crystallographically equivalent fluorines should electrostatically attract both equally, and the force holding these fluorines to the $[PF_6]^-$ tetrahedra should also be the same for both.

T (K)	Statistics (MEv)	χ^2 per d.o.f.	r_{nn} (Å)	r_{disp} (Å)
10	1453	8.20	1.2053(4)	0.0513(28)
20	182	1.94	1.2045(5)	0.0772(40)
30	182	2.20	1.2063(5)	0.0888(35)
40	182	5.67	1.2089(6)	0.1186(19)

Table 6.1: KPF_6 fitting results. Only the parameters relating to the muon site as described in the text are shown. The χ^2 per degree of freedom tabulated here is calculated by considering the data where $t > 2$µs.

measured are in Table 6.1. This table also shows the χ^2 per degree of freedom for the fits, which takes into account data for $t > 2$ µs only, as this part of the data are much less affected by deadtime effects. In addition to the zero field dataset, a small longitudinal field was applied to the sample at 10 K, to remove the effects of the small nuclear moments in the impurities. Plotting the fitting function with $\lambda = 0$ and calculating $P_\mu(t)$ with the parameters obtained from the ZF fit results in excellent agreement with the data, and is also shown in Figure 6.4.

The fitting results in Table 6.1 show that the nearest-neighbour μ–F distance increases slightly with temperature. The origin of this is unclear, not least because the random error for each of these values is close to the deviation of the values between the temperatures. Nevertheless, thermal expansion might be a suitable explanation for this: the coefficient of thermal expansion for $[PF_6]^-$-containing compounds tends to be of the order of 10^{-5} K^{-1} [129], consistent with the order of magnitude of the changes in r_{nn}, but with only four temperature points it is not possible to conclusively determine this as the cause. The variation of r_{disp} with temperature is too large to be due to thermal expansion effects alone. A close inspection of Figure 6.3 suggests that increasing r_{disp} has the effect of increasing the relaxation, which would also happen if the muon is slowly diffusing at higher temperatures. Therefore, the increase of this parameter with temperature may be due to the incompleteness of the model. Some studies of diffusion in F–μ–F states (Refs. [68, 70, 74]) have modelled muon diffusion using the strong collision model [72, 73], but this would not take into account the fact the muon will have passed some of its polarisation onto the next-nearest-neighbour fluorines before diffusing to a new

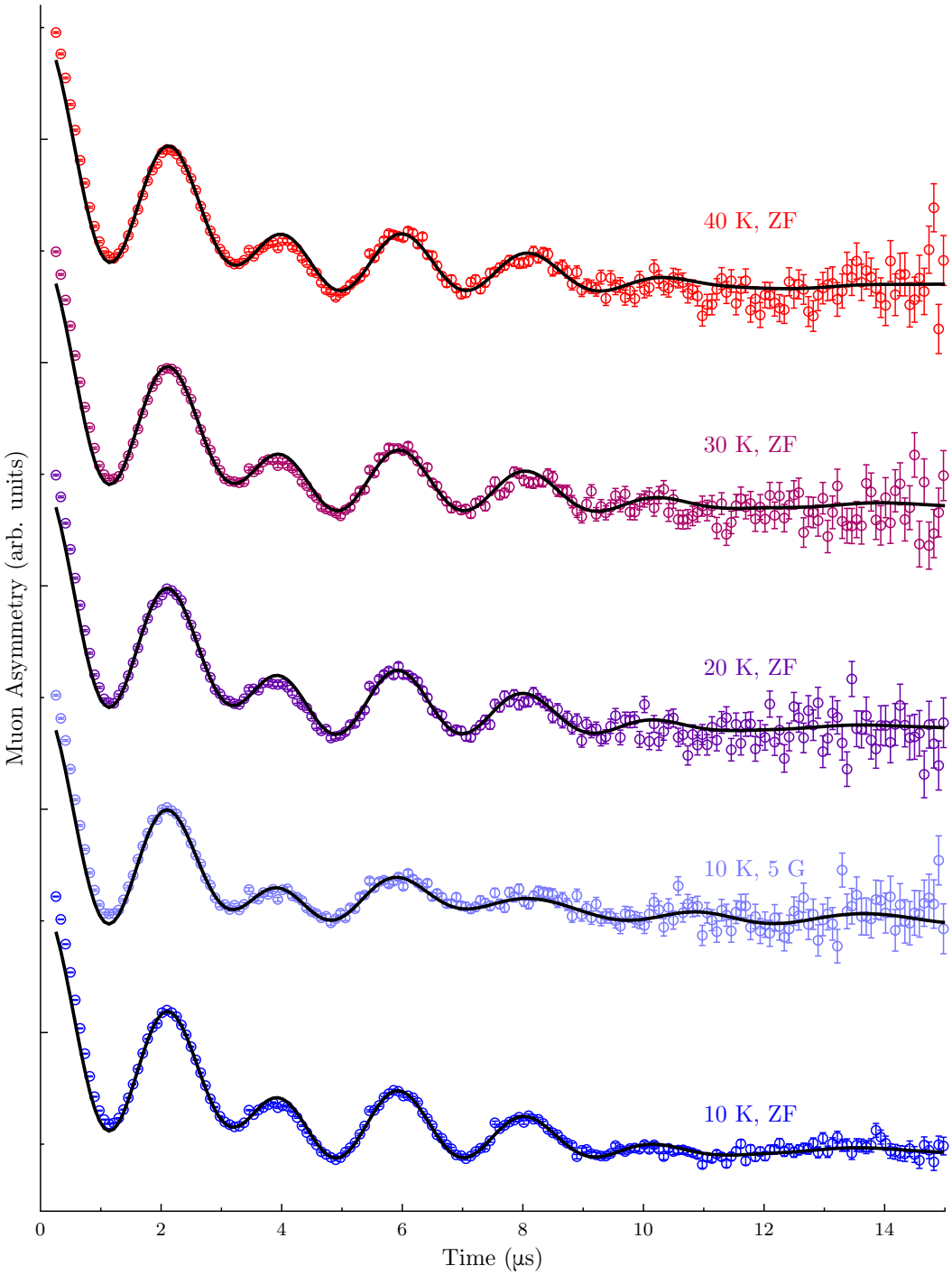


Figure 6.4: Fits of the KPF_6 EMU data, using Equation (6.1). The fits are in a very good agreement with the data for all the measured temperatures.

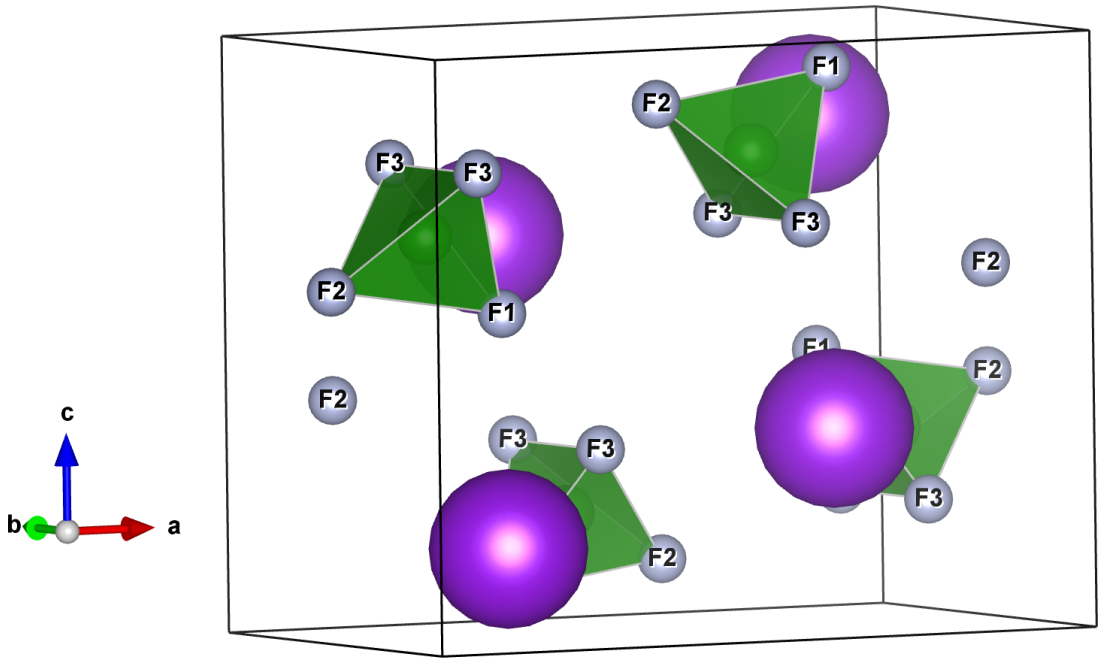


Figure 6.5: Crystal structure of KBF_4. The $[BF_4]^-$ tetrahedra consist of two fluorides in the F3 site, and one in F1 and F2.

position would make them nearest-neighbours, an effect which may be significant. An approach such as that detailed in Ref. [91] would be possible, which considers two separate Hamiltonians of the system: one for before the hop event ($\mathcal{H}_1$) and a different one for after ($\mathcal{H}_2$), with the density matrix taking into account the spins around the muon both pre- and post-hop. This would however be valid only for slow dynamics, as it can only take into account one hop event, and calculating the muon polarisation function would require a prohibitively large Hilbert space which makes the method unfeasible for this compound.

6.4 KBF_4

KBF_4 consists of tetrahedral $[BF_4]^-$ ions intercalated with K^+, in the space group *Pnma* [130]. This structure is shown in Figure 6.5. The fluorines occupy three distinct Wyckoff sites: F1 at $(0.1789, 0.25, 0.556)$, another at $(-0.0814, 0.25, 0.6049)$ (F2), and another at $(0.0774, 0.0440, 0.8039)$ (F3), all of which have multiplicity 4.

Nearest-neighbour fluorines	Number of DFT runs	ΔE (meV)
F1 ↔ F2	6	0
F2 ↔ F3	2	83
F3 ↔ F3	4	100–120
F1 ↔ F3	4	100–200

Table 6.2: KBF_4 DFT+μ results. Each pair of fluorines which had a muon site predicted by DFT+μ is shown, alongside the number of DFT+μ calculations predicting each of these sites. The range of energies of the relaxed supercells for each site is also shown (ΔE is the difference in energy between the site with the lowest energy and the site in question).

6.4.1 Muon site determination

As the fluorine atoms occupy three different Wyckoff sites, determining which site (or sites) the muon stops in is best achieved by DFT+μ. To this extent, I placed muons (modelled by a hydrogen pseudopotential, see Section 3.2.2) in between every pair of fluorines less than 3.3 Å apart in a supercell consisting of $1 \times 2 \times 2$ conventional unit cells, giving the supercell a charge of $+|e|$ due to the muon's charge state. This resulted in twenty starting sites, which were relaxed until the total force on all the atoms fell below a threshold of 51 meV $Å^{-1}$. The final muon sites are listed in Table 6.2, analysed in terms of the total energy of the relaxed supercell.

From these DFT+μ results, it is possible to determine several properties of the KBF_4 muon site. Firstly, there is an absence of any muon sites which are in between two fluorines of type F1 and two of type F2. The closest distance between two F1s (where a line can be drawn between them without touching the other atoms) is 4.21 Å, and for the F2s this is 3.41 Å, which are both larger than the initial distance between all the other pairs of fluorines, suggesting these sites do not minimise the total energy because very large perturbations of the crystal would be required to form such F–μ–F states[13]. Secondly, *all* of the states are formed between fluorines on different tetrahedra ("inter-tetrahedra"), similar to the case

[13]Of course, all the initial muon sites (before relaxation) were between two fluorines closer than 3.3 Å, which excluded all F1↔F1 and F2↔F2 sites – but if these sites have a large enough potential minimum, the relaxation calculation ought to have found them.

for KPF_6 discussed previously. This, as for KPF_6, can be understood by the central boron cation in the polyhedron (B^{3+}) strongly repelling the muon[14].

As each of the states predicted by DFT+μ have the muon in a different environment, each state gives rise to a different muon polarisation. Therefore, to investigate the most likely muon site, I calculated the muon polarisation for muons in each of the sites in Table 6.2. Boron has two isotopes (see Appendix C), both of which have spin $I > \frac{1}{2}$, making it necessary to include both dipolar and quadrupolar terms in the Hamiltonian. Therefore the muon evolves with the Hamiltonian composed of the sum of Equations (3.8) and (4.4),

$$\mathcal{H} = \sum_{i<j} \frac{\mu_0 \gamma_i \gamma_j}{4\pi |\boldsymbol{r_{ij}}|^3} (\boldsymbol{s}_i \cdot \boldsymbol{s}_j - 3(\boldsymbol{s}_i \cdot \hat{\boldsymbol{r}}_i)(\boldsymbol{s}_j \cdot \hat{\boldsymbol{r}}_j)) + \sum_{i \in \mathrm{B}} \frac{eQ(1+\gamma)}{\hbar 2I(2I-1)} \sum_{\alpha\beta} V^i_{\alpha\beta} \hat{I}^i_\alpha \hat{I}^i_\beta, \quad (6.2)$$

where the sum in the second term (over $i \in$ B) is over the boron nuclei only (the other nuclei are spin-$\frac{1}{2}$ and therefore have no quadrupole moment). The external electric field gradient (EFG) $V^i_{\alpha\beta}$ at the site of the ith boron nucleus (with spin operator $\boldsymbol{I}^i$) due to external charges q_j, is calculated as

$$\begin{aligned} V^i_{\alpha\beta} &= \frac{\partial^2 V(\boldsymbol{x}^i)}{\partial x_\alpha \partial x_\beta} \\ &= \sum_{j \neq i} \frac{q_j}{4\pi\epsilon_0} \left(\frac{3(x^i_\alpha - x^j_\alpha)(x^i_\beta - x^j_\beta) - \delta_{\alpha\beta} |\boldsymbol{x}^i - \boldsymbol{x}^j|^2}{|\boldsymbol{x}^i - \boldsymbol{x}^j|^5} \right), \end{aligned} \quad (6.3)$$

summing over all atoms in the lattice up to a radial cutoff, chosen to be 50 Å (this sum converges very quickly, so a larger cutoff was not required). For the purposes of these calculations, I modelled the charge state of the boron to be +3, despite the bond between the fluorine and boron being of a covalent character. A boron in this charge state gives rise to an anti-shielding factor γ_∞ of around -0.144, assuming an average of the values reported by various sources[15] [102, 133–135]. To take into

[14] This is a rather simplistic view, as the intra-tetrahedra bonds of the $[BF_4]^-$ ions are more covalent in character than the other ionic compounds studied in the preceding chapters [131]. Nevertheless, Ref. [132] shows that at the molecular surface of these ions, the electrostatic potential increases as one moves towards the midpoint of two fluorines on the same tetrahedron, consistent with the DFT+μ calculations shown here.

[15] This anti-shielding factor varies from around 0.142 to 0.1453 in the literature, and will vary depending on the charge state and electronic configuration of boron in the material (which, due to the muon's perturbation, may be different for each one!).

account both the boron isotopes, I calculated the total muon polarisation as a weighted sum of the muon polarisation due to muons stopping in sites surrounded by each combination of boron isotopes, that is,

$$P_\mu(t) = \sum_i w^i P_\mu^i(t), \tag{6.4}$$

where the superscript i denotes the combination of isotopes used in the Hamiltonian to calculate the muon polarisation $P_\mu^i(t)$. The term w^i is a weighting factor, which is calculated as a product of the abundances of all the nuclei used to calculate $P_\mu^i(t)$. As a first step, I chose to cut off the Hilbert space when the matrices were of size 4096×4096 (sufficiently large to produce many of the key features of the muon polarisation, while being small enough to not take too long to compute), selecting the specific nuclei used in the calculation by calculating the average dipolar interaction size ω_k as

$$\omega_k = \sum_j v_j \frac{\mu_j}{r_k^3}, \tag{6.5}$$

where the sum is over the isotopes (labelled as j) of atom k (with each isotope having a natural abundance of v_j), and r_k is the distance between the muon and k, a method analogous to that used for KPF_6. The atoms which produced the largest ω_k values and satisfied the Hilbert space cutoff were the ones I included in the calculation of the muon polarisation. For this initial investigation, I did not rescale any interactions to take into account the infinite crystal, as a poor choice of the number of nearest-neighbours to rescale is likely to result in the spectrum becoming distorted. The predicted muon polarisations from the four possible muon sites determined by DFT are plotted in Figure 6.6.

By inspecting Figure 6.6, comparing each of the muon polarisations to the data (in the inset) shows that the muon site is clearly of the type F1↔F3, despite the results from the DFT+μ calculations suggesting a different muon site. This muon site is highly unusual, as some of the fluorines move considerably from their original positions, as is shown in Figure 6.7. In this figure, it can be seen that the muon's perturbation pulls the nearest-neighbour F3 atom away from its $[BF_4]^-$ complex,

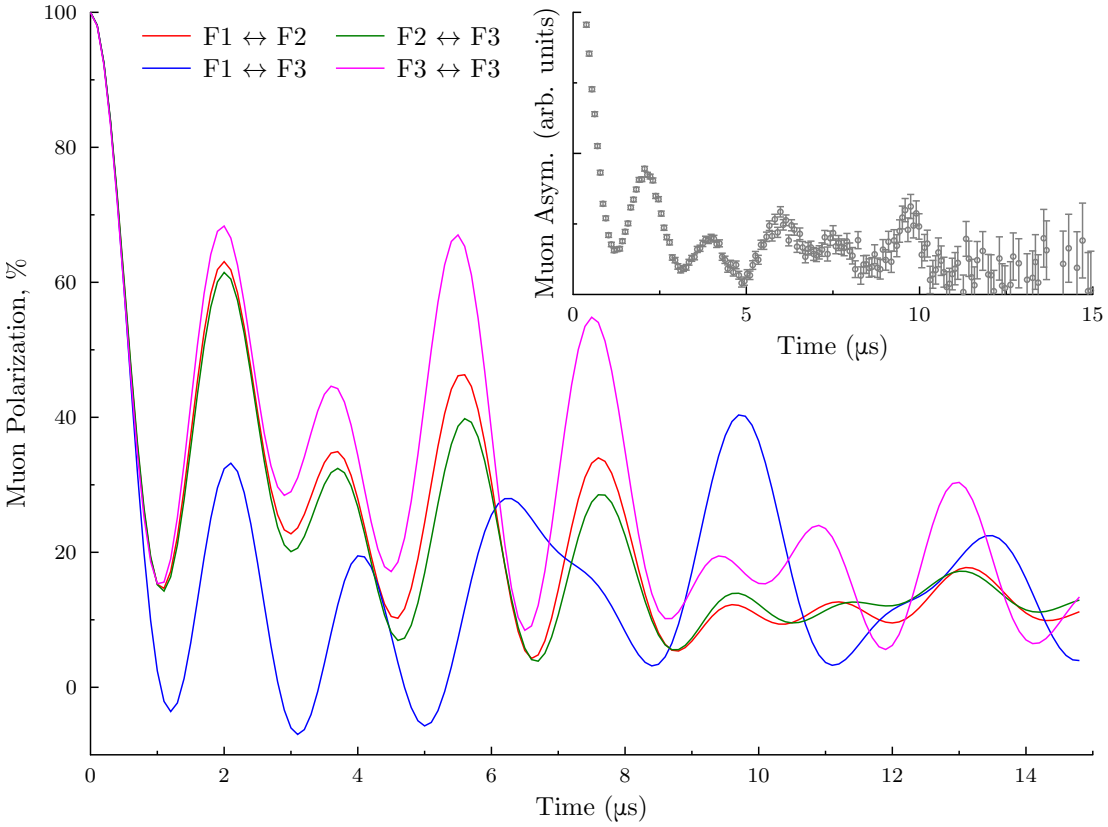


Figure 6.6: Muon states in KBF_4. The muon polarisation expected from muons in all four potential muon states calculated with DFT+μ are plotted. Inset: The muon asymmetry data from the KBF_4 sample.

which then makes the boron move towards its remaining three fluorides (F1, F2 and the other F3), becoming in effect a neutral planar BF_3 ion. The other $[BF_4]^-$ ion is affected far less by the muon perturbations, and all of its constituents remain in a similar location relative to each other, but all have moved slightly towards the muon.

BF_3 is a Lewis acid (a chemical species which has an empty orbital which can accept an electron pair [136]), which is known to accept an F^- ion to form the $[BF_4]^-$ ion. A muon has the effect of reversing this process, removing an F^- ion from the $[BF_4]^-$ ion. This is similar to the way in which the Lewis bases HCN [137] and NH_3 [138] interact with BF_3, with the μ–F complex acting as a Lewis base in this case.

The muon state depicted in Figure 6.7 has many atoms which are perturbed, meaning that to get a full understanding of this the muon polarisation needs to be

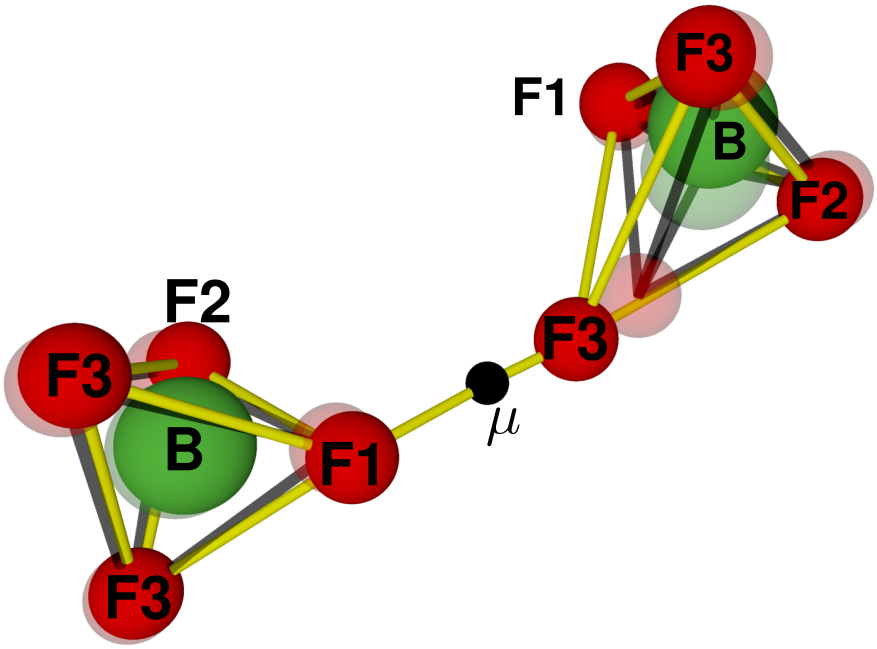


Figure 6.7: Muon-induced perturbations in KBF_4. The muon is represented by the black sphere, fluorine by the red and boron by the green sphere. Distorted (undistorted) positions are shown as solid (translucent) spheres, and the lines connecting the spheres are guides to the eye. The potassium ions are not shown for clarity.

calculated with a larger Hilbert space than what was calculated in the previous compounds studied. To this end, I cut off the Hilbert space when the size of the matrices reached 12544×12544 for the fitting of the μSR asymmetry data (this meant the calculation included the muon, seven fluorines and both borons, even if they are both the isotope with the greater spin (^{10}B)). The initial positions of the nuclei included in the calculation are in Table 6.3.

To model the effects of all the nuclei in the sample affecting the muon's polarisation, I rescaled the distances of the nuclei from the muon for those more distant than F_3 to take into account the second dipole moment of the infinite lattice. However, the fact that boron has two isotopes means that the calculation of the rescaling factor ζ_7 needs to be done with care: for each of the isotope combinations i in Equation (6.4), $\sigma_{\geq \mathrm{nnn}}$ was calculated using Equation (4.1), and then σ_∞ was

Spin	Fractional Position		
μ	0.30857	0.38536	0.45311
F_{nn1} (F3)	0.42260	0.54400	0.45311
F_{nn2} (F1)	0.17890	0.25000	0.55600
F_3 (F3)	0.42260	-0.04400	0.30390
B_1	0.06260	0.25000	0.68970
F_4 (F2)	0.08140	0.75000	0.38510
F_5 (F3)	0.57740	0.45600	0.69610
F_6 (F3)	0.07740	0.45600	0.80390
B_2	0.43740	0.75000	0.18970
F_7 (F2)	0.41860	0.25000	0.89510

Table 6.3: Original positions of the nuclei included in the KBF_4 muon polarisation calculation, ignoring muon perturbations.

calculated in a similar way to Equation (4.3), with

$$\sigma_\infty^2 = \sigma_{\geq \mathrm{nnn}}^2 + \frac{2}{3}\left(\frac{\mu_0}{4\pi}\right)^2 \hbar^2 \gamma_\mu^2 \left[\sum_{r_j < r_{\mathrm{cutoff}}} \frac{\langle \gamma_j^2 I_j(I_j+1) \rangle}{r_j^6} + \int_{r_{\mathrm{cutoff}}}^{\infty} \frac{4\pi r^2}{r^6} n \sum_{j \in \mathrm{u.c.}} \frac{\langle \gamma_j^2 I_j(I_j+1) \rangle}{N_{\mathrm{u.c.}}} \mathrm{d}r \right], \quad (6.6)$$

where all the symbols retain their meanings from Equation (4.3), with the difference being that the quantity $\gamma_j^2 I_j(I_j+1)$ is now in angle brackets, to denote this being averaged over the all the isotopes of the nucleus with label j, weighted by their natural abundances. Additionally, r_j now only takes into account nuclei *beyond* those calculated explicitly, with the second moments of the other nuclei taken into account with the term $\sigma_{\geq \mathrm{nnn}}^2$. This term changes for each isotope combination (labelled with i in Equation (6.4)), which means there are four values of ζ_7 (the subscript 7 here meaning the distances for all the nuclei beyond two closest to the muon (nn1 and nn2) are rescaled, or in other words the seven furthest nuclei from the muon included in the Hamiltonian explicitly). These values of ζ_7 are shown in Table 6.4, assuming the distortions calculated by DFT+μ.

B_1	B_2	w_i	ζ_7
^{10}B	^{10}B	0.0383	0.8992
^{11}B	^{10}B	0.1575	0.9063
^{10}B	^{11}B	0.1575	0.9018
^{11}B	^{11}B	0.6467	0.9085

Table 6.4: ζ_7 values for the combinations of boron isotopes used to calculate the muon polarisation, including the weights w_i, calculated from the product of their abundances.

6.4.2 Data analysis

I fitted the KBF_4 data with the function

$$A(t) = A_{\text{rel}} P_\mu(r_{\text{nn1}}, r_{\text{nn2}}; t) + A_{\text{imp}} e^{-\lambda_{\text{imp}} t} + A_{\text{bg}} e^{-(\sigma t)^2}, \tag{6.7}$$

a similar function to that used for KPF_6 (Equation (6.1)). The first term represents the muons stopped in KBF_4 and evolving as described in the previous section, the second term represents the muons stopping in impurities and causing their polarisation to decay exponentially (this is inevitably a phenomenological relaxation function, as the X-ray data could not conclusively determine what the impurities were). The final term is a Gaussian decay due to muons stopping in the Ag sample holder[16]. The muon polarisation for the muon stopping in KBF_4 uses values for ζ_7 calculated from the DFT+μ results, because having this as a variable parameter would require the introduction of four additional fitting parameters (due to the boron isotope combinations), all of which would change the muon polarisation a similar way resulting in many local minima for the fit.

The fit was in excellent agreement with the data, as depicted in Figure 6.8. The isotope combinations are also depicted in the inset, showing the significant effect of substituting the nearest boron nucleus on the muon polarisation (^{11}B has a larger nuclear moment that ^{10}B, explaining the more significant relaxation which occurs if B_1 is of this species). The nearest-neighbour distances to the muon were $r_{\text{nn1}} = 1.077(1)$ Å and $r_{\text{nn2}} = 1.489(6)$ Å, very close to the values

[16]The use of a Gaussian relaxation for the sample holder and a Lorentzian relaxation function for the sample impurities is a purely based on phenomenology, and were chosen as they provided the best fits to the data.

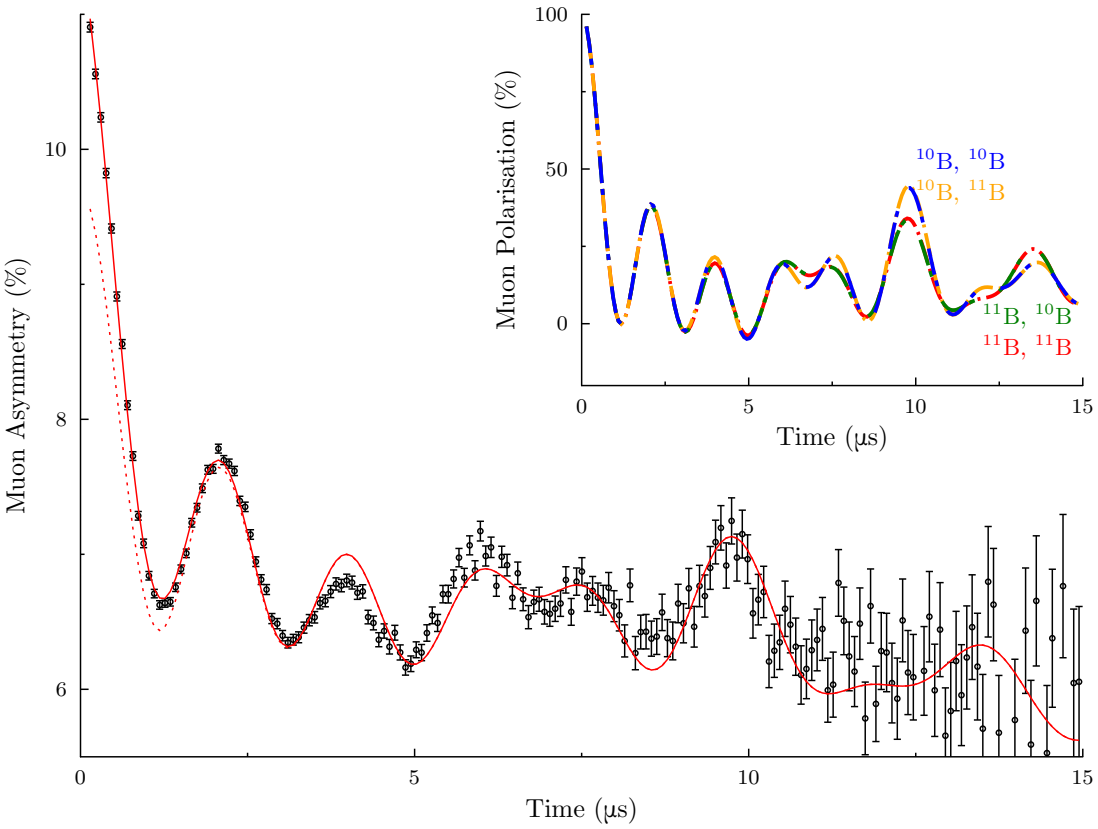


Figure 6.8: KBF_4 μSR fits. The main plot shows the fit of the muon data to Equation (6.7). The inset shows the muon polarisations obtained when the borons in the positions of B_1 and B_2 are either ^{10}B or ^{11}B.

obtained by DFT+μ of 0.908 Å and 1.456 Å respectively. The amplitudes A_{rel} and A_{imp} were 3.21(1)% and 1.8(1)% respectively, suggesting a significant number of muons had not stopped in KBF_4.

Figure 6.8 also shows the importance of including the impurity term in the fitting function: the dashed line represents the fit without including this, which fails to take into account the initial part of the asymmetry. Whether this term is truly taking into account the impurities or not is uncertain: other causes of this could be additional muon states (fitting with combinations of the other muon states suggested by DFT+μ was also attempted, but in every case this resulted in a worse fit to the data). AFD states, like those studied in Chapter 5 are also unlikely, and would result in a component of the muon asymmetry which evolves much more slowly than what is measured here.

6.5 Conclusion

Here I have shown that the model fluorides KPF_6 and KBF_4 produce muon polarisations which can be used to deduce muon sites to a very high degree of accuracy. In addition, I have shown that the nature of the muon site in polyatomic ions tends to be of the type that bridges two separate ions, which appears to be due to the central atom having a strong positive charge. In particular, for KBF_4 the muon site appears to be analogous to the way in which Lewis bases interact with BF_3 ions, a reaction which can be observed by a careful analysis of F–μ–F states, and may be present in other compounds.

These results have strong implications for the study of molecular magnets: often $[BF_4]^-$ or $[PF_6]^-$ ions are used as anions to separate the magnetic cations, and these materials have been studied extensively with μSR [75, 139], but owing to their complicated nature, it has been very difficult to accurately determine the muon sites in these compounds and hence get a full understanding of the way in which the muon perturbs the host. The methods used in this chapter to determine the muon sites can be extended to these, which will significantly improve their analysis.

7

$KAgF_3$: a Magnetic Fluoride

Contents

7.1 Introduction 89
7.2 DFT+μ 92
7.3 μSR experiments 93
7.3.1 $T < T_c$: measuring the magnetic order 94
7.3.2 $T > T_c$: measuring the muon-induced perturbations . . 96
7.4 Analysis 101
7.4.1 Calculating the Ag^{2+} moment 101
7.4.2 F–μ states and magnetic order 102
7.5 Conclusion 106

7.1 Introduction

All of the compounds considered in the previous chapters have been primarily model systems, specifically wide bandgap fluorides with closed-shell ions, ensuring that the electronic structure of the materials had a minimal effect on the muon's polarisation. This meant that the muon only interacted with its surrounding nuclear spins, and could be described with a Hamiltonian with only dipolar and sometimes quadrupolar terms (where necessary). Yet all the most interesting materials are those where the electronic structure plays a key role in their physical properties, and these materials are arguably where the analysis techniques developed in this

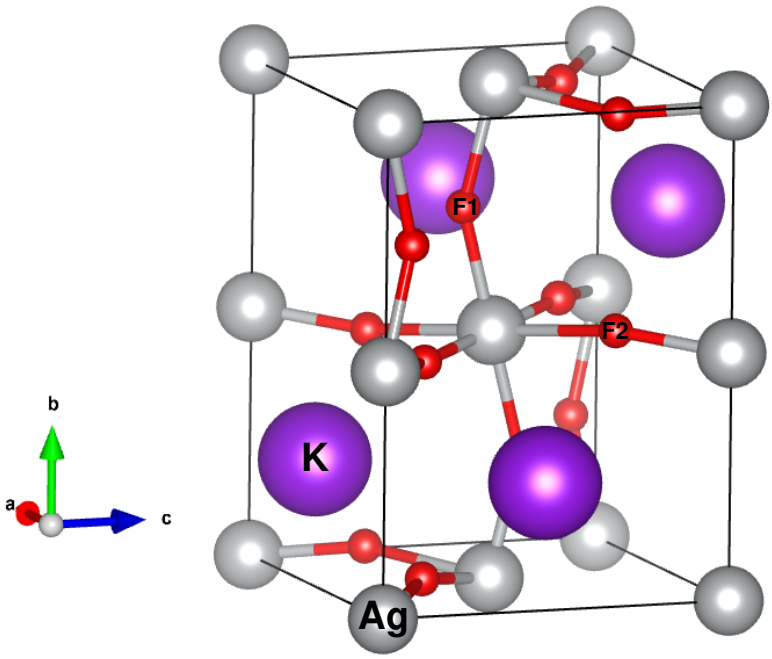


Figure 7.1: Crystal structure of $KAgF_3$. The Ag^{2+} ions are connected in Ag–F–Ag chains in the **b** direction by fluorines of the type F1, and the **a**-**c** planes contain two dimensional AgF_2 sheets, using the fluorine of the type F2.

thesis would be most useful. One particular family of materials which would benefit heavily are the fluoroargentates (materials composed of silver and fluorine), which have been predicted to be a potential new class of superconductors [140–142], due to their similarity to copper (II) oxides (which are the precursors to a family of high temperature superconductors, known as cuprates [143–146]).

Potassium trifluoroargentate (II) ($KAgF_3$) is an insulator which contains Ag in the 2+ oxidation state, resulting in it having moments with electronic spin $S = \frac{1}{2}$ [147][1]. The material crystallises into a deformed perovskite structure with space group *Pnma*, which is depicted in Figure 7.1. The structure at 80 K has Ag at $(0, 0, 0)$, K at $(0.0529, 0.25, 0.486)$ and F1 at $(0.483, 0.25, 0.579)$, all with multiplicity 4, and F2 at $(0.317, 0.469, 0.236)$ with multiplicity 8. Upon heating, at a temperature between 225 and 235 K, the compound undergoes a structural phase transition to a structure with space group *Pcma*.

[1]Hund's rules would suggest a total angular momentum quantum number of $\frac{5}{2}$, but it is not uncommon for Hund's rules to fail for d electrons due to the effects of the crystal field being significant (a phenomenon called orbital quenching), giving $L = 0$ [148].

Previous work on $KAgF_3$ has involved X-ray diffraction and magnetic susceptibility measurements [147], and extensive DFT+U studies [149]. The magnetic susceptibility measurements show features at 35 K and 66 K, which are attributed to magnetic impurities (although earlier studies [150] suggest that the material undergoes a magnetic phase transition at 64 K, albeit in a much less clean sample), and it was suggested that the electronic moments on the Ag^{2+} ions order antiferromagnetically along **b** in a 1D Heisenberg-like chain[2], with a relatively large exchange coupling constant[3] of $J = -97$ meV.

DFT+U calculations[4] on $KAgF_3$ also predict the Ag^{2+} moments to align antiferromagnetically along the **b** axis, and ferromagnetically (with a much smaller exchange constant) in the **a**-**c** plane [149]. The ordering of the Ag^{2+} moments arises due to the fluoride ions mediating a superexchange interaction [153], as is typical for ionic solids. These results also suggest that the electronic moment on the Ag ions is around $0.62\mu_B$ and the magnetic exchange coupling is $J = -136$ meV along **b**, and $J_\perp = 5.8$ meV between the Ag^{2+} ions in the **a**-**c** planes. The vast difference between these values suggest the compound has a quasi-1D magnetic structure, consistent with the magnetic susceptibility measurements (but, as the authors of the DFT+U study acknowledge, DFT+U tends to overestimate the size of magnetic exchange interactions [154]).

All of the scientific work on $KAgF_3$ so far in the literature has been on either bulk methods or ab initio calculations to characterise the compound. However, in order to understand the true nature of the interactions between its constituents, it is necessary to use a local technique. A detailed μSR study, looking at both the magnetic phase below the transition temperature, and the F–μ–F states at

[2] A Heisenberg chain has nearest-neighbour spins $\boldsymbol{S}_i$ and $\boldsymbol{S}_j$ interacting with the Hamiltonian $\mathcal{H} = -J_{ij}\boldsymbol{S}_j \cdot \boldsymbol{S}_j$ [148].

[3] For comparison, the dipolar interaction between the muon and the Ag ion is of the order of 100 peV, so the muon has nowhere near enough energy to flip the electronic moments, and hence can measure this magnetic ordering without directly affecting it.

[4] DFT+U is DFT where the energy functional includes a Hubbard U interaction of the form $\sum_I \frac{U^I}{2} \sum_{m,\sigma\neq m',\sigma'} n_m^{l\sigma} n_{m'}^{l'\sigma'}$ for electrons in atomic site I, state m and with spin σ. This introduces an additional Coulomb interaction between the states, encouraging them to localise [151, 152].

temperatures above, can provide a much more detailed understanding of the nature of the magnetic interactions in this material.

7.2 DFT+μ

As a first step to locate the muon stopping site, *ab initio* DFT calculations were performed with Quantum Espresso [89], as discussed in Section 3.2. The calculations were performed on a supercell containing $1 \times 2 \times 2$ conventional unit cells, using a $5 \times 4 \times 5$ Monkhorst–Pack grid, and ultrasoft pseudopotentials to model the electronic wavefunctions of the atoms. Specifically, for the Ag the electrons treated as valence were the 5s, 5p and 4d, with all the other electrons treated as core.

Density functional theory (DFT) calculations undertaken previously on $KAgF_3$ required a Hubbard U interaction to be included on the electrons of the Ag ions. I found that the DFT converged successfully without the inclusion of this interaction, and reproduced the experimentally measured lattice parameters to around 3–4 %. Nevertheless, the muon sites were calculated both with and without the inclusion of the Hubbard U interaction, to test the robustness of the method. Using the linear response technique as detailed in Ref. [155], I estimated U to be 1.475 eV, somewhat smaller than the 5 eV used in other studies [150] (but note that Hubbard U values depend strongly on the pseudopotentials used).

The DFT+μ calculations resulted in two possible muon sites, which are shown in Table 7.1, with all other sites discounted due to having an energy far above these. The locations of these two candidate muon sites are depicted in the $KAgF_3$ unit cell in Figure 7.2. DFT+μ predicts that the muon will draw in the two nearest fluorines towards it for both sites, as is usually the case for ionic fluorides. Although DFT often struggles to calculate the extent of these distortions to a high accuracy, these calculations estimate that for site 1 the nearest-neighbour fluorine goes from being 1.26 Å away from the muon to 1.11 Å, and for site 2 the nearest-neighbour moves from 1.91 Å to 1.05 Å away, and these bond length estimates are likely to be correct to within 0.1–0.2 Å [60]. The two nearest-neighbours of site 1 are two fluorines which

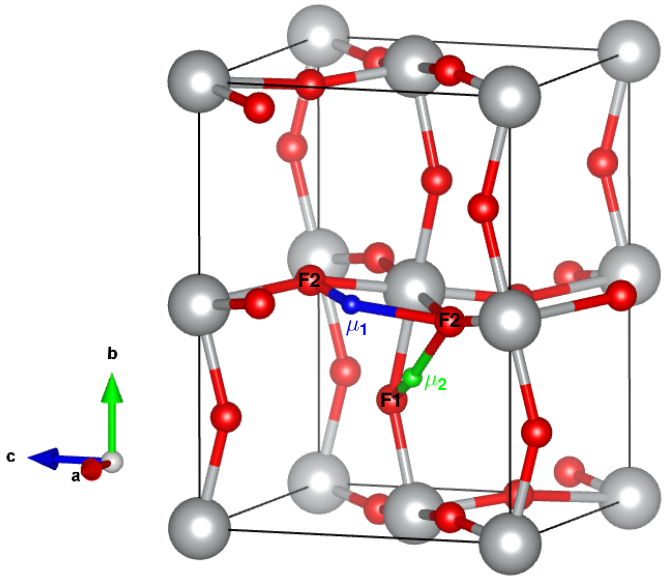


Figure 7.2: Potential $KAgF_3$ muon sites. The two candidate muon sites as described in Table 7.1 are shown. Neither the muon-induced structural perturbations nor the potassium ions are shown for visual clarity.

occupy the same Wyckoff site (F2), and site 2 is between two fluorines occupying different Wyckoff sites, hence forming an asymmetric F–μ–F state.

Site	Position (fractional coordinates)	Energy above min (eV)	
		DFT	DFT+U
1	(0.7857, 0.4931, 0.5933)	-	0
2	(0.6619, 0.3221, 0.4446)	0	151

Table 7.1: DFT+μ results for $KAgF_3$, showing the muon sites and their energies above the lowest energy site (note that site 1 was not realised in the DFT calculations when no Hubbard U was included).

7.3 μSR experiments

The $KAgF_3$ sample was synthesised by W. Grochala's research group. Previous attempts at synthesising $KAgF_3$ involved reacting AgF_2 and KF, but this reportedly created a sample with a significant amount of impurities. Therefore, the approach taken here was to create a sample of $KAgF_4$ (which has Ag in the 3+ oxidation state) by fluorinating AgF_2 and KF with around 270 kPa of F_2, over four days

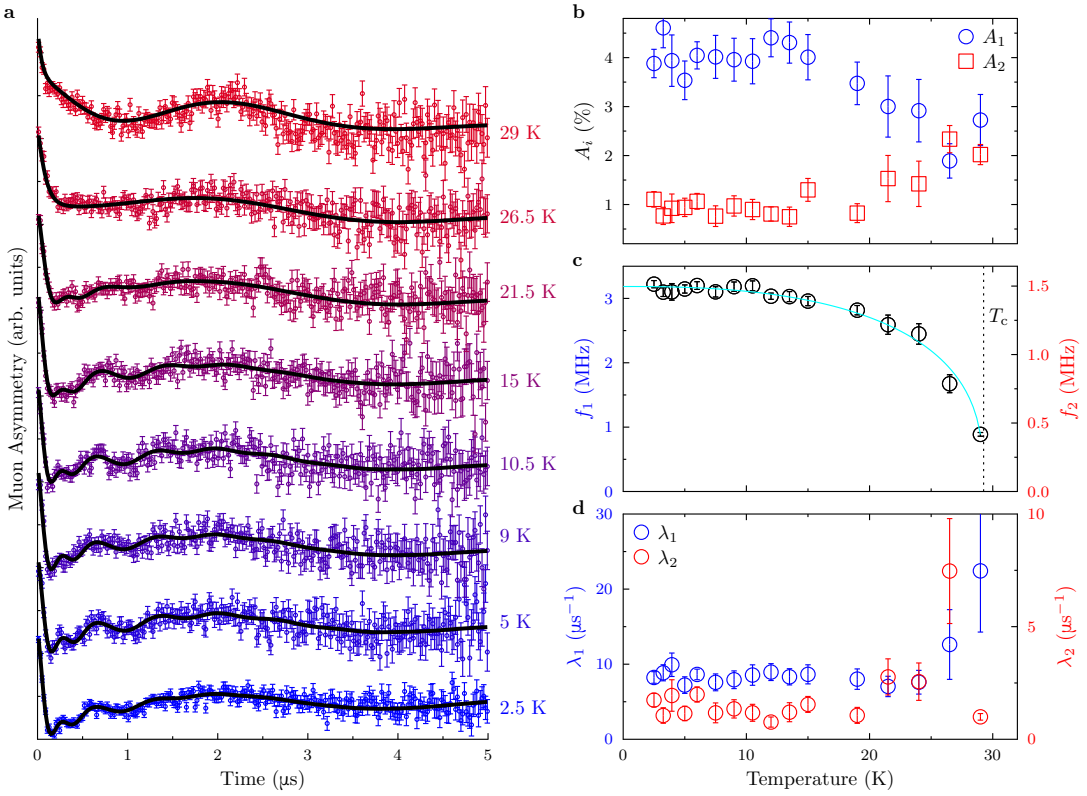


Figure 7.3: PSI $KAgF_3$ data and fits. **a** shows the PSI data with the sample holder background removed, where the oscillations can be clearly observed. The black lines represent the fit to Equation (7.2), as described in the text. **b** shows how the amplitudes of the two oscillating components A_1 and A_2 vary with temperature, **c** shows the frequency of these oscillations (the cyan line shows the fit to the model as described in the text), and **d** the relaxation of these two components.

at 575 K (see the Supplementary Information in Ref. [147] for more information). This was then thermally decomposed at 715 K under a dynamic vacuum over six days to create the high purity $KAgF_3$ sample used in these experiments.

7.3.1 $T < T_c$: measuring the magnetic order

The PSI data, taken with the GPS instrument [40], are shown in Figure 7.3**a**. This shows a clear oscillatory feature at short timescales, which is very heavily damped. This feature remains present up to around 31 K, above which no oscillations due to the ordered electronic moments can be observed in the muon asymmetry.

Some muons were found to stop in the Cu sample holder[5], which creates a

[5]A copper sample holder was required as $KAgF_3$ reacts violently with water, and the Ag foil holders (as used in the other experiments) would be insufficient at keeping moisture out.

Kubo–Toyabe component in the muon asymmetry [72, 156], which was modelled by the function

$$A_{\mathrm{KT}}(t) = A_{\mathrm{KT}}(0)\left(\frac{1}{3} + \frac{2}{3}(1-\Delta^2 t^2)\exp\left(-\frac{\Delta^2 t^2}{2}\right)\right)e^{-\lambda_{\mathrm{KT}} t}, \tag{7.1}$$

where Δ is the standard deviation of the internal fields in the Cu, $A_{\mathrm{KT}}(0)$ is the amplitude of the asymmetry due to muons stopping in the sample holder, and λ_{KT} is a phenomenological parameter to crudely model muon diffusion. For the PSI data, these parameters were found to be $\Delta = 0.180(5)$ $\mu\mathrm{s}^{-1}$, $A_{\mathrm{KT}}(0) = 11.47(6)\%$, and $\lambda_{\mathrm{KT}} = 0.353(3)$ $\mu\mathrm{s}^{-1}$, and this function was subtracted from the data for all subsequent analysis.

The background-corrected data were fitted with the function

$$A(t) = \sum_{i=1}^{3} A_i \cos(2\pi f_i t - \phi_i)e^{-\lambda_i t} + A_{\mathrm{bg}} e^{-\lambda_{\mathrm{bg}} t}, \tag{7.2}$$

where each component is usually interpreted as muons stopping in different sites in the sample, with each one precessing in its local magnetic field ($B_i = 2\pi f_i/\gamma_\mu$) (see Section 2.2), with a relaxation $e^{-\lambda_i t}$ due to field fluctuations caused by spin dynamics and inhomogeneity. Many of these fitting parameters were found to be constant throughout the range of the temperatures studied, so they were fixed to the following values: $\phi_1 = 0 \pm 10°$, $\phi_2 = 0.0(1)°$, $A_3 = 0.85(16)\%$, $\phi_3 = 151 \pm 13°$, $f_3 = 0.277(10)$ MHz, and $\lambda_3 = 0.25(10)$ $\mu\mathrm{s}^{-1}$. After initially being allowed to vary, it was found that the ratio between the frequencies f_1 and f_2 was constant at around $1 : 0.47$, and was fixed for the subsequent analysis. The values of the parameters which were allowed to vary are plotted in Figure 7.3**b**. The oscillations with amplitudes A_1 and A_2 are clearly due to muons stopping in the $KAgF_3$ sample, the origin of which is discussed in Section 7.4. As the A_3 term exhibits no order parameter-like behaviour, it can be assumed to be due to a muon stopping in an impurity in the sample, the frequency of which is consistent with the muon precessing in a very small magnetic field, *or* it may be due the muon becoming entangled with fluoride impurities leading to very low amplitude F–μ–F oscillations.

The temperature dependence of A_1 and A_2 is very unusual and is a significant point which I will subsequently return to.

The f_1 values were fitted to the phenomenological fitting function

$$f(T) = f_0\left(1 - \left(\frac{T}{T_c}\right)^{\alpha}\right)^{\beta}, \tag{7.3}$$

to model the critical behaviour of this low temperature phase[6]. The fitting parameters obtained were $T_c = 29.26(2)$ K, $f_0 = 3.185(15)$ MHz, $\alpha = 2.5(1)$ and $\beta = 0.335(7)$. The critical temperature T_c is slightly lower than the 35 K measured by magnetic susceptibility [147], which was also observed in the ISIS data. The value of β characterises the critical behaviour of the sample, and is consistent with the value one would expect from a 3D Ising-like system (which predicts $\beta = 0.326$ [29]), though the number of data points in the critical regime is very low and so this should only be taken as a crude estimate.

7.3.2 $T > T_c$: measuring the muon-induced perturbations

The μSR data taken with the MuSR instrument at ISIS [39] for some temperatures are shown in Figure 7.4. Due to the superior decay statistics, it is possible to measure the muon asymmetry over a much longer timescale than PSI, although it is not possible to resolve the oscillations at the shorter timescales (as shown in the inset). These data show that clear F–μ–F oscillations start to appear at around 30 K, and are very pronounced at about 40 K. The presence of these oscillations is indicative of a lack of magnetic order at these temperatures, as the dipole-dipole coupling between the muon and fluorine is much smaller than the Zeeman interaction of the muon in its local magnetic field.

The muon asymmetry data were fitted to the function

$$A(t) = A_r P_{F\mu F}(r_{nn1}, r_{nn2}, r_{\mu Ag}; t) + A_{Cu} G_{DKT}(\Delta, \nu; t) + A_{bg}, \tag{7.4}$$

[6]This phenomenological formula is designed to replicate the behaviour of the system throughout its phase transition. When T is close to T_c, $\frac{T}{T_c} = 1 - \epsilon$ (with $\epsilon \ll 1$), so $f(T) = f_0\alpha^{\beta}\left(1 - \frac{T}{T_c}\right)^{\beta}$, so the behaviour of this function in the critical regime is independent of α (which is just there to fit the low-temperature part of the data [29].

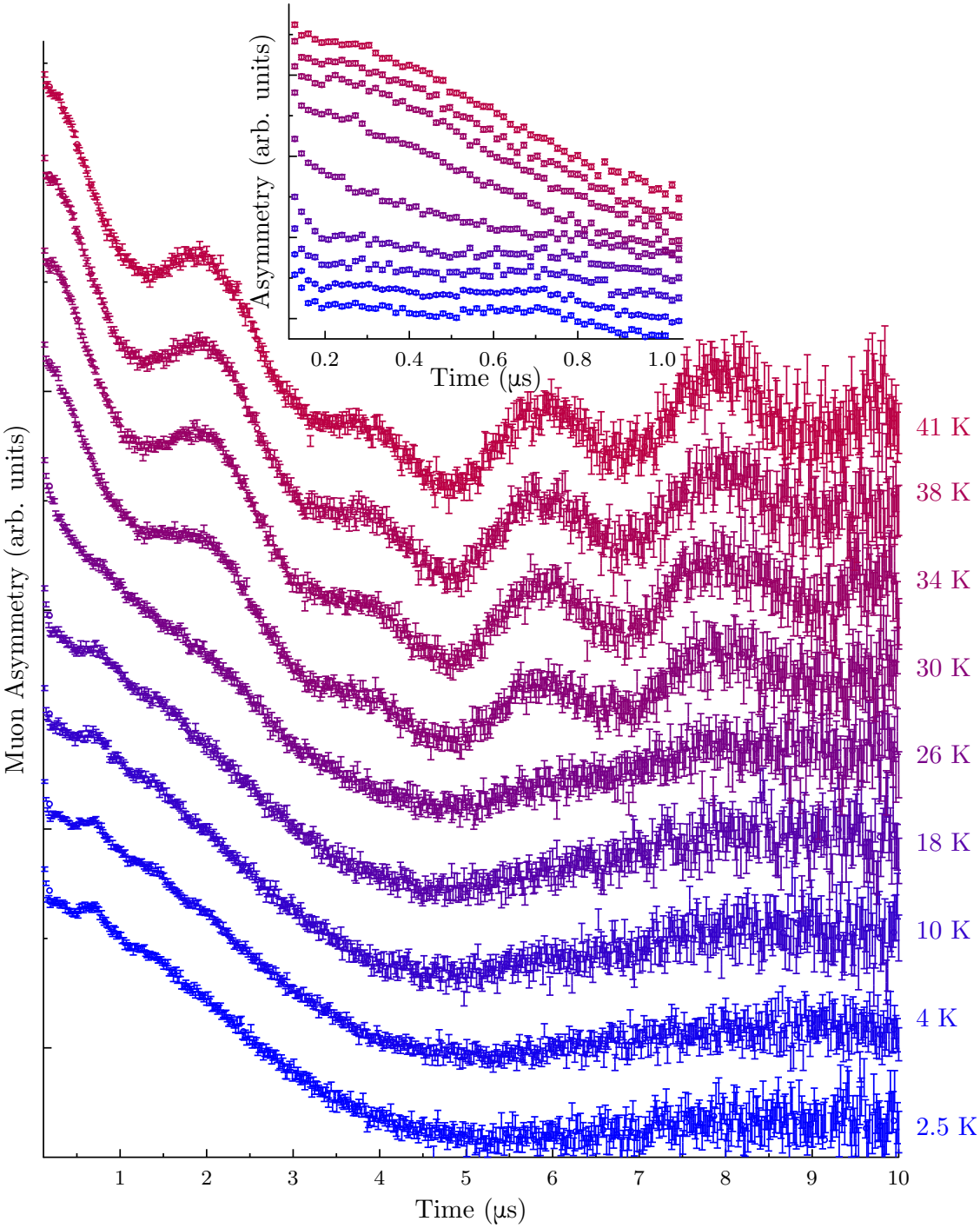


Figure 7.4: $KAgF_3$ μSR data taken with MuSR. The oscillations observed above 30 K are due to the muon entering into an F–μ–F state, due to the entanglement between the muon and the nearest fluorine nuclei. The inset shows the data in the main graph at short times, where one can see the onset of magnetic order in the sample (which is resolved better in the PSI data plotted in Figure 7.3**a**).

where the first term represents muons stopped in the $KAgF_3$ crystal and evolving due to the entanglement between itself and the surrounding fluorine nuclei. This function has the fitting parameters r_{nn1} and r_{nn2} to represent the distance from the muon to the closest and next-closest nearest neighbour fluorines respectively (μ_2 to the nearest F2 and F1 in Figure 7.2 respectively), and $r_{\mu\mathrm{Ag}}$ is the distance from the muon to the nearest-neighbour Ag ion. Note that, as both Ag isotopes have a very small nuclear moment, they have a negligible effect on the μSR spectrum (see Appendix C), so the fitting parameter $r_{\mu\mathrm{Ag}}$ keeps the Ag stationary and moves the muon away from it. This in effect fits the next-nearest neighbour rescaling factor ζ (as defined in Eq. (4.2)), as changing the muon position changes its decohering environment, and also fits the F–μ–F bond angle as increasing $r_{\mu\mathrm{Ag}}$ moves the muon away from both the nearest neighbour fluorines. The second term represents muons stopped in the Cu sample holder, and the final term represents muons stopped elsewhere but not undergoing any precession or relaxation which can be measured.

The Cu sample holder again produces a Kubo–Toyabe background, which was modelled by the dynamical Kubo–Toyabe function as described by Kadono et al. [72],

$$G_{\mathrm{DKT}}(t) = g(t)e^{-\nu t} + \nu \int_0^t g(\tau)e^{-\nu\tau} G_{\mathrm{DKT}}(t-\tau)\mathrm{d}\tau, \tag{7.5}$$

with

$$g(t) = \frac{1}{3} + \frac{2}{3}(1-\Delta^2 t^2)\exp\left(-\frac{\Delta^2 t^2}{2}\right). \tag{7.6}$$

Note that the dynamics in this case are dealt with by the more rigorous strong collision model; this was not required for the PSI data as the dynamics only affect the data at long times.

Initially, in an attempt to locate the muon stopping site, the muon polarisation $P_{\mathrm{F}\mu\mathrm{F}}(t)$ for both site 1 and site 2 (Table 7.1) was fitted to the data at a temperature[7] of 60 K. Unfortunately, both muon sites appear to have an almost identical muon polarisation, as shown in Figure 7.5. This is mostly because both isotopes of Ag have a very small nuclear moment (see Appendix C), as do the K isotopes,

[7] These sites were fitted at 60 K because it is far enough above the magnetic ordering temperature so that the F–μ–F states dominate, but a low enough temperature so that muon diffusion does not occur.

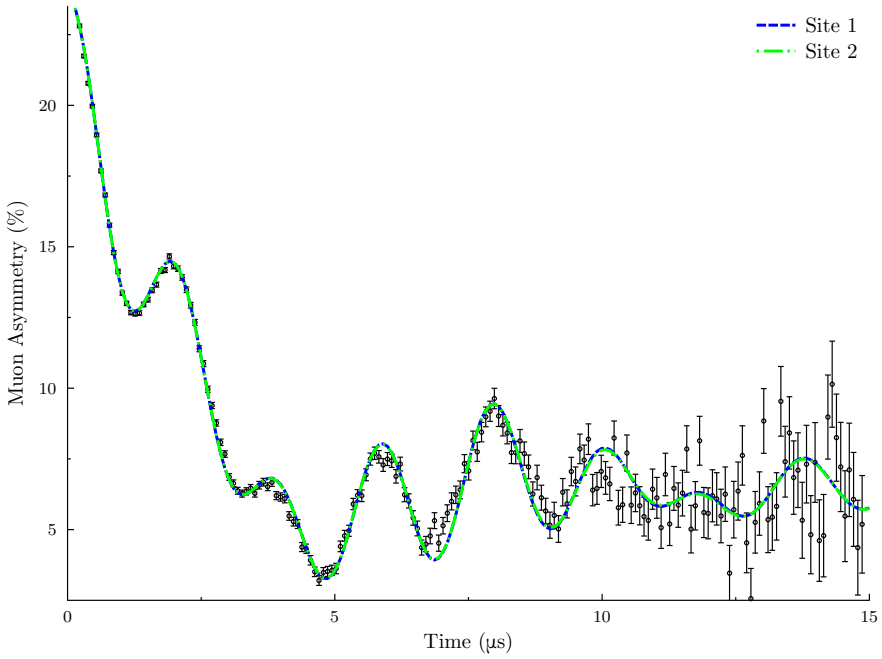


Figure 7.5: $KAgF_3$ fits for both DFT sites. Both sites discussed in Table 7.1 were fitted to the ISIS data at 60 K using Equation (7.4).

so the muon polarisation is dominated by the fluorine nuclei. As the distances between the muon and the two nearest-neighbour nuclei were fitting parameters, the only method of distinguishing between the two potential muon sites is by analysing the decohering environment of more distant spins, which is similar for both sites. Nevertheless, the careful analysis of the dipole fields of both sites and the comparison of this to the PSI data (as discussed in Section 7.4), shows that the only site which is realised by the muon is site 2.

The fits to Equation (7.4) are shown in Figure 7.6**a** and the fitting parameters obtained are plotted in Figure 7.6**b** and **c**. Figure 7.6**a** demonstrates the impressive agreement between the model and the data up to 105 K (muon diffusion occurs at very high temperatures and this is outside the scope of this model[8]). The change in A_{bg} and A_{r} is somewhat unusual, suggesting some sort of phase transition in the sample between 50 and 70 K, but there is insufficient muon data in this

[8]One approach to model this is to apply the strong collision model in Equation (7.5) to the F–μ–F polarisation function, but this would not properly take into account the fact that the fluorines will no longer be in a completely pure state when the muon diffuses to them. This is a point I will discuss further in the Conclusion of this thesis.

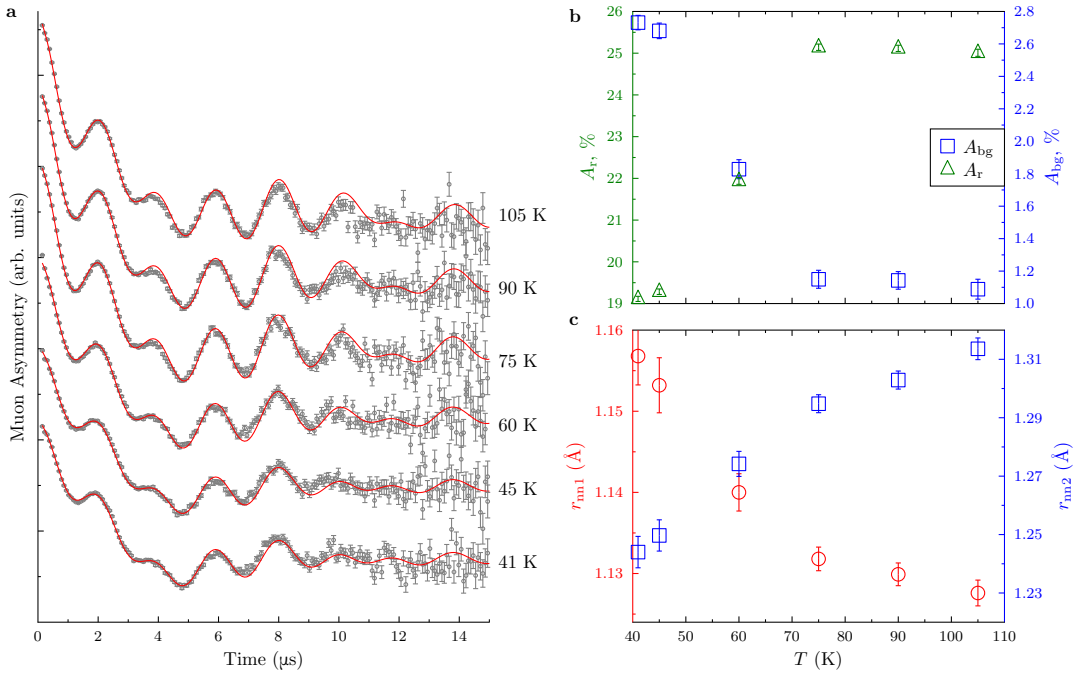


Figure 7.6: ISIS $KAgF_3$ data and fits. **a** shows the fits to the data using the model described in the text. **b** shows the variation of the relaxing asymmetry A_r and background asymmetry A_{bg} with temperature T, and **c** shows how the μ–F distances r_{nn1} and r_{nn2} vary.

temperature range to be able to determine the cause of this. Yet, it is important to note that as F–μ–F states are highly suppressed by magnetic fields, the origin of this change is most likely to be the impurities in the sample rather than the $KAgF_3$ itself, as any magnetic ordering in the compound is very likely to suppress the formation of the states.

The fits also show that the F–μ–F complex changes slightly with temperature, with a change in bond length of around 0.05 Å across the whole temperature range. This is likely to be due to the way in which the entire structure of the crystal changes with temperature, as has been reported previously [147]. Additionally, the μ–Ag distance $r_{\mu Ag}$ varied very little with temperature, and was found to be 2.28(4) Å, slightly smaller than the value of 2.36 Å calculated with DFT+μ.

7.4 Analysis

7.4.1 Calculating the Ag^{2+} moment

A muon implanted in a magnetically ordered sample precesses in its local magnetic field due to the Zeeman interaction, as discussed in Section 2.2. Assuming that the only origin of this field in $KAgF_3$ is due to the dipolar field of the surrounding electronic magnetic moments, the local field of the muon $\mathbf{B}_{\text{dip}}$ can be calculated as

$$\mathbf{B}_{\text{dip}} = \sum_i \frac{\mu_0}{4\pi r_i^3}\Big(3(\boldsymbol{\mu}_i \cdot \hat{\boldsymbol{r}}_i)\hat{\boldsymbol{r}}_i - \boldsymbol{\mu}_i\Big), \tag{7.7}$$

where the sum is taken over the surrounding Ag ions with a magnetic moment $\boldsymbol{\mu}_i$ at a distance r_i from the muon. I calculated this sum over a large Lorentz sphere of radius 150 Å, and as the material is antiferromagnetically ordered the lack of bulk magnetisation means no additional term was required to account for moments beyond this.

Using Equation (7.7), I calculated the dipole field at both the muon stopping sites predicted by DFT+μ, assuming that the moments were ordered ferromagnetically in the **a**-**c** plane and antiferromagnetically along **b**, with all moments constrained to point in the **c** direction. From this, assuming the moment of the Ag ions $\mu_{\text{Ag}} = 0.55\mu_{\text{B}}$ (from DFT calculations by W. Grochala's research group), the field at the muon site would be 723 Gauss for site 1, and 265 Gauss for site 2, leading to muon precession frequencies of around 9.8 MHz and 3.6 MHz respectively. The precession frequency of site 2 is significantly closer to that measured, and therefore is assumed to be the correct muon site for the rest of this analysis.

As the distance between the muon and the nearest Ag ion was found to be 2.28(4) Å by fitting the ISIS data, this can be used to determine the moment on the Ag^{2+} ions using the fact that the field at the muon site is directly proportional to the size of the moments. This results in a moment on the Ag^{2+} ions of $\mu_{\text{Ag}} = 0.488(2)\mu_{\text{B}}$, slightly smaller than the value of $0.62\mu_{\text{B}}$ calculated with DFT in the literature [149].

Other valid potential magnetic structures for this compound have the moments aligned along the **a** direction, and in any other direction along the **a**-**c** plane (neutron

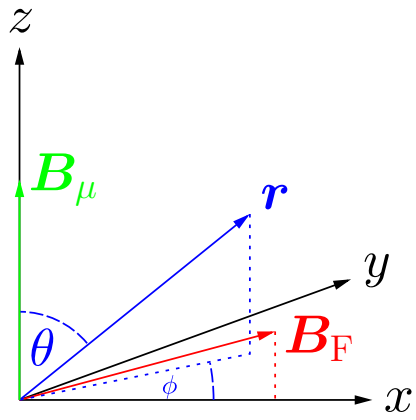


Figure 7.7: Coordinate system used for the calculation of F–μ states in a magnetic field. The coordinates are aligned such that the field on the muon is in along z, and such that the component of the fluorine's field along y is zero.

scattering data by M. Braden's research group suggests no other orientation of the moments is possible). If the moments are aligned along **a**, following the same calculation as above results in an electronic moment on the Ag^{2+} ions of $0.189(1)\mu_B$, which is significantly smaller than the moment calculated from both the neutron data and by the DFT calculations, suggesting that this magnetic structure is highly unlikely. If the moments are aligned along an intermediate direction in the **a**-**c** plane, one would expect the muon data to have two frequencies with an equal magnitude (owing to the site symmetry), which is not realised in the data (although note that the measured muon precession at this frequency relaxes very quickly, so moments pointing in an intermediate direction cannot conclusively be ruled out).

7.4.2 F–μ states and magnetic order

As discussed in Section 7.3.1, the PSI data show two oscillations with frequencies f_1 and f_2 which follow the same order parameter. The two frequencies could be associated with two distinct muon sites, but the temperature-dependent nature of the amplitudes A_1 and A_2 shown in Fig. 7.3**b**, together with the single site assumed for fitting the F–μ–F oscillations (which works so well, as shown in Fig. 7.6**a**), point instead to a different interpretation.

Consider a muon coupled to a single fluorine, with both spins in their own local magnetic fields $\boldsymbol{B}_\mu$ and $\boldsymbol{B}_\mathrm{F}$. If the alignment of the axis is chosen such that $\boldsymbol{B}_\mu$ is along $\hat{\boldsymbol{z}}$ and the $\hat{\boldsymbol{y}}$ component of $\boldsymbol{B}_\mathrm{F}$ is zero (see Figure 7.7), then the Zeeman Hamiltonian is

$$\frac{\mathcal{H}^{(0)}}{\hbar} = \begin{pmatrix} \omega_\mu + b_z\omega_\mathrm{F} & b_x\omega_\mathrm{F} & 0 & 0 \\ b_x\omega_\mathrm{F} & \omega_\mu - b_z\omega_\mathrm{F} & 0 & 0 \\ 0 & 0 & -\omega_\mu + b_z\omega_\mathrm{F} & b_x\omega_\mathrm{F} \\ 0 & 0 & b_x\omega_\mathrm{F} & -\omega_\mu - b_z\omega_\mathrm{F} \end{pmatrix}, \tag{7.8}$$

where b_x and b_z are the components of $\hat{\boldsymbol{B}}_\mathrm{F}$ in the x and z direction respectively, and $\omega_{\mu,\mathrm{F}} = \gamma_{\mu,\mathrm{F}} B_{\mu,\mathrm{F}}$. This matrix has eigenvalues $\omega_i^{(0)}$ and corresponding eigenstates $|i^{(0)}\rangle$ of

$$\omega_1^{(0)} = \frac{1}{2}(\omega_\mu + \omega_\mathrm{F}), \qquad |1^{(0)}\rangle = \frac{1}{\sqrt{2(1-b_z)}} \begin{bmatrix} b_x \\ 1-b_z \\ 0 \\ 0 \end{bmatrix},$$

$$\omega_2^{(0)} = \frac{1}{2}(\omega_\mu - \omega_\mathrm{F}), \qquad |2^{(0)}\rangle = \frac{1}{\sqrt{2(1+b_z)}} \begin{bmatrix} -b_x \\ 1+b_z \\ 0 \\ 0 \end{bmatrix},$$

$$\omega_3^{(0)} = \frac{1}{2}(-\omega_\mu + \omega_\mathrm{F}), \qquad |3^{(0)}\rangle = \frac{1}{\sqrt{2(1-b_z)}} \begin{bmatrix} 0 \\ 0 \\ b_x \\ 1-b_z \end{bmatrix},$$

$$\omega_4^{(0)} = \frac{1}{2}(-\omega_\mu - \omega_\mathrm{F}), \quad \text{and} \qquad |4^{(0)}\rangle = \frac{1}{\sqrt{2(1+b_z)}} \begin{bmatrix} 0 \\ 0 \\ -b_x \\ 1+b_z \end{bmatrix}.$$

The dipole-dipole term can now be included, by considering this as a perturbation on these Zeeman states. The dipole–dipole Hamiltonian $\mathcal{H}_\mathrm{dip}$ is

$$\frac{\mathcal{H}_\mathrm{dip}}{\hbar} = \frac{\omega_\mathrm{D}}{4} \begin{pmatrix} \frac{1}{2} - 3\cos^2\theta & -\frac{3}{2}\sin 2\theta e^{-i\phi} & -\frac{3}{2}\sin 2\theta e^{-i\phi} & -3\sin^2\theta e^{-2i\phi} \\ -\frac{3}{2}\sin 2\theta e^{i\phi} & -\frac{1}{2} + 3\cos^2\theta & \frac{1}{2} - 3\sin^2\theta & \frac{3}{2}\sin 2\theta e^{-i\phi} \\ -\frac{3}{2}\sin 2\theta e^{i\phi} & \frac{1}{2} - 3\sin^2\theta & -\frac{1}{2} + 3\cos^2\theta & \frac{3}{2}\sin 2\theta e^{-i\phi} \\ -3\sin^2\theta e^{2i\phi} & \frac{3}{2}\sin 2\theta e^{i\phi} & \frac{3}{2}\sin 2\theta e^{i\phi} & \frac{1}{2} - 3\cos^2\theta \end{pmatrix}, \tag{7.9}$$

where θ and ϕ are the azimuthal and polar angles of the F–μ bond respectively (see Figure 7.7). The first order perturbation of this interaction on the eigen-

values is given by

$$\omega_i = \frac{1}{\hbar}\langle i^{(0)}|\mathcal{H}_{\rm dip}|i^{(0)}\rangle. \tag{7.10}$$

Using this, the perturbed eigenvalues (for $\omega_\mu, \omega_{\rm F} \gg \omega_{\rm D}$) are

$$\omega_1 = \frac{1}{2}(\omega_\mu + \omega_{\rm F}) + \frac{\omega_{\rm D}}{8(1-b_z)}\bigg(b_x^2\Big(\frac{1}{2} - 3\cos^2\theta\Big) - 3b_x(1-b_z)\sin 2\theta\cos\phi + (1-b_z)^2\Big(3\cos^2\theta - \frac{1}{2}\Big)\bigg),$$

$$\omega_2 = \frac{1}{2}(\omega_\mu - \omega_{\rm F}) + \frac{\omega_{\rm D}}{8(1+b_z)}\bigg(b_x^2\Big(\frac{1}{2} - 3\cos^2\theta\Big) + 3b_x(1+b_z)\sin 2\theta\cos\phi + (1+b_z)^2\Big(3\cos^2\theta - \frac{1}{2}\Big)\bigg),$$

$$\omega_3 = \frac{1}{2}(\omega_{\rm F} - \omega_\mu) + \frac{\omega_{\rm D}}{8(1-b_z)}\bigg(b_x^2\Big(3\cos^2\theta - \frac{1}{2}\Big) + 3b_x(1-b_z)\sin 2\theta\cos\phi + (1-b_z)^2\Big(\frac{1}{2} - 3\cos^2\theta\Big)\bigg),$$

and

$$\omega_4 = \frac{1}{2}(-\omega_\mu - \omega_{\rm F}) + \frac{\omega_{\rm D}}{8(1+b_z)}\bigg(b_x^2\Big(3\cos^2\theta - \frac{1}{2}\Big) - 3b_x(1+b_z)\sin 2\theta\cos\phi + (1+b_z)^2\Big(\frac{1}{2} - 3\cos^2\theta\Big)\bigg).$$

The geometry of this muon state gives $b_x = 0.9257$ and $b_z = -0.3782$, and also $\cos\theta = 0.9175$ and $\cos\phi = -0.9362$. Therefore the muon precession frequencies are

$$\omega_\mu^\pm = \gamma_\mu B_\mu \pm \delta_\mu$$
$$\omega_{\rm F}^\pm = \gamma_{\rm F} B_{\rm F} \pm \delta_{\rm F}$$
$$\omega_{\rm F} \pm \omega_\mu = \gamma_{\rm F} B_{\rm F} \pm \gamma_\mu B_\mu,$$

with $\delta_\mu = \delta_{\rm F} = 0.8574\omega_{\rm D}$ ($\omega_{\rm D} = \frac{\mu_0\gamma_\mu\gamma_{\rm F}}{4\pi\hbar|\boldsymbol{r}|^3} = 1.472$ Mrad s^{-1} from the ISIS data for this geometry). Note that δ_μ and $\delta_{\rm F}$ vary as a function of the geometry of the system, and will change for different magnetic structures and muon sites.

Therefore, we propose that the origin of the second oscillation is due to the effect of the nearest-neighbour fluorine nucleus precessing in its own local magnetic field resulting from the ordered Ag^{2+} electronic moments, which then affects the state of

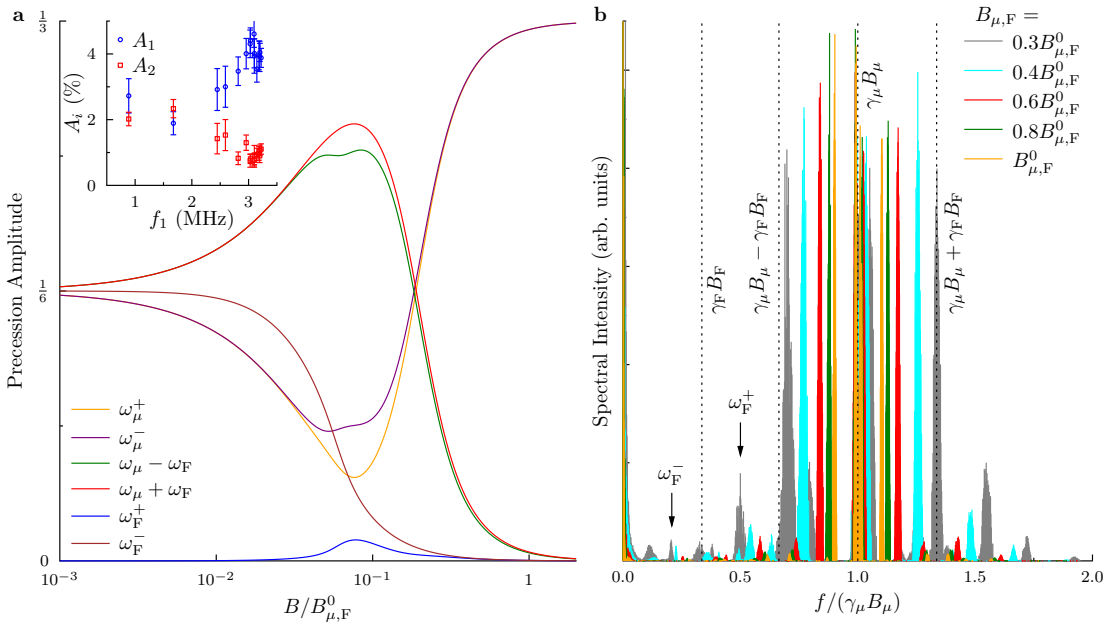


Figure 7.8: F–μ states in a magnetic field. **a** shows how the amplitudes of the components of the muon precession signal vary as the field on the muon and fluorine sites are scaled by a factor of $B/B^0_{\mu,F}$ (the key shows the precession frequencies as $B\to\infty$). The inset shows how the amplitudes A_1 and A_2 of the two measured components vary with the muon precession frequency, showing how at low fields A_1 and A_2 become closer in value, in support of this model. **b** shows the Fourier transform of the system of the muon coupled to its nearest- and next-nearest neighbour spins, for the field at the muon and fluorine sites scaled by various amounts, as shown in the legend.

the muon. This can be pictured by considering both the muon and fluorine to be classical dipoles in a magnetic field. The fluorine and muon both undergo Larmor precession in the field produced by the ordered Ag^{2+} moments, but the dipole-dipole interaction between them creates a field at the muon site that depends on the orientation of the nuclear spin of the fluorine with respect to the local field direction at the fluorine site. The field at the nearest-neighbour fluorine site (assuming the magnetic structure of $KAgF_3$ described above) is calculated as 266.9 Gauss, which is slightly larger than that of the muon (235.1 Gauss), but points in a different direction.

The way in which the amplitudes of the muon precession components vary with magnetic field strength is plotted[9] in Figure 7.8**a**, scaling the field at the muon and fluorine sites by various amounts. This shows that, when the fields at the muon

[9]It is possible to obtain an analytic expression for the amplitudes as well as the frequencies using perturbation theory, but this would only be able to approximate the large B regime.

and fluorine sites are very large, the only precession frequencies observable are due to the muon precessing at its Larmor frequency ("normal" μSR experiments measure far out into this limit, which explains why this effect does not usually need to be considered). However, for the relatively small fields seen in $KAgF_3$, the figure shows that the $\omega_F^{\pm}$ terms increase as the magnetic fields decrease, which occurs when the temperature approaches the transition.

The inset to Figure 7.8**a** shows how the amplitudes of the two components A_1 and A_2 vary with the precession frequency f_1. This shows a clear trend of A_1 decreasing as A_2 increases, which is consistent with this model, despite the effect being more pronounced in the data as one would expect from the theory. Expanding this model to consider also the next-nearest neighbour interactions, the amplitudes of these oscillations change slightly, as shown in Figure 7.8**b**. This shows the Fourier components of the expected muon polarisation, showing peaks at around most of the frequencies of the F–μ case, broadened out by the next-nearest neighbour dipole-dipole interactions (the peaks at the frequencies $\omega_\mu \pm \omega_F$ appear to be missing, showing that the dipole-dipole interaction between the muon and the next-nearest neighbour nuclei is very strong). Decreasing the field further, it can be seen that peaks at ω_F^+ and ω_F^- start to emerge, the latter of which has the larger amplitude, and has a frequency just under half of $\gamma_\mu B_\mu$, consistent with the $f_1 : f_2$ ratio found previously.

7.5 Conclusion

This chapter has applied the methods developed in the previous chapters to locate the muon site in the antiferromagnetic material $KAgF_3$, from which it was possible to measure very accurately the electronic moment of the Ag^{2+} ions, using a mixture of data both above and below the ordering temperature. The μSR data also provides evidence of the nature of the interactions between the ions being Ising-like, however more data are required to conclusively distinguish this from other

possible interactions (the critical exponents for a 3D Heisenberg model is 0.367, but for a 3D Ising model[10] this is 0.326).

Additionally, the way in which the dipole-dipole coupling between the muon and the nearest-neighbour fluorine nucleus affects the μSR spectrum in the ordered phase is a fascinating phenomenon which has not been discovered before. Although there were not enough decay statistics nor temperature points measured in the PSI dataset to show this conclusively, it is a highly plausible hypothesis that may also apply to other materials, including other fluoroargentates[11] and molecular magnets.

[10]The Ising model has spins interacting with Hamiltonian $\mathcal{H} = -J\sum_{\langle i,j\rangle}\sigma_i\sigma_j - h\sum_i \sigma_i$ for nearest-neighbour spins i and j, constrained such that $\sigma \in \{+1, -1\}$ only [107]. J is the exchange coupling constant, and h is a parameter which creates anisotropy, possibly due to an applied magnetic field.

[11]The compound Cs_2AgF_4, measured with μSR in 2007 [76], also showed two precession frequencies which were attributed to two separate muon sites. It is possible that the two frequencies can be accounted for with this method.

8
Conclusion

This thesis has shown that the entanglement between a muon in a fluoride sample and its surroundings produces a muon polarisation which can be used to identify the muon site in the material. By starting with simple cubic compounds where the muon site has been known for many years, it was possible to uncover that the perceived relaxation of the μSR signal in these compounds was due to the muon interacting with all the other nuclei, causing its quantum information to decohere away. Once techniques were developed which allowed for the quantification of this decohering effect, it was possible to apply these techniques to compounds with more complicated crystal structures, allowing for the identification of muon sites, muon-induced distortions and Frenkel defects.

The work in this thesis can be most readily applied to the study of magnetic materials with μSR. Chapter 6 identified the muon sites of the ions $[PF_6]^-$ and $[BF_4]^-$ in the simple analogues KPF_6 and KBF_4, which were slightly different to the sites favoured by DFT+μ. This can be directly applied to the study of molecular magnets, as these polyatomic ions are very often found in these materials. Additionally, the work following this in Chapter 7 identified the muon site in an antiferromagnetically ordered material containing fluorine, and hypothesised that the two muon precession frequencies observed in the magnetic phase were due to fluorine precession, rather than the usual interpretation of multiple precession frequencies

corresponding to different muon sites. Despite this, it was not possible to *conclusively* determine this as the source – for this, it is necessary to measure more decay statistics and temperatures to be able to track the precession in more detail. One would also expect to see this phenomenon in other fluoride samples where the magnetic field at the muon site is of a similar order of magnitude, for example in Cs_2AgF_4.

By studying the muon site in the various model systems in this thesis, it is possible to qualitatively identify some patterns which appear to emerge. One of the most crucial ones is that the muon prefers to avoid being in the vicinity of cations whenever possible – for example in KPF_6 and KBF_4, the muon never forms states between fluorides on the same molecular ion, in its attempt to avoid being too close to their central atoms which have had their electrons slightly withdrawn by their surrounding fluorines (hence becoming slightly positively charged). Additionally, it appears that in all the compounds studied which have fluorines occupying different Wyckoff sites (all except CaF_2, NaF and KPF_6), the muon seems to have a preference of forming F–μ–F states between two fluorides in different sites. While this could just be due to nothing more than coincidence, there could possibly be a deeper reason behind this which may emerge once more fluorides are investigated.

Future work

Some ideas for future work are:

- **Muon sites in molecular magnets.** Chapter 6 has focused on locating the muon site in two fluorine containing molecular anions often found in molecular magnets, but there is still some uncertainty as to what extent the muon sites found in these compounds are transferable to other compounds[1]. In particular, what if the $[BF_4]^-$ or $[PF_6]^-$ ions are separated by a long distance? Would the muon still bridge between two of these, or would it be forced to form an intra-polyhedron state?

[1] It is therefore perhaps unfortunate that inter-polyhedra muon sites are preferred over intra-polyhedra!

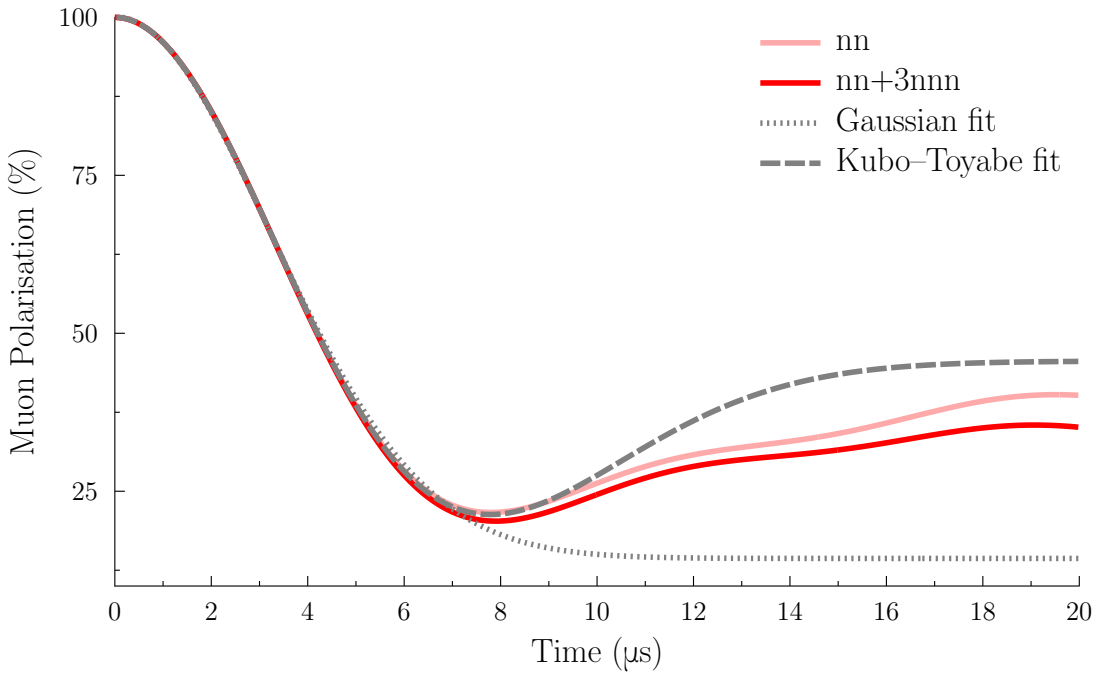


Figure 8.1: Muon–iodine entanglement in KI. The muon polarisation for KI is plotted for a muon interacting with its nearest-neighbour iodine nuclei (pink line) and three of its next-nearest-neighbours (red line) (calculating this for all four nnn nuclei results in matrices of size 93312×93312, which is very computationally challenging). The grey lines show the fits to these lines with a Gaussian and Kubo–Toyabe oscillation, showing the effect the muon–iodine entanglement has on the polarisation.

- **Measuring muon entanglement in *all* halogens.** This thesis has only focused on muon states in fluorides, but it is certainly possible that the muon states in compounds containing other halogen ions are similar to these. In particular, iodine has nuclear spin $I = \frac{5}{2}$, with moment $2.81\mu_N$, and is still fairly electronegative (according to Pauling's scale, fluorine has electronegativity 4.0 and iodine 2.5 [131]). Potassium iodide (KI) has the same structure as NaF and would therefore be an ideal test material to see whether analogous "I–μ–I" states form. Preliminary calculations of the muon polarisation in this compound in Figure 8.1 show the deviation from the Kubo–Toyabe behaviour (which one would obtain if the iodine spins were randomly oriented), assuming a μ–I distance of 1.93 Å which was estimated with DFT+μ. This idea is currently being actively investigated.

- **Understanding the role of temperature in muon entangled states.** The fitting results for KPF_6 in Table 6.1 and the variation of the distance between the muon and nearest-neighbour fluorines in Figure 7.6 for $KAgF_3$ suggests that the muon site varies slightly with temperature. However, this is still uncertain, as muon diffusion would also affect the data in a similar way, which has not been accurately modelled in systems like these before. Being able to disentangle[2] the effects of thermal expansion and muon diffusion would allow one to be able to explain these effects in greater detail, giving a deeper insight into the nature of muon sites and would certainly inform the analysis of many other compounds.

- **Understanding organic F–μ–F states.** As the electronegativity of carbon is relatively similar to that of fluorine, in organic fluorides the C–F bonds are much more covalent in character. This means that these complexes rarely accept hydrogen bonds [157, 158], which will have consequences for the formation of F–μ–F states. We have measured the material PERFECTA [159] with μSR in 2020, which showed a distinctive oscillation at 4 K (as shown in Figure 8.2), but it has not been possible to locate a muon site which can explain this. It is possible that muon dynamics are the reason for this unusual shape, despite the temperature being a lot lower than the usual temperatures one would expect to observe muon diffusion (but note that the oscillations in this F–μ–F state have a frequency about half that of the ionic fluoride F–μ–F states measured in the previous chapters, suggesting a longer – and therefore possibly weaker – F–μ bond). Organic compounds would be an ideal test for understanding the role of temperature, as the effect of temperature on muon entangled states is significant in these compounds [70, 74, 160]. In addition, it may be possible to use *negative* muons to study these, as some will become implanted in a low 1s muonic ground state in the carbon atom (and are therefore unlikely to diffuse), forming F–μ–F states. This idea, originating from G. J. W. Gill, is also being actively investigated by the Oxford group.

[2] ☺

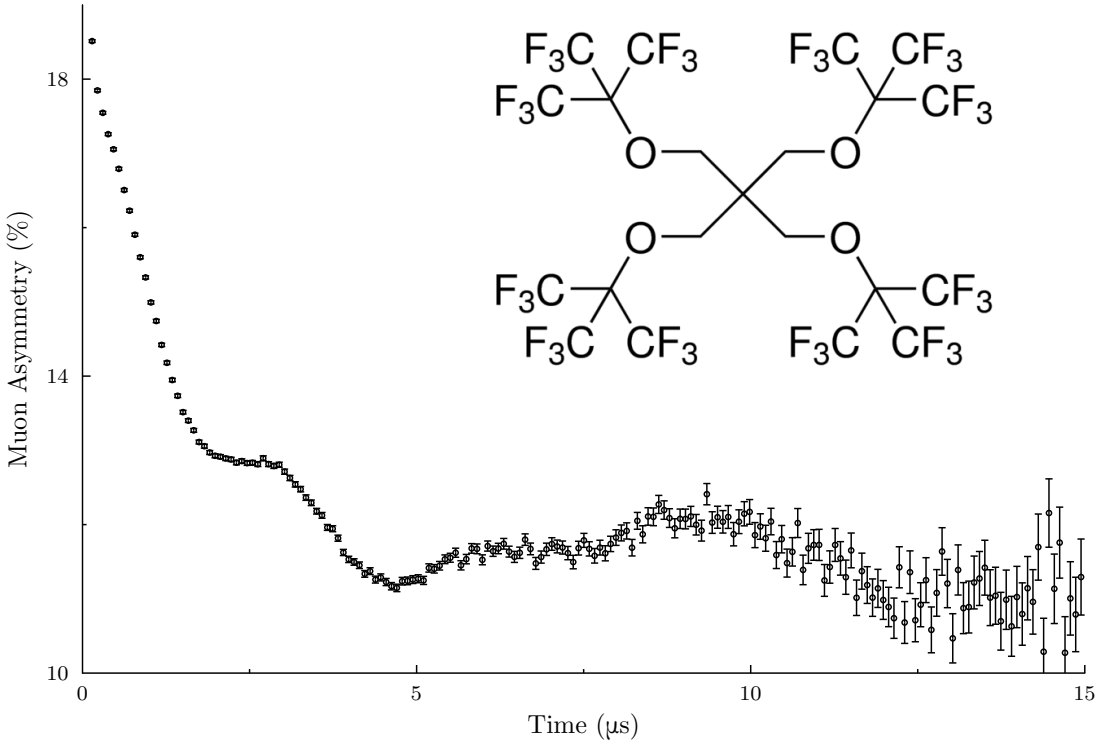


Figure 8.2: PERFECTA μSR data. The data obtained at 4 K with the MuSR spectrometer at ISIS is shown, alongside the chemical structure in the inset (note that the hydrogen atoms are not shown for clarity)

Appendices

A

Classical Derivation of Muon Precession in a Magnetic Field

The time dependence of the muon polarisation in a magnetic field can be calculated classically in addition to quantum mechanically: consider a spin-polarised muon which has moment $\boldsymbol{\mu}$ in a magnetic field $\boldsymbol{B}$, and we define the coordinate system so that $\boldsymbol{B} = B\hat{\boldsymbol{z}}$, with the muon initially polarised in the xz plane. We also define the angles θ and ϕ to be the polar and azimuthal angles of the muon magnetic moment respectively, see Figure A.1, and $\phi(t = 0) = 0$. The magnetic field creates a torque $\boldsymbol{\tau} = \boldsymbol{\mu} \times \boldsymbol{B}$ on the muon which is perpendicular to the direction of its moment, which is equal to the rate of change of angular momentum, so

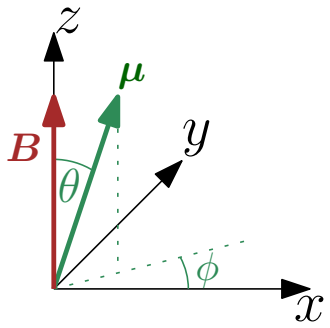


Figure A.1: Coordinate system used for the derivation of muon precession in a magnetic field.

$$\frac{\mathrm{d}\boldsymbol{L}}{\mathrm{d}t} = \frac{1}{\gamma}\frac{\mathrm{d}\boldsymbol{\mu}}{\mathrm{d}t} = \boldsymbol{\mu} \times \boldsymbol{B}, \tag{A.1}$$

where γ is the gyromagnetic ratio of the muon. If we now substitute the muon magnetic moment in Cartesian coordinates, we get

$$\frac{\mathrm{d}\boldsymbol{\mu}}{\mathrm{d}t} = \gamma\mu \begin{bmatrix} \sin\theta\cos\phi \\ \sin\theta\sin\phi \\ \cos\theta \end{bmatrix} \times \begin{bmatrix} 0 \\ 0 \\ B \end{bmatrix} = \gamma\mu B \begin{bmatrix} \sin\theta\sin\phi \\ -\sin\theta\cos\phi \\ 0 \end{bmatrix} \tag{A.2}$$

$$= \begin{bmatrix} \dot{\mu}\sin\theta\cos\phi + \dot{\theta}\mu\cos\theta\cos\phi - \dot{\phi}\mu\sin\theta\sin\phi \\ \dot{\mu}\sin\theta\sin\phi + \dot{\theta}\mu\cos\theta\sin\phi + \dot{\phi}\mu\sin\theta\cos\phi \\ \dot{\mu}\cos\theta - \dot{\theta}\mu\sin\theta \end{bmatrix}, \tag{A.3}$$

which, by comparing initially the $\hat{\boldsymbol{z}}$ term, we get

$$\dot{\mu}\cos\theta = \dot{\theta}\mu\sin\theta. \tag{A.4}$$

As μ is a property of the muon due to its spin, it is constant with time so $\dot{\mu} = 0$. This then means that $\dot{\theta} = 0$[1], and then the $\hat{\mathbf{x}}$ and $\hat{\mathbf{y}}$ equations collapse to

$$-\dot{\phi}\mu\sin\theta\sin\phi = \gamma\mu B\sin\theta\sin\phi \tag{A.5}$$

$$-\dot{\phi}\mu\sin\theta\cos\phi = \gamma\mu B\sin\theta\cos\phi, \tag{A.6}$$

and so $\phi(t) = -\gamma Bt$, i.e the muon precesses in the plane perpendicular to the magnetic field.

In μSR the muon polarisation $P_\mu(t)$ is measured, which can be obtained by projecting $\hat{\boldsymbol{\mu}}(t)$ along the direction of the muon's initial moment direction, $\hat{\boldsymbol{\mu}}(0)$ (due to the geometry of the instrument), so

$$P_\mu(t) = \hat{\boldsymbol{\mu}}(t)\cdot\hat{\boldsymbol{\mu}}(0) \tag{A.7}$$

$$= \begin{bmatrix} \sin\theta\cos -\gamma Bt \\ \sin\theta\sin -\gamma Bt \\ \cos\theta \end{bmatrix} \cdot \begin{bmatrix} \sin\theta \\ 0 \\ \cos\theta \end{bmatrix} \tag{A.8}$$

$$= \sin^2\theta\cos\gamma Bt + \cos^2\theta. \tag{A.9}$$

By substituting $\theta = 0$ and $\theta = \frac{\pi}{2}$ for a muon in a longitudinal and transverse field respectively, one can see that the muon polarisation is exactly the same as that derived using quantum mechanics in Chapter 2.2.

[1] At this stage, it looks like $\theta = \pi$ is also a valid solution which would allow $\dot{\theta} \neq 0$, but on inserting this in to the equations for $\hat{\mathbf{x}}$ and $\hat{\mathbf{y}}$, it can be shown that this still must lead to $\dot{\theta} = 0$.

B

Derivation of the Muon Polarisation of a Linear F–μ–F State

In order to calculate the muon polarisation for an isolated linear F–μ–F system (as first calculated by J. H. Brewer et al. [67]), we start with Equation (2.26), that is,

$$P_\mu^{\text{avg}}(t) = \frac{1}{3}\Big(P_\mu^x(t) + P_\mu^y(t) + P_\mu^z(t)\Big). \tag{2.26}$$

Defining our coordinate system such that the $\hat{\boldsymbol{z}}$ direction is parallel to the μ–F bond and $\hat{\boldsymbol{x}}$ and $\hat{\boldsymbol{y}}$ are perpendicular, we find that both the $\hat{\boldsymbol{x}}$ and $\hat{\boldsymbol{y}}$ directions are equivalent and will hence produce the same muon polarisation. Therefore, for a muon coupled with two ^{19}F nuclei with $I = \frac{1}{2}$, the polarisation can be calculated as

$$P_\mu^{\text{avg}}(t) = \frac{1}{3}\cdot\frac{1}{8}\Big(2\cdot\text{Tr}[\sigma_\mu^x(0)\sigma_\mu^x(t)] + \text{Tr}[\sigma_\mu^z(0)\sigma_\mu^z(t)]\Big). \tag{B.1}$$

Time evolving the muon spin measurement operators in the Heisenberg picture,

$$\sigma_\mu^\sigma(t) = e^{i\mathcal{H}t}\sigma_\mu^\sigma(0)e^{-i\mathcal{H}t},$$

and diagonalising the Hamiltonian into its eigenkets $|\alpha\rangle$ and corresponding eigenvalues ω_α, we obtain

$$\begin{aligned} P_\mu^{\text{avg}}(t) = \frac{1}{24}\Big(&2\sum_{\alpha\beta\gamma}\langle\alpha|\sigma_x^\mu(0)|\beta\rangle e^{i\omega_\beta t}\langle\beta|\sigma_x^\mu(0)|\gamma\rangle e^{-i\omega_\gamma t}\langle\gamma|\alpha\rangle \\ &+\sum_{\alpha\beta\gamma}\langle\alpha|\sigma_z^\mu(0)|\beta\rangle e^{i\omega_\beta t}\langle\beta|\sigma_z^\mu(0)|\gamma\rangle e^{-i\omega_\gamma t}\langle\gamma|\alpha\rangle\Big). \end{aligned} \tag{B.2}$$

Noting $\langle\beta|\alpha\rangle = \delta_{\alpha,\beta}$, and rearranging gives

$$P_\mu^{\text{avg}}(t) = \frac{1}{24}\Big(2\sum_{\alpha\beta}\Big|\langle\alpha|\sigma_x^\mu(0)|\beta\rangle\Big|^2 e^{i(\omega_\beta-\omega_\alpha)t} + \sum_{\alpha\beta}\Big|\langle\alpha|\sigma_z^\mu(0)|\beta\rangle\Big|^2 e^{i(\omega_\beta-\omega_\alpha)t}\Big). \quad \text{(B.3)}$$

Splitting the sums into $\alpha = \beta$ and $\alpha < \beta$, we obtain

$$\begin{aligned} P_\mu^{\text{avg}}(t) = \frac{1}{24}\Big[2\Big(\sum_\alpha\Big|\langle\alpha|\sigma_x^\mu(0)|\alpha\rangle\Big|^2 + \sum_{\alpha<\beta}\Big|\langle\alpha|\sigma_x^\mu(0)|\beta\rangle\Big|^2(e^{i(\omega_\beta-\omega_\alpha)t} + e^{-i(\omega_\beta-\omega_\alpha)t})\Big) \\ + \sum_\alpha\Big|\langle\alpha|\sigma_z^\mu(0)|\alpha\rangle\Big|^2 + \sum_{\alpha<\beta}\Big|\langle\alpha|\sigma_z^\mu(0)|\beta\rangle\Big|^2(e^{i(\omega_\beta-\omega_\alpha)t} + e^{-i(\omega_\beta-\omega_\alpha)t})\Big)\Big], \end{aligned} \quad \text{(B.4)}$$

and hence we get the general expression

$$\begin{aligned} P_\mu^{\text{avg}}(t) = \frac{1}{24}\Big[\sum_\alpha\Big(2\Big|\langle\alpha|\sigma_x^\mu(0)|\alpha\rangle\Big|^2 + 2\Big|\langle\alpha|\sigma_z^\mu(0)|\alpha\rangle\Big|^2\Big) \\ + 2\sum_{\alpha<\beta}\Big(2\Big|\langle\alpha|\sigma_x^\mu(0)|\beta\rangle\Big|^2 + \Big|\langle\alpha|\sigma_z^\mu(0)|\beta\rangle\Big|^2\Big)\cos(\omega_\beta-\omega_\alpha)t\Big]. \end{aligned} \quad \text{(B.5)}$$

The Hamiltonian in this case is the magnetic dipole-dipole Hamiltonian, Equation (3.8). Considering only μ–F interactions, and assuming the muon is exactly at the centre between the two fluorines, this becomes

$$\begin{aligned} \mathcal{H} &= \frac{\mu_0\gamma_\mu\gamma_{\text{F}}}{4\pi|\boldsymbol{r}_{\mu\text{F}}|^3}\Big(\boldsymbol{s}_\mu\cdot\boldsymbol{I}_1 - 3(\boldsymbol{s}_\mu\cdot\hat{\boldsymbol{r}}_{\mu\text{F}})(\boldsymbol{I}_1\cdot\hat{\boldsymbol{r}}_{\mu\text{F}}) + \boldsymbol{s}_\mu\cdot\boldsymbol{I}_2 - 3(\boldsymbol{s}_\mu\cdot\hat{\boldsymbol{r}}_{\mu\text{F}})(\boldsymbol{I}_2\cdot\hat{\boldsymbol{r}}_{\mu\text{F}})\Big) \\ &= \frac{\mu_0\gamma_\mu\gamma_{\text{F}}}{4\pi|\boldsymbol{r}_{\mu\text{F}}|^3}\Big(\boldsymbol{s}_\mu\cdot\boldsymbol{I}_{\text{T}} - 3(\boldsymbol{s}_\mu\cdot\hat{\boldsymbol{r}}_{\mu\text{F}})(\boldsymbol{I}_{\text{T}}\cdot\hat{\boldsymbol{r}}_{\mu\text{F}})\Big) \end{aligned} \quad \text{(B.6)}$$

where the symbol $\boldsymbol{I}_{1,2}$ is used to denote the spin of the individual fluorine nuclei, and $\boldsymbol{I}_{\text{T}} = \boldsymbol{I}_1 + \boldsymbol{I}_2$ is used to denote the vector sum of the spins of both.

Working in the basis $|\mu\text{F}_1\text{F}_2\rangle$, the states are as follows (where I use m to denote the magnetic quantum number of the species, and each of the states are ordered to make the states which interact adjacent to each other):

State	$\lvert\mu\mathrm{F}_1\mathrm{F}_2\rangle$ form	m_μ	I_T	m_T
$\lvert 0\rangle$	$\lvert\uparrow\uparrow\uparrow\rangle$	$\frac{1}{2}$	1	1
$\lvert 1\rangle$	$\lvert\uparrow\rangle\otimes(\lvert\uparrow\downarrow\rangle-\lvert\downarrow\uparrow\rangle)/\sqrt{2}$	$\frac{1}{2}$	0	0
$\lvert 2\rangle$	$\lvert\uparrow\downarrow\downarrow\rangle$	$\frac{1}{2}$	1	−1
$\lvert 3\rangle$	$\lvert\downarrow\rangle\otimes(\lvert\uparrow\downarrow\rangle+\lvert\downarrow\uparrow\rangle)/\sqrt{2}$	$-\frac{1}{2}$	1	0
$\lvert 4\rangle$	$\lvert\uparrow\rangle\otimes(\lvert\uparrow\downarrow\rangle+\lvert\downarrow\uparrow\rangle)/\sqrt{2}$	$\frac{1}{2}$	1	0
$\lvert 5\rangle$	$\lvert\downarrow\uparrow\uparrow\rangle$	$-\frac{1}{2}$	1	1
$\lvert 6\rangle$	$\lvert\downarrow\rangle\otimes(\lvert\uparrow\downarrow\rangle-\lvert\downarrow\uparrow\rangle)/\sqrt{2}$	$-\frac{1}{2}$	0	0
$\lvert 7\rangle$	$\lvert\downarrow\downarrow\downarrow\rangle$	$-\frac{1}{2}$	1	−1

Placing these states into a matrix with elements $H_{ij} = \langle i|\mathcal{H}|j\rangle$, results in the block diagonal matrix

$$\mathcal{H} = \frac{\mu_0\gamma_\mu\gamma_\mathrm{F}}{2\cdot 4\pi|\boldsymbol{r}_{\mu\mathrm{F}}|^3}\begin{bmatrix} -2 & & & & & & & \\ & 0 & & & & & & \\ & & 2 & \sqrt{2} & & & & \\ & & \sqrt{2} & 0 & & & & \\ & & & & 0 & \sqrt{2} & & \\ & & & & \sqrt{2} & 2 & & \\ & & & & & & 0 & \\ & & & & & & & -2 \end{bmatrix}, \tag{B.7}$$

which is easy to diagonalise into a matrix of eigenvalues $\boldsymbol{\Omega}$,

$$\boldsymbol{\Omega} = \frac{\mu_0\gamma_\mu\gamma_\mathrm{F}}{2\cdot 4\pi|\boldsymbol{r}_{\mu\mathrm{F}}|^3}\mathrm{diag}\{-2, 0, 1+\sqrt{3}, 1-\sqrt{3}, 1+\sqrt{3}, 1-\sqrt{3}, 0, -2\}, \tag{B.8}$$

where diag{} creates a diagonal matrix with its arguments as the elements, and corresponding orthonormal eigenstates $\mathbf{S}$,

$$\mathbf{S} = \begin{array}{c} \begin{matrix} |\mathrm{I}\rangle & |\mathrm{II}\rangle & |\mathrm{III}\rangle & |\mathrm{IV}\rangle & |\mathrm{V}\rangle & |\mathrm{VI}\rangle & |\mathrm{VII}\rangle & |\mathrm{VIII}\rangle \end{matrix} \\ \begin{bmatrix} 1 & 0 & 0 & 0 & 0 & 0 & 0 & 0 \\ 0 & 1 & 0 & 0 & 0 & 0 & 0 & 0 \\ 0 & 0 & \frac{\sqrt{2}}{\sqrt{6-2\sqrt{3}}} & \frac{\sqrt{2}}{\sqrt{6+2\sqrt{3}}} & 0 & 0 & 0 & 0 \\ 0 & 0 & \frac{-1+\sqrt{3}}{\sqrt{6-2\sqrt{3}}} & \frac{1-\sqrt{3}}{\sqrt{6+2\sqrt{3}}} & 0 & 0 & 0 & 0 \\ 0 & 0 & 0 & 0 & \frac{-1+\sqrt{3}}{\sqrt{6-2\sqrt{3}}} & \frac{-1-\sqrt{3}}{\sqrt{6+2\sqrt{3}}} & 0 & 0 \\ 0 & 0 & 0 & 0 & \frac{\sqrt{2}}{\sqrt{6-2\sqrt{3}}} & \frac{\sqrt{2}}{\sqrt{6+2\sqrt{3}}} & 0 & 0 \\ 0 & 0 & 0 & 0 & 0 & 0 & 1 & 0 \\ 0 & 0 & 0 & 0 & 0 & 0 & 0 & 1 \end{bmatrix} \end{array}. \tag{B.9}$$

By inspecting the matrix in Equation (B.7) and comparing it to the quantum numbers of the states, one can deduce that the only allowed transitions that lead to oscillations in the μSR asymmetry are where $\Delta m_{\mathrm{T}} + \Delta m_{\mu} = 0$ is satisfied, and also flipping all the spins results in the same transition amplitudes. This means reduced matrices can be constructed by removing the interactions which produce the same oscillations. These are

$$\mathbf{S}_{\mathrm{red}} = \begin{array}{c} \begin{matrix} |\mathrm{I}\rangle & |\mathrm{II}\rangle & |\mathrm{III}\rangle & |\mathrm{IV}\rangle \end{matrix} \\ \begin{bmatrix} 1 & 0 & 0 & 0 \\ 0 & 1 & 0 & 0 \\ 0 & 0 & \frac{\sqrt{2}}{\sqrt{6-2\sqrt{3}}} & \frac{\sqrt{2}}{\sqrt{6+2\sqrt{3}}} \\ 0 & 0 & \frac{-1+\sqrt{3}}{\sqrt{6-2\sqrt{3}}} & \frac{1-\sqrt{3}}{\sqrt{6+2\sqrt{3}}} \end{bmatrix} \end{array}. \tag{B.10}$$

and

$$\mathbf{\Omega}_{\mathrm{red}} = \frac{\mu_0 \gamma_{\mu} \gamma_{\mathrm{F}}}{2 \cdot 4\pi |\boldsymbol{r}_{\mu \mathrm{F}}|^3} \mathrm{diag}\{-2, 0, 1+\sqrt{3}, 1-\sqrt{3}\}. \tag{B.11}$$

The corresponding muon spin measurement operators of this reduced space, $\sigma^x_{\mu,\mathrm{red}}$ and $\sigma^z_{\mu,\mathrm{red}}$ are

$$\sigma^x_{\mu,\mathrm{red}} = \begin{bmatrix} 0 & 0 & 1 & 0 \\ 0 & 1 & 0 & 0 \\ 1 & 0 & 0 & 0 \\ 0 & 0 & 0 & 1 \end{bmatrix}, \tag{B.12}$$

and

$$\sigma^z_{\mu,\mathrm{red}} = \begin{bmatrix} 1 & 0 & 0 & 0 \\ 0 & 1 & 0 & 0 \\ 0 & 0 & 1 & 0 \\ 0 & 0 & 0 & -1 \end{bmatrix}, \tag{B.13}$$

which have been constructed by considering that the effect of the σ^x_{μ} operator on an eigenstate of σ^z_{μ} is to flip the z component of the muon spin, and the effect of σ^z_{μ} on these states is to return the value of the muon spin along z.

Now, following from Equation (B.5), the only non-zero oscillatory amplitudes are

$$\begin{aligned}
\left|\langle \mathrm{III}|\sigma^z_{\mu,\mathrm{red}}|\mathrm{IV}\rangle\right|^2 &= \frac{2}{3} \\
\left|\langle \mathrm{I}|\sigma^x_{\mu,\mathrm{red}}|\mathrm{III}\rangle\right|^2 &= \frac{1}{2}\left(1+\frac{1}{\sqrt{3}}\right) \\
\left|\langle \mathrm{I}|\sigma^x_{\mu,\mathrm{red}}|\mathrm{IV}\rangle\right|^2 &= \frac{1}{2}\left(1-\frac{1}{\sqrt{3}}\right) \\
\left|\langle \mathrm{III}|\sigma^x_{\mu,\mathrm{red}}|\mathrm{IV}\rangle\right|^2 &= \frac{1}{6}.
\end{aligned}$$

Substituting these with the corresponding amplitudes into Equation (B.5), we get

$$\begin{aligned}
P_\mu^{\mathrm{avg}}(t) = c + \frac{1}{24}\cdot 2\cdot 2\cdot \Bigg[& \frac{2}{3}\cos\left(\sqrt{3}\omega_{\mathrm{D}}t\right) + \\
& 2\cdot\left(\frac{1}{2}\left(1-\frac{1}{\sqrt{3}}\right)\cos\left(\frac{3-\sqrt{3}}{2}\omega_{\mathrm{D}}t\right)\right. \\
& \quad + \frac{1}{2}\left(1+\frac{1}{\sqrt{3}}\right)\cos\left(\frac{3+\sqrt{3}}{2}\omega_{\mathrm{D}}t\right) \\
& \quad \left. + \frac{1}{6}\cos\left(\sqrt{3}\omega_{\mathrm{D}}t\right)\right)\Bigg],
\end{aligned} \tag{B.14}$$

where c is a constant (the non-oscillatory term in Equation (B.5)), and $\omega_{\mathrm{D}} = \frac{\mu_0\gamma_\mu\gamma_{\mathrm{F}}}{4\pi|\boldsymbol{r}_{\mu\mathrm{F}}|^3}$. The new factor of 2 at the start of the oscillatory term is due to the symmetry of flipping all the spins in the Hamiltonian leaving it invariant, an artefact of the use of the reduced matrices (hence not explicitly calculating the oscillations for states $|\mathrm{V}\rangle$ to $|\mathrm{VIII}\rangle$). It is possible to calculate the constant c by evaluating the $\langle\alpha|\sigma_\mu|\alpha\rangle$ terms, but an easier way is to use the initial condition $P_\mu^{\mathrm{avg}}(0) = 1$, which leads to $c = \frac{1}{2}$. Therefore, the muon polarisation for an F–μ–F state is

$$\begin{aligned}
P_\mu^{\mathrm{avg}}(t) = \frac{1}{6}\Bigg\{ & 3 + \cos\left(\sqrt{3}\omega_{\mathrm{D}}t\right) + \left(1-\frac{1}{\sqrt{3}}\right)\cos\left[\left(\frac{3-\sqrt{3}}{2}\right)\omega_{\mathrm{D}}t\right] \\
& + \left(1+\frac{1}{\sqrt{3}}\right)\cos\left[\left(\frac{3+\sqrt{3}}{2}\right)\omega_{\mathrm{D}}t\right]\Bigg\},
\end{aligned} \tag{B.15}$$

as given by Equation (3.9).

This method can also be extended to a muon interacting with nuclei with $I > \frac{1}{2}$, by using the Clebsch-Gordan coefficients to join the two nuclei into a single state.

The z component of the polarisation is then[1]

$$P_\mu^z(t) = 1 + \frac{2}{(I_\mathrm{T}+1)^2} \sum_{I=0}^{I=I_\mathrm{T}} \sum_{m=0}^{m=I} \frac{I(I+1) - m(m+1)}{1 + I(I+1) + 3m(m+1)} \cdot \left(\cos\left(\sqrt{1 + I(I+1) + 3m(m+1)}\omega_\mathrm{D} t \right) - 1 \right), \tag{B.16}$$

which has the beautiful property that the polarisation for nuclei with $I > \frac{1}{2}$ can be achieved by just scaling and adding additional terms to the $I = \frac{1}{2}$ ($I_\mathrm{T} = 1$) case, or in other words there exists a recurrence relation for the muon polarisation for increasing I (the derivation of this is beyond the scope of this thesis, but this may be useful in the future if one wishes to investigate the muon precession in e.g. potential I–μ–I states in KI)[2].

[1] This is my favourite formula to come out of my entire D.Phil, and it pains me greatly that it has ended up in an appendix rather than in the meat of the thesis. But, as it never really gets used, here it goes for now.

[2] The derivation of the x case is much more complicated due to $\sigma^x_{\mu,\mathrm{red}}$ being non-diagonal.

C

Magnetic Properties of Nuclear Isotopes

Table C.1 lists all the isotopes of the atoms used in this thesis, with their natural abundance, magnetic moments, and gyromagnetic ratios. (Note that isotopes with spin $I = 0$ are not included as these nuclei will have no contribution to the μSR spectra). Isotopes marked with a † are radioactive.

Species	Isotope	I	$\lvert\mu\rvert/\mu_N$	Gyromag. Ratio (Mrad s^{-1} T^{-1})	Abundance (%)
(μ	–	$\frac{1}{2}$	8.889	$2\pi \times 135.5$	100)
H	^{1}H	$\frac{1}{2}$	2.793	$2\pi \times 42.58$	99.99
	^{2}H	1	0.857	$2\pi \times 6.536$	0.01
B	^{10}B	3	1.801	$2\pi \times 4.575$	19.6
	^{11}B	$\frac{3}{2}$	2.689	$2\pi \times 13.66$	80.4
F	^{19}F	$\frac{1}{2}$	2.627	$2\pi \times 40.06$	100
Na	^{23}Na	$\frac{3}{2}$	2.217	$2\pi \times 11.26$	100
P	^{31}P	$\frac{1}{2}$	1.131	$2\pi \times 17.24$	100
K	^{39}K	$\frac{3}{2}$	0.3915	$2\pi \times 1.986$	93.10
	^{40}K†	4	1.298	$2\pi \times 2.470$	0.01
	^{41}K	$\frac{3}{2}$	0.2149	$2\pi \times 1.090$	6.88
Ca	^{43}Ca	$\frac{7}{2}$	1.317	$2\pi \times 2.865$	0.145
Y	^{89}Y	$\frac{1}{2}$	0.1373	$2\pi \times 2.086$	100
Ag	^{107}Ag	$\frac{1}{2}$	0.1135	$2\pi \times 1.723$	51.8
	^{109}Ag	$\frac{1}{2}$	0.1305	$2\pi \times 1.981$	48.2
I	^{127}I	$\frac{5}{2}$	2.809	$2\pi \times 8.518$	100
Pb	^{207}Pb	$\frac{1}{2}$	0.5843	$2\pi \times 8.907$	100

Table C.1: Isotopes of all magnetic nuclei used in this thesis. Data from [161]

References

[1] É. d. T. de Lacheisserie, D. Gignoux, and M. Schlenker, *Magnetism: I - fundamentals* (Springer, New York, 2002).

[2] M. Faraday, *Experimental researches in electricity*, Phil. Trans. R. Soc. Lond. **122**, 125 (1832).

[3] J. C. Maxwell, *A dynamical theory of the electromagnetic field*, Phil. Trans. R. Soc. Lond. **155**, 459 (1865).

[4] A. Einstein, *Zur Elektrodynamik bewegter Körper [english: On the electrodynamics of moving bodies]*, German, Ann. Phys. **17**, 891 (1905).

[5] A. Wright, *The spinning electron*, Nat. Phys. **4**, S6 (2008).

[6] W. Heisenberg, *Zur Theorie des Ferromagnetismus [english: On the theory of ferromagnetism]*, Z. Angew. Phys. **49**, 619 (1928).

[7] C. V. Topping and S. J. Blundell, *A.C. susceptibility as a probe of low-frequency magnetic dynamcis*, J. Phys.: Condens. Matter **31**, 013001 (2019).

[8] A. T. Boothroyd, *Principles of neutron scattering from condensed matter* (Oxford University Press, Oxford, 2020).

[9] B. Reif, S. E. Ashbrook, L. Emsley, and M. Hong, *Solid-state NMR spectroscopy*, Nat. Rev. Methods Primers **1**, 2 (2021).

[10] J. H. Freed, *Electron spin resonance*, Annu. Rev. Phys. Chem. **23**, 265 (1972).

[11] R. L. Garwin, L. M. Lederman, and M. Weinrich, *Observations of the failure of conservation of parity and charge conjugation in meson decays: the magnetic moment of the free muon*, Phys. Rev. **105**, 1415 (1957).

[12] Y. J. Uemura, G. M. Luke, B. J. Sternlieb, J. H. Brewer, J. F. Carolan, W. N. Hardy, R. Kadono, J. R. Kempton, R. F. Kiefl, S. R. Kreitzman, P. Mulhern, T. M. Riseman, D. L. Williams, B. X. Yang, S. Uchida, H. Takagi, J. Gopalakrishnan, A. W. Sleight, M. A. Subramanian, C. L. Chien, M. Z. Cieplak, G. Xiao, V. Y. Lee, B. W. Statt, C. E. Stronach, W. J. Kossler, and X. H. Yu, *Universal correlations between T_c and $\frac{n_s}{m^*}$ (carrier density over effective mass) in high-T_c cuprate superconductors*, Phys. Rev. Lett. **62**, 2317 (1989).

[13] A. D. Hillier and R. Cywinski, *The classification of superconductors using muon spin rotation*, Appl. Magn. Reson. **13**, 95 (1997).

[14] S. Sanna, G. Allodi, G. Concas, A. D. Hillier, and R. D. Renzi, *Nanoscopic coexistence of magnetism and superconductivity in $YBa_2Cu_3O_{6+x}$ detected by muon spin rotation*, Phys. Rev. Lett. **93**, 207001 (2004).

[15] T. J. Jackson, T. M. Riseman, E. M. Forgan, H. Glückler, T. Prokscha, E. Morenzoni, M. Pleines, C. Niedermayer, G. Schatz, H. Luetkens, and J. Litterst, *Depth-resolved profile of the magnetic field beneath the surface of a superconductor with a few nm resolution*, Phys. Rev. Lett. **84**, 4958 (2000).

[16] N. Nishida, H. Miyatake, D. Shimada, S. Hikami, E. Torikai, K. Nishiyama, and K. Nagamine, *Probing magnetism of high-T_c Superconductor Y-Ba-Cu oxide by positive muons*, Jpn. J. Appl. Phys. **26**, L799 (1987).

[17] N. Nishida, H. Miyatake, D. Shimada, S. Okuma, M. Ishikawa, T. Takabatake, Y. Nakazawa, Y. Kuno, R. Keitel, J. H. Brewer, T. M. Riseman, D. L. Williams, Y. Watanabe, T. Yamazaki, K. Nishiyama, K. Nagamine, E. J. Ansaldo, and E. Torikai, *First observation of an antiferromagnetic phase in the $Y_1Ba_2Cu_3O_x$ system*, Jpn. J. Appl. Phys. **26**, L1856 (1987).

[18] H. Maeter, H. Luetkens, Y. G. Pashkevich, A. Kwadrin, R. Khasanov, A. Amato, A. A. Gusev, K. V. Lamonova, D. A. Chervinskii, R. Klingeler, C. Hess, G. Behr, B. Büchner, and H.-H. Klauss, *Interplay of rare earth and iron magnetism in RFeAsO (R=La, Ce, Pr, and Sm): muon-spin relaxation study and symmetry analysis*, Phys. Rev. B **80**, 094524 (2009).

[19] D. E. Murnick, A. T. Fiory, and W. J. Kossler, *Muon-spin depolarization in spin-glasses*, Phys. Rev. Lett. **36**, 100 (1976).

[20] F. Lang, P. J. Baker, A. A. Haghighirad, Y. Li, D. Prabhakaran, R. Valentí, and S. J. Blundell, *Unconventional magnetism on a honeycomb lattice in α-$RuCl_3$ studied by muon spin rotation*, Phys. Rev. B **94**, 020407 (2016).

[21] J. Sugiyama, *Study on hydrogen storage materials*, J. Phys. Soc. Jpn. **85**, 091012 (2016).

[22] M. Aramini, M. Gaboardi, G. Vlahopoulou, D. Pontiroli, C. Cavallari, C. Milanese, and M. Riccò, *Muon spin relaxation reveals the hydrogen storage mechanism in light alkali metal fullerides*, Carbon **67**, 92 (2014).

[23] J. Sugiyama, I. Umegaki, M. Matsumoto, K. Miwa, H. Nozaki, Y. Higuchi, T. Noritake, O. K. Forslund, M. Månsson, S. P. Cottrell, A. Koda, E. J. Ansaldo, and J. H. Brewer, *Desorption reaction in MgH_2 studied with in situ μ^+SR*, Sustainable Energy Fuels **3**, 956 (2019).

[24] S. F. J. Cox, *Implanted muon studies in condensed matter science*, J. Phys. C: Solid State Phys. **20**, 3187 (1987).

[25] S. J. Blundell, *Spin-polarized muons in condensed matter physics*, Contemp. Phys. **40**, 175 (1999).

[26] L. Nuccio, L. Schulz, and A. J. Drew, *Muon spin spectroscopy: magnetism, soft matter and the bridge between the two*, J. Phys. D: Appl. Phys. **47**, 473001 (2014).

[27] A. D. Hillier, S. J. Blundell, I. McKenzie, I. Umegaki, L. Shu, J. A. Wright, T. Prokscha, F. Bert, K. Shimomura, A. Berlie, H. Alberto, and I. Watanabe, *Muon spin spectroscopy*, Nat. Rev. Methods Primers **2**, 4 (2022).

[28] A. Yaouanc and P. de Réotier, *Muon spin rotation, relaxation, and resonance: applications to condensed matter*, International Series of Monographs on Physics (Oxford University Press, 2011).

[29] S. J. Blundell, R. De Renzi, T. Lancaster, and F. L. Pratt, eds., *Introduction to muon spectroscopy* (Oxford University Press, Oxford, 2022).

[30] K. Olive, *Review of particle physics*, Chin. Phys. C **40**, 100001 (2016).

[31] J. Sugiyama, I. Umegaki, H. Nozaki, W. Higemoto, K. Hamada, S. Takeshita, A. Koda, K. Shimomura, K. Ninomiya, and M. K. Kubo, *Nuclear magnetic field in solids detected with negative-muon spin rotation and relaxation*, Phys. Rev. Lett. **121**, 087202 (2018).

[32] A. Hillier, D. Paul, and K. Ishida, *Probing beneath the surface without a scratch – bulk non-destructive elemental analysis using negative muons*, Microchem. J. **125**, 203 (2016).

[33] E. Tiesinga, P. J. Mohr, D. B. Newell, and B. N. Taylor, *CODATA recommended values of the fundamental physical constants: 2018*, Rev. Mod. Phys. **93**, 025010 (2021).

[34] C. Anderson, *Unraveling the particle content of cosmic-rays*, Engineering and Science **46**, 13 (1982).

[35] T. Bowen, *The surface muon beam*, Phys. Today **38**, 22 (1985).

[36] A. D. Hillier, J. S. Lord, K. Ishida, and C. Rogers, *Muons at ISIS*, Phil. Trans. R. Soc. A **377**, 20180064 (2018).

[37] M. Senba, D. J. Arseneau, J. J. Pan, and D. G. Fleming, *Slowing-down times and stopping powers for 2 MeV μ^+ in low-pressure gases*, Phys. Rev. A **74**, 042708 (2006).

[38] L. Michel, *Interaction between four half-spin particles and the decay of the μ-meson*, Proc. Phys. Soc. A **63**, 514 (1950).

[39] P. J. Baker, A. D. Hillier, J. S. Lord, and S. R. Giblin, *MuSR manual*, STFC-ISIS Neutron and Muon Source (Rutherford Appleton Laboratory, Chilton, Oxfordshire, U.K., 2011).

[40] A. Amato and H. Luetkens, *GPS user guide*, Paul Scherrer Institut (Villigen, Aargau, Switzerland, 2015).

[41] K. Blum, *Density matrix theory and applications*, Springer series on atomic, optical and plasma physics (Springer-Verlag, Heidelberg, 2011).

[42] P. Zeeman, *XXXII. On the influence of magnetism on the nature of the light emitted by a substance*, Lond. Edinb. Dublin Philos. Mag. J. Sci. **43**, 226 (1897).

[43] A. J. Kox, *The discovery of the electron: II. the Zeeman effect*, Eur. J. Phys. **18**, 139 (1997).

[44] J. S. Lord, S. P. Cottrell, and W. G. Williams, *Muon spin rotation in strongly coupled systems*, Physica B **289–290**, 495 (2000).

[45] S. J. Blundell, A. J. Steele, T. Lancaster, J. D. Wright, and F. L. Pratt, *A Bayesian approach to magnetic moment determination using μSR*, Physics Procedia **30**, 12th International Conference on Muon Spin Rotation, Relaxation and Resonance (μSR2011), 113 (2012).

[46] P. Hohenberg and W. Kohn, *Inhomogeneous electron gas*, Phys. Rev. **136**, B864 (1964).

[47] R. M. Martin, *Electronic structure: basic theory and practical methods* (Cambridge University Press, 2004).

[48] M. Born, *Zur Quantenmechanik der Stossvergänge [english: On the quantum mechanics of collision processes*, Z. Angew. Phys. **37**, 863 (1926).

[49] W. Kohn, *Nobel lecture: Electronic structure of matter – wave functions and density functionals*, Rev. Mod. Phys. **71**, 1253 (1999).

[50] J. P. Perdew and A. Zunger, *Self-interaction correction to density-functional approximations for many-electron systems*, Phys. Rev. B **23**, 5048 (1981).

[51] J. P. Perdew, J. A. Chevary, S. H. Vosko, K. A. Jackson, M. R. Pederson, D. J. Singh, and C. Fiolhais, *Atoms, molecules, solids, and surfaces: applications of the generalized gradient approximation for exchange and correlation*, Phys. Rev. B **46**, 6671 (1992).

[52] V. Ozoliņš and M. Körling, *Full-potential calculations using the generalized gradient approximation: structural properties of transition metals*, Phys. Rev. B **48**, 18304 (1993).

[53] J. P. Perdew and K. Burke, *Comparison shopping for a gradient-corrected density functional*, Int. J. Quantum Chem. **57**, 309 (1994).

[54] J. P. Perdew, K. Burke, and M. Ernzerhof, *Generalized gradient approximation made simple*, Phys. Rev. Lett. **77**, 3865 (1996).

[55] P. Ziesche, S. Kurth, and J. P. Perdew, *Density functionals from LDA to GGA*, Comput. Mater. Sci. **11**, 122 (1998).

[56] P. Schwerdtfeger, *The pseudopotential approximation in electronic structure theory*, ChemPhysChem **12**, 3143 (2011).

[57] R. P. Feynman, *Forces in molecules*, Phys. Rev. **56**, 340 (1939).

[58] H. Hellmann, *Einfürung in die Quantenchemie [english: Introduction to quantum chemistry]*, German, Reprint. Leipzig und Wien, F. Deuticke, 1937. ([Edwards], Ann Arbor, 1944).

[59] F. Giustino, *Materials modelling using density functional theory: properties and predictions* (Oxford University Press, 2014).

[60] J. S. Möller, D. Ceresoli, T. Lancaster, N. Marzari, and S. J. Blundell, *Quantum states of muons in fluorides*, Phys. Rev. B **87**, 121108(R) (2013).

[61] F. Bernardini, P. Bonfà, S. Massidda, and R. De Renzi, *Ab initio strategy for muon site assignment in wide band gap fluorides*, Phys. Rev. B **87**, 115148 (2013).

[62] D. R. Noakes, *Effect of zero-point motion on μ^+–^{19}F dipole coupling in the $F\mu F^-$ ion in fluoride insulators*, J. Chem. Phys **87**, 3704 (1987).

[63] P. Bonfà, P. Sartori, and R. De Renzi, *Efficient and reliable strategy for identifying muon sites based on the double adiabatic approximation*, J. Phys. Chem. C **119**, 4278 (2015).

[64] P. Bonfà and R. De Renzi, *Toward the computational prediction of muon sites and interaction parameters*, J. Phys. Soc. Jpn. **85**, 091014 (2016).

[65] F. R. Foronda, F. Lang, J. S. Möller, T. Lancaster, A. T. Boothroyd, F. L. Pratt, S. R. Giblin, D. Prabhakaran, and S. J. Blundell, *Anisotropic local modification of crystal field levels in Pr-based pyrochlores: a muon-induced effect modeled using density functional theory*, Phys. Rev. Lett. **114**, 017602 (2015).

[66] J. S. Möller, B. P., D. Ceresoli, F. Bernardini, S. J. Blundell, T. Lancaster, R. De Renzi, N. Marzari, I. Watanabe, S. Sulaiman, and M. I. Mohamed-Ibrahim, *Playing quantum hide-and-seek with the muon: localizing muon stopping sites*, Physica Scripta **88**, 068510 (2013).

[67] J. H. Brewer, S. R. Kreitzman, D. R. Noakes, E. J. Ansaldo, D. R. Harshman, and R. Keitel, *Observation of muon-fluorine "hydrogen bonding" in ionic crystals*, Phys. Rev. B **33**, 7813 (1986).

[68] J. H. Brewer, D. R. Harshman, R. Keitel, S. R. Kreitzman, G. M. Luke, D. R. Noakes, and R. E. Turner, *Thermal hopping of μ^+ between "FμF" centres in NaF*, Hyperfine Interact. **32**, 677 (1986).

[69] D. R. Noakes, E. J. Ansaldo, S. R. Kreitzman, and G. M. Luke, *The $(F\mu F)^-$ ion in solid fluorides*, J. Phys. Chem. Solids **54**, 785 (1993).

[70] K. Nishiyama, S. Nishiyama, and W. Higemoto, *Asymmetric F–μ–F interaction of the muon in polyfluorocarbons*, Physica B **326**, 41 (2003).

[71] R. S. Hayano, Y. J. Uemura, J. Imazato, N. Nishida, T. Yamazaki, and R. Kubo, *Zero-and low-field spin relaxation studied by positive muons*, Phys. Rev. B **20**, 850 (1979).

[72] R. Kadono, J. Imazato, T. Matsuzaki, K. Nishiyama, K. Nagamine, T. Yamazaki, D. Richter, and J.-M. Welter, *Quantum diffusion of positive muons in copper*, Phys. Rev. B **39**, 23 (1989).

[73] G. Allodi and R. D. Renzi, *A numerical method to calculate the muon relaxation function in the presence of diffusion*, Phys. Scr. **89**, 115201 (2014).

[74] F. L. Pratt, S. J. Blundell, I. M. Marshall, T. Lancaster, A. Husmann, C. Steer, W. Hayes, C. Fischmeister, R. E. Martin, and A. B. Holmes, *μSR in polymers*, Physica B **326**, 34 (2003).

[75] T. Lancaster, S. J. Blundell, P. J. Baker, M. L. Brooks, W. Hayes, F. L. Pratt, J. L. Manson, M. M. Conner, and J. A. Schlueter, *Muon-fluorine entangled states in molecular magnets*, Phys. Rev. Lett. **99**, 267601 (2007).

[76] T. Lancaster, S. J. Blundell, P. J. Baker, W. Hayes, S. R. Giblin, S. E. McLain, F. L. Pratt, Z. Salman, E. A. Jacobs, J. F. C. Turner, and T. Barnes, *Intrinsic magnetic order in Cs_2AgF_4 detected by muon-spin relaxation*, Phys. Rev. B **75**, 220408 (2007).

[77] A. Potočnik, A. Zorko, D. Arčon, E. Goreshnik, B. Žemva, R. Blinc, P. Cevc, Z. Trontelj, Z. Jagličič, and J. F. Scott, *Muon spin relaxation in some multiferroic fluorides*, Phys. Rev. B **81**, 214420 (2010).

[78] J. Sugiyama, Y. Ikedo, T. Noritake, O. Ofer, T. Goko, M. Månsson, K. Miwa, E. J. Ansaldo, J. H. Brewer, K. H. Chow, and S.-i. Towata, *Microscopic indicator for thermodynamic stability of hydrogen storage materials provided by positive muon-spin rotation*, Phys. Rev. B **81**, 092103 (2010).

[79] M. Celio and P. Meier, *Spin relaxation of positive muons due to dipolar interactions*, Phys. Rev. B **27**, 1908 (1983).

[80] J. M. Wilkinson and S. J. Blundell, *Information and decoherence in a muon-fluorine coupled system*, Phys. Rev. Lett. **125**, 087201 (2020).

[81] W. H. Zurek, *Decoherence, einselection, and the quantum origins of the classical*, Rev. Mod. Phys. **75**, 715 (2003).

[82] E. Joos and H. D. Zeh, *The emergence of classical properties through interaction with the environment*, Z. Phys. B: Condens. Matter **59**, 223 (1985).

[83] V. Vedral, *The role of relative entropy in quantum information theory*, Rev. Mod. Phys. **74**, 197 (2002).

[84] G. Lindblad, *On the generators of quantum dynamical semigroups*, Commun. Math. Phys. **48**, 119 (1976).

[85] W. P. Aue, E. Bartholdi, and R. R. Ernst, *Two-dimensional spectroscopy. Application to nuclear magnetic resonance*, J. Chem. Phys **64**, 2229 (1976).

[86] W. Hayes, *Crystals with the fluorite structure: electronic, vibrational, and defect properties*, International series of monographs on physics (Clarendon Press, 1974).

[87] S. M. Barnett, *Quantum information* (Oxford University Press, 2009).

[88] E. Noether, *Invariante Variationsprobleme [english: Invariant variation problems*, German, Nachrichten von der Gesellschaft der Wissenschaften zu Göttingen, Mathematisch-Physikalische Klasse **1918**, 235 (1918).

[89] P. Giannozzi, S. Baroni, N. Bonini, M. Calandra, R. Car, C. Cavazzoni, D. Ceresoli, G. L. Chiarotti, M. Cococcioni, I. Dabo, A. D. Corso, S. de Gironcoli, S. Fabris, G. Fratesi, R. Gebauer, U. Gerstmann, C. Gougoussis, A. Kokalj, M. Lazzeri, L. Martin-Samos, N. Marzari, F. Mauri, R. Mazzarello, S. Paolini, A. Pasquarello, L. Paulatto, C. Sbraccia, S. Scandolo, G. Sclauzero, A. P. Seitsonen, A. Smogunov, P. Umari, and R. M. Wentzcovitch, *QUANTUM ESPRESSO: a modular and open-source software project for quantum simulations of materials*, J. Phys. Condens. Matter **21**, 395502 (2009).

[90] E. Roduner and H. Fischer, *The evolution of muon spin polarization in muonic radicals and related species*, Chem. Phys. Lett. **65**, 582 (1979).

[91] M. Celio, *New method to calculate the muon polarization function*, Phys. Rev. Lett. **56**, 2720 (1986).

[92] E. M. Stoudenmire and S. R. White, *Minimally entangled typical thermal state algorithms*, New J. Phys. **12**, 055026 (2010).

[93] J. C. Garcia-Escartin and P. Chamorro-Posada, *A SWAP gate for qudits*, Quantum Inf. Process. **12**, 3625 (2013).

[94] D. R. Harshman and M. Celio, *Positive muons in single crystal sodium fluoride: a simple spin system*, Hyperfine Interact. **32**, 683 (1986).

[95] J. H. Van Vleck, *The dipolar broadening of magnetic resonance lines in crystals*, Phys. Rev. **74**, 1168 (1948).

[96] A. Abragam, *Principles of nuclear magnetism*, 1st ed. (Oxford University Press, Oxford, 1961), p. 370.

[97] R. F. Kiefl, E. Holzschuh, H. Keller, W. Kündig, P. F. Meier, B. D. Patterson, J. W. Schneider, K. W. Blazey, S. L. Rudaz, and A. B. Denison, *Decoupling of muonium in high transverse magnetic fields*, Phys. Rev. Lett. **53**, 90 (1984).

[98] T. Lancaster, F. L. Pratt, S. J. Blundell, I. McKenzie, and H. E. Assender, *Muon–fluorine entanglement in fluoropolymers*, J. Phys.: Condens. Matter **21**, 346004 (2009).

[99] R. Sternheimer, *On nuclear quadrupole moments*, Phys. Rev. **80**, 102 (1950).

[100] H. M. Foley, R. M. Sternheimer, and D. Tycko, *Nuclear quadrupole coupling in polar molecules*, Phys. Rev. **93**, 734 (1954).

[101] R. M. Sternheimer, *Quadrupole shielding and antishielding factors for several atomic ground states*, Phys. Rev. A **6**, 1702 (1972).

[102] E. A. C. Lucken, *Nuclear quadrupole coupling constants,* (Academic P., London; New York, 1969).

[103] T. Prokscha, E. Morenzoni, K. Dieters, F. Foroughi, D. George, R. Kobler, and V. Vrankovic, *A new high-intensity, low-momentum muon beam for the generation of low-energy muons at PSI*, Hyperfine Interact. **159**, 385 (2004).

[104] J. M. Wilkinson, F. L. Pratt, T. Lancaster, P. J. Baker, and S. J. Blundell, *Muon sites in PbF_2 and YF_3: decohering environments and the role of anion Frenkel defects*, Phys. Rev. B **104**, L220409 (2021).

[105] A. Zalkin and D. H. Templeton, *The crystal structures of YF_3 and related compounds*, J. Am. Chem. Soc **64**, 2453 (1953).

[106] K. F. Portella, K. R. Rattmann, G. P. De Souza, C. M. Garcia, M. P. Cantão, and R. Muccillo, *Characterization of $\alpha \leftrightarrow \beta$-$PbF_2$ phase transition by several techniques*, J. Mater. Sci. **35**, 3263 (2000).

[107] S. H. Simon, *The Oxford solid state basics* (Oxford, 2013).

[108] N. W. Ashcroft and N. D. Mermin, *Solid state physics* (Holt, Rinehart and Winston, New York; London, 1976).

[109] A. Möslang, H. Graf, G. Balzer, E. Recknagel, A. Weidinger, T. Wichert, and R. I. Grynszpan, *Muon trapping at monovacancies in iron*, Phys. Rev. B **27**, 2674 (1983).

[110] J. A. Brown, R. H. Heffner, M. Leon, M. E. Schillaci, D. W. Cooke, and W. B. Gauster, *Trapping of positive muons at vacancies in quenched aluminium*, Phys. Rev. Lett. **43**, 1513 (1979).

[111] K. Dorenburg, M. Gladisch, D. Herlach, W. Mansel, H. Metz, H. Orth, G. zu Putlitz, A. Seeger, W. Wahl, and M. Wingand, *Trapping by vacancies and mobility of positive muons in neutron-irridated aluminium*, Z. Physik. B **31**, 165 (1978).

[112] W. R. Panero, L. P. Stixrude, and R. C. Ewing, *First-principles calculation of defect-formation energies in the $Y_2(Ti,Sn,Zr)_2O_7$ pyrochlore*, Phys. Rev. B **70**, 054110 (2004).

[113] V. P. Zhukov and V. M. Za, *First-principles calculations of the electronic structure of fluorite-type crystals and transport properties*, Phys. Solid State **40**, 1827 (1998).

[114] W. Mackrodt, *Defect calculations for ionic materials*, in Computer simulation of solids (Springer-Verlag, Berlin, 1982) Chap. 12, p. 175.

[115] G. A. Samara, *Pressure and temperature dependences of the ionic conductivities of cubic and orthorhombic lead fluoride (PbF_2)*, J. Phys. Chem. Solids **40**, 509 (1979).

[116] T. U. Ito, W. Higemoto, and K. Shimomura, *Negatively charged muonium and related centres in solids*, J. Phys. Soc. Jpn **89**, 051007 (2020).

[117] K. H. Chow, R. F. Kiefl, W. A. MacFarlane, J. W. Schneider, D. W. Cooke, M. Leon, M. Paciotti, T. L. Estle, B. Hitti, R. L. Lichti, S. F. J. Cox, C. Schwab, E. A. Davis, A. Morrobel-Sosa, and L. Zavieh, *Structure of negatively charged muonium in n-type GaAs*, Phys. Rev. B **51**, 14762 (1995).

[118] K. Shimomura, R. Kadono, A. Koda, K. Nishiyama, W. Hugemoto, and T. U. Ito, *μSR study on isolated hydrogen and oxygen vancancy in $SrTiO_3$*, JPS Conf. Proc. **2**, 010308 (2014).

[119] T. U. Ito, A. Koda, K. Shimomura, W. Higemoto, T. Matsuzaki, Y. Kobayashi, and H. Kageyama, *Excited configurations of hydrogen in the $BaTiO_{3-x}H_x$ perovskite lattice associated with hydrogen exchange and transport*, Phys. Rev. B **95**, 020301(R) (2017).

[120] A. J. Churchard, M. Derzsi, Z. Jagličič, A. Remhof, and W. Grochala, *Chemo-switched chromatic, magnetic and structural changes with retention of molecular crystallinity, $Ni(12aneS_4)(BF_4)_2$*, Dalton Trans. **41**, 5172 (2012).

[121] D. L. Reger, C. A. Little, A. L. Rheingold, M. Lam, L. M. Liable-Sands, B. Rhagitan, T. Concolino, A. Mohan, G. J. Long, V. Briois, and F. Grandjean, *A synthetic, structural, magnetic, and spectral study of several $\{Fe[tris(pyrazolyl)methane]_2\}(BF_4)_2$ complexes: observation of an unusual spin-state crossover*, Inorg. Chem. **40**, 1508 (2001).

[122] C.-C. Chiu, M.-C. Cheng, S.-H. Lin, C.-W. Yan, G.-H. Lee, M.-C. Chang, T.-S. Lin, and S.-M. Peng, *Structure and magnetic properties of a novel heteroheptanuclear metal string complex $[Ni_3Ru_2Ni_2(\mu_7\text{-teptra})_4(NCS)_2](PF_6)$*, Dalton Trans. **49**, 6635 (2020).

[123] Y. Yu, Z. Honda, K. Katsumata, T. Ohishi, T. Manabe, and M. Yamashita, *Crystal structure and magnetic properties of the S=1 quasi-one-dimensional compound $Ni([15]aneN_4)N_3(PF_6)$*, Mol. Cryst. Liq. Cryst. **286**, 121 (1996).

[124] A. J. Steele, T. Lancaster, S. J. Blundell, P. J. Baker, F. L. Pratt, C. Baines, M. M. Conner, H. I. Southerland, J. L. Manson, and J. A. Schlueter, *Magnetic order in quasi-two-dimensional molecular magnets investigated with muon-spin relaxation*, Phys. Rev. B **84**, 064412 (2011).

[125] S. R. Giblin, S. P. Cottrell, P. J. C. King, S. Tomlinson, S. J. S. Jago, L. J. Randall, M. J. Roberts, J. Norris, S. Howarth, Q. B. Mutamba, N. J. Rhodes, and F. A. Akeroyd, *Optimising a muon spectrometer for measurements at the ISIS pulsed muon source*, Nucl. Instrum. Methods Phys. Res., Sect. A **751**, 70 (2014).

[126] A. N. Fitch and J. K. Cockcroft, *Low-temperature powder diffraction studies using synchrotron radiation*, Phase Transitions **39**, 161 (1992).

[127] J. K. Cockcroft, *Neutron-scattering studies of order-disorder transitions in hexafluoride salts ABFg*, PhD thesis (University of Oxford, 1985).

[128] A. M. Heyns and C. W. Pistorius, *Vibrational spectra and high-pressure polymorphism of KPF_6*, Spectrochim. Acta, Part A **30**, 99 (1974).

[129] M. Lang, J. Müller, F. Steglich, A. Brüuhl, B. Wolf, and M. Dressel, *Anomalous thermal expansion behavior in $(TMTTF)_2PF_6$ and $(TMTSF)_2PF_6$ around 100 K: indications for a strong spin-phonon interaction?*, J. Phys. IV France **114**, 111 (2004).

[130] G. Brunton, *The crystal structure of KBF_4*, Acta Crystallogr., Sect. B: Struct. Sci **25**, 2161 (1969).

[131] L. Pauling, *The nature of the chemical bond* (Cornell University Press, New York, 1948).

[132] S. J. Grabowski, *Hydrogen bonds with BF_4^- anion as a proton acceptor*, Crystals **10**, 460 (2020).

[133] P. W. Langhoff and R. P. Hurst, *Multipole polarizabilities and shielding factors from Hartree-Fock wave functions*, Phys. Rev. **139**, A1415 (1965).

[134] J. Lahiri and A. Mukherji, *Self-consistent perturbation. II. Calculation of quadrupole polarizability and shielding factor*, Phys. Rev. **141**, 428 (1966).

[135] A. Dalgarno, *Atomic polarizabilities and shielding factors*, Adv. Phys. **11**, 281 (1962).

[136] P. Muller, *Glossary of terms used in physical organic chemistry (IUPAC recommendations 1994)*, Pure & Appl. Chem. **66**, 1077 (1994).

[137] S. J. Grabowski, *π-hole bonds: boron and aluminium Lewis acid centers*, ChemPhysChem **16**, 1470 (2015).

[138] H. Hirao, K. Omoto, and H. Fujimoto, *Lewis acidity of boron trihalides*, J. Phys. Chem. A **103**, 5807 (1999).

[139] J. L. Manson, M. M. Conner, J. A. Schlueter, T. Lancaster, S. J. Blundell, M. L. Brooks, F. L. Pratt, T. Papageorgiou, A. D. Bianchi, J. Wosnitza, and M.-H. Whangbo, *$[Cu(HF_2)(pyz)_2]BF_4$ (pyz = pyrazine): long-range magnetic ordering in a pseudo-cubic coordination polymer comprised of bridging HF_2^- and pyrazine ligands*, Chem. Commun., 4894 (2006).

[140] W. Grochala and R. Hoffmann, *Real and hypothetical intermediate-valence Ag^{II} /Ag^{II} and Ag^{II} /Ag^{I} fluoride systems as potential superconductors*, Angew. Chem. Int. Ed. **40**, 2743 (2001).

[141] W. Grochala, *The theory-driven quest for a novel family of superconductors: fluorides*, J. Mater. Chem. **19**, 6949 (2009).

[142] W. Grochala, *Silverland: the realm of compounds of divalent silver – and why they are interesting*, J. Supercond. Novel Magn. **31**, 737 (2018).

[143] C. Proust and L. Taillefer, *The remarkable underlying ground states of cuprate superconductors*, Annu. Rev. Condens. Matter Phys. **10**, 409 (2019).

[144] X. Zhou, W. Lee, M. Imada, N. Trivedi, P. Phillips, H. Kee, P. Törmä, and M. Eremets, *High-temperature superconductivity*, Nat. Rev. Phys. **3**, 462 (2021).

[145] W. M. Li, J. F. Zhao, L. P. Cao, Z. Hu, Q. Z. Huang, X. C. Wang, Y. Liu, G. Q. Zhao, J. Zhang, Q. Q. Liu, R. Z. Yu, Y. W. Long, H. Wu, H. J. Lin, C. T. Chen, Z. Li, Z. Z. Gong, Z. Guguchia, J. S. Kim, G. R. Stewart, Y. J. Uemura, S. Uchida, and C. Q. Jin, *Superconductivity in a unique type of copper oxide*, PNAS **116**, 12156 (2019).

[146] Y. Zhou, J. Guo, S. Cai, J. Zhao, G. Gu, C. Lin, H. Yan, C. Huang, C. Yang, S. Long, Y. Gong, Y. Li, X. Li, Q. Wu, J. Hu, X. Zhou, T. Xiang, and L. Sun, *Quantum phase transition from superconducting to insulating-like state in a pressurized cuprate superconductor*, Nat. Phys. (2022).

[147] D. Kurzydłowski, Z. Mazej, Z. Jagličić, Y. Filinchuke, and W. Grochala, *Structural transition and unusually strong antiferromagnetic superexchange coupling in perovskite $KAgF_3$*, Chem. Commun. **49**, 6262 (2013).

[148] S. J. Blundell, *Magnetism in condensed matter* (Oxford University Press, 2001).

[149] X. Zhang, G. Zhang, T. Jia, Y. Guo, Z. Zeng, and H. Q. Lin, *$KAgF_3$: Quasi-one-dimensional magnetism in three-dimensional magnetic ion sublattice*, Phys. Lett. A **375**, 2456 (2011).

[150] Z. Mazej, E. Goreshnik, Z. Jagliić, B. Gaweł, W. Łasocha, D. Grzybowska, T. Jaroń, D. Kurzydłowski, P. Malinowski, W. Koźminski, J. Szydłowska, P. Leszczyński, and W. Grochala, *$KAgF_3$, K_2AgF_4 and $K_3Ag_2F_7$: important steps towards a layered antiferromagnetic fluoroargentate(II)*, CrystEngComm **11**, 1702 (2009).

[151] V. I. Anisimov, A. F., and A. I. Lichtenstein, *First-principles calculations of the electronic structure and spectra of strongly correlated systems: the LDA+U method*, J. Phys.: Condens. Matt. **9**, 767 (1997).

[152] S. A. Tolba, K. M. Gameel, B. A. Ali, H. A. Almossalami, and N. K. Allam, *The DFT+U: approaches, accuracy, and applications*, in Density functional calculations, edited by G. Yang (IntechOpen, Rijeka, 2018) Chap. 1.

[153] P. W. Anderson, *Antiferromagnetism. Theory of superexchange interaction*, Phys. Rev. **79**, 350 (1950).

[154] D. Dai and M. Whangbo, *Spin-Hamiltonian and density functional theory descriptions of spin exchange interactions*, J. Chem. Phys. **114**, 2887 (2001).

[155] M. Cococcioni and S. de Grioncoli, *Linear response approach to the calculation of the effective interaction parameters in the LDA+U method*, Phys. Rev. B **71**, 035105 (2005).

[156] R. Kubo and T. Toyabe, *A stochastic model for low field resonance and relaxation*, in Magnetic resonance and relaxation, edited by R. Blinc (North Holland, 1967), p. 810.

[157] J. D. Dunitz and R. Taylor, *Organic fluorine hardly ever accepts hydrogen bonds*, Chem. Eur. J. **3**, 89 (1997).

[158] J. D. Dunitz, *Organic fluorine: odd man out*, ChemBioChem **5**, 614 (2004).

[159] I. Tirotta, A. Mastropietro, C. Cordiglieri, L. Gazzera, F. Baggi, G. Baselli, M. G. Bruzzone, I. Zucca, G. Cavallo, G. Terraneo, F. Baldelli Bombelli, P. Metrangolo, and G. Resnati, *A superfluorinated molecular probe for highly sensitive in vivo ^{19}F-MRI*, J. Am. Chem. Soc. **136**, 8524 (2014).

[160] I. McKenzie, Z. Salman, S. R. Giblin, Y. Y. Han, G. W. Leach, E. Morenzoni, T. Prokscha, and A. Suter, *Polymer dynamics near the surface and in the bulk of poly(tetrafluoroethylene) probed by zero-field muon-spin-relaxation spectroscopy*, Phys. Rev. E **89**, 022605 (2014).

[161] G. H. Fuller, *Nuclear spins and moments*, J. Phys. Chem. Ref. Data **5**, 835 (1976).